Novel Systems and Techniques for Nonlinear Optics at Low Light Levels

A dissertation presented
by

Michal Bajcsy

to
The School of Engineering and Applied Sciences
in partial fulfillment of the requirements
for the degree of
Doctor of Philosophy
in the subject of

Applied Physics

Harvard University
Cambridge, Massachusetts
December 2009

Thesis advisor
Mikhail D. Lukin

Author
Michal Bajcsy

Novel Systems and Techniques for Nonlinear Optics at Low Light Levels

Abstract

This thesis describes novel experimental approaches to nonlinear optics at low light levels. These approaches focus on significantly increasing the probability of interaction between two weak pulses of light by using novel photonic systems and quantum control techniques.

Specifically, the creation of a stationary pulse of light with non-vanishing photonic component was experimentally demonstrated. Our technique allows a pulse of light to enter into, be stopped inside, and finally be released from a room temperature coherently controlled atomic ensemble, which is dynamically and reversibly turned into a cavity-like system in the process. A detailed theoretical description of the phenomena is presented in addition to the experimental results that show pulses of light kept stationary for up to several microseconds.

We also describe a technique for loading laser-cooled atoms into a single-mode hollow-core photonic-crystal fiber.In our approach, atoms collected in a magneto-optical trap are transferred into a dipole optical trap guided by such fiber. This trap confines the atoms inside the 7 μm diameter hollow core of this fiber for time scales on the order of tens of milliseconds. We observe atomic ensembles consisting of as few as 200 atoms creating an optically thick medium when confined inside the hollow-core fiber. We report the loading of up to 30000 rubidium atoms into this fiber, which results in a system with optical depth 150.

Finally, we demonstrate a fiber-optical switch that is activated at tiny energies corresponding to a few hundred optical photons per pulse. This is achieved by simultaneously confining both photons and a small ensemble of cold atoms inside the microscopic hollow core of a single-mode photonic-crystal fiber and using techniques from quantum optics resulting in slow light propagation and large nonlinear interaction between light beams.

Contents

Title Page i
Abstract iii
Table of Contents iv
Citations to Previously Published Work vii
Acknowledgments viii
Dedication x

1 Introduction **1**
1.1 Motivation 1
1.2 Improving the odds 2
1.3 Nonlinear Optics at Low Light Levels 3
1.4 Overview 5

2 Tools and techniques **6**
2.1 Interaction between a single photon and a single atom: A toy model 6
2.2 Electromagnetically Induced Transparency 9
2.2.1 Slow light 13
2.2.2 Light storage and dark state polaritons 14
2.3 Atom Cooling and Trapping 17
2.3.1 Magneto Optical Trap 17
2.3.2 Magnetic Traps 20
2.3.3 Optical Dipole Trap 21

3 Stationary pulses of light **24**
3.1 Dark-state polariton picture 25
3.2 Making a mirror out of an atomic ensemble 27
3.2.1 Coupled modes in a Bragg grating 28
3.2.2 Wave mixing and Maxwell-Bloch equations 29
3.2.3 Phase matching 36
3.3 Experimental results 37
3.3.1 Continuous wave study 38
3.3.2 Trapping a pulse of light 40

3.4 Outlook 42

4 Cold atoms inside a hollow optical fiber 43

4.1 Preliminary considerations 45
  4.1.1 Fiber selection 45
  4.1.2 Wall attraction and vacuum inside the fiber 46
  4.1.3 Optical depth inside the fiber 46
4.2 From a room-temperature vapor in free space to cold atoms inside the fiber 48
  4.2.1 Fiber mounting structure 50
  4.2.2 Loading procedure 50
4.3 Atoms inside the fiber 52
  4.3.1 Modulated dipole trap 52
  4.3.2 Are the atoms really inside? 52
  4.3.3 Lifetime of atoms inside the fiber 55
  4.3.4 Length of the atomic cloud inside the fiber 56
  4.3.5 Temperature of the fiber confined atomic cloud 56
  4.3.6 Nonlinear saturation based on incoherent few-photon controlled population transfer:
  Counting atoms inside the fiber 57
4.4 MOT to dipole trap transfer procedures 58
  4.4.1 Free fall 59
  4.4.2 Magnetic funnel guiding 61
  4.4.3 Hollow-beam atomic guide 63
4.5 Final remarks 65

5 Nonlinear optics with with tightly confined photons and atoms 67

5.1 EIT with atoms confined to hollow core fiber 67
5.2 An all-optical switch inside a hollow optical fiber 69
  5.2.1 Analysis of pulse transmission 69
5.3 Outlook 72

6 Conclusions 73

6.1 Summary 73
6.2 Future directions 73

A Properties of Rubidium^{87} 75

A.1 Physical and optical properties 75
A.2 Number density of rubidium in the vapor cell 75
A.3 Scattering cross-section of unpolarized rubidium atoms 79

B EIT: Beyond a three level atom 80
- B.1 Probing multiple excited states 80
- B.2 Effects of a third field coupled to a fourth level 81
  - B.2.1 Resonant case 83
  - B.2.2 Far off-resonant case 84
  - B.2.3 Interaction of two slow light pulses 85
- B.3 Coupling of probe and control fields to additional transitions 86
- B.4 EIT and rubidium^{87} 90
- B.5 Doppler broadening 92

C EIT-based wave guide 94
- C.1 Qualitative picture 96
- C.2 Experimental setup 97
- C.3 CW experiment 98
- C.4 Pulsed experiment 99
- C.5 Summary 102

D Technical appendices to Chapter 4 103
- D.1 Vacuum system 103
- D.2 Current carrying structures 105
- D.3 Laser systems 105
  - D.3.1 D_2 line lasers 107
  - D.3.2 D_1 line lasers 107
  - D.3.3 Dipole trap lasers 107
- D.4 Hollow beam generation 108
- D.5 Probe light detection 110
- D.6 Fiber assembly 111

E Atomic cloud expansion in free space 114
- E.1 Evolution of spatial distribution 115
- E.2 Position dependence of velocity 116

Bibliography 119

Citations to Previously Published Work

The experimental results and part of the theory described in Chapter 3 have been published as

> "Stationary pulses of light in an atomic medium", M. Bajcsy, A. S. Zibrov, and M. Lukin Nature **426**, 638-641 (2003).

Large portions of Chapter 4 and 5 have appeared in:

> "Efficient All-Optical Switching Using Slow Light within a Hollow Fiber", M. Bajcsy, S. Hofferberth, V. Balic, T. Peyronel, M. Hafezi, A. S. Zibrov, V. Vuletic, and M. D. Lukin, Phys. Rev. Lett. **102**, 203902 (2009).

Acknowledgments

This work would not have been been possible without the help, support and advice from the large number of extraordinary people I encountered during my stay at Harvard and my four-year-long visit at MIT.

My thanks go first and foremost to Prof. Mikhail Lukin for being my thesis adviser and mentor during the years I spent in graduate school. His scientific brilliance, deep knowledge of many fields, incredible generosity, and patience make him as close to a perfect adviser as a graduate student could wish for. His high standards have been both a challenge and an inspiration for me, and I feel incredibly lucky and grateful for the opportunity to be a member of his research group.

It was a great honor and privilege to become part of the research group led by Prof. Vladan Vuletić during the collaboration on the hollow-core fiber experiment. This work led to my extended visit at MIT and Prof. Vuletić essentially became my second thesis adviser during that time. Learning from him was an amazing experience and I would like to thank him for all of his time, patience, and encouragement which I enjoyed.

Dr. Alexander "Sasha" Zibrov was kind enough to take me under his experimental wing when I was a klutzy first year graduate student. Building on my initially limited experience with optics, he taught me most of what I know now about grating lasers, rubidium vapor cells, and experimental physics in general. It is an understatement to say that without his continued guidance and participation, the experiments described here, in particular the stationary light pulse demonstration, could not have been accomplished.

I most likely will never be able to thank sufficiently Prof. R. Victor Jones and Prof. Frederick H. Abernathy for all their help and sage advice over all the years they have known me, going all the way back to my time as an undergraduate. I am immensely grateful for their support and encouragement, in particular during the rougher spots of my journey as a graduate student.

I would like to thank Prof. Frederico Capasso, Prof. Lene V. Hau, Prof. Mara Prentiss, and Prof. Eugene Demler for being on my qualifying exam committees and for their valuable feedback about the early stages of my graduate research career. In addition, my deep thanks go to Prof. Jones and Prof. Marko Lončar for being a part of my thesis committee and for their feedback on this work. I would also like to thank Prof. Ron Walsworth for his cheery words of advice and encouragement liberally applied at the right moments.

I am grateful for having had the chance to learn from the many great physicists of the MIT-Harvard Center for Ultracold Atoms – attending the lectures of Prof. John Doyle, Prof. Wolfgang Ketterle, Prof. Ike Chuang, Prof. Dave Pritchard, and Prof. Eugene Demler has been both an educational and inspirational experience.

My graduate studies would feel incomplete without my own experience of teaching. I would like to thank Prof. Abernathy, Prof. Woodward Yang, Prof. Jones, and Prof. Michael Branstein for allowing me to work on my teaching skills as a teaching fellow in their classes, which gave me a lot of joy.

It was a great pleasure to work with Dr. Vlatko Balic, Dr. Sebastian Hofferberth, and Thibault Peyronel, my closest collaborators on the hollow-core fiber experiment. I learned a lot from each one of them and their presence made the long hours in the lab a lot of fun. Additionally, I would like to thank Yiwen Chu, who is now a graduate student in Lukin group, David Brown, and Silvia Arroyo Camejo, for their contributions to the hollow-core fiber experiment as undergraduate researchers.

This work greatly benefited from additional collaborations and numerous fruitful discussions, most notably with Axel André, Prof. Michael Fleischhauer, Mohammad Hafezi, Michael Gullans, Alexey Gorshkov, Jake Taylor, Darrick Chang, and Prof. Philip Hemmer.

Additionally, the hollow-core fiber experiment would hardly be possible without the generous help and expert advice from the members of the Vuletić group at MIT, including Jonathan Simon, Haruka Tanji, Marko Cetina, Andrew Grier, Monica Schleier-Smith, Ian Leroux, Saikat Ghosh, Fedja Oručević, Igor Teper, Yu-ju Lin, Renate Landig, and Markus Zwerger.

My thanks also go to all the members of the Lukin group with whom I overlapped during my time here, who are responsible for the incredibly stimulating atmosphere in the group, and whose help I could always count on. In addition to those already mentioned, they include Matt Eisaman, Lily Childress, Caspar van der Wal, Alexei Trifonov, Jeff Thompson, Liang Jiang, Alexey Akimov, Tommaso Calarco, Anders Sorensen, Ana Maria Rey, Paola Cappellaro, Jonathan Hodges, Philip Walther, Peter Rabl, Brendan Shields, Sahand Hormoz, Gurudev Dutt, Alex Nemiroski, Aryesh Mukherjee, Peter Maurer, Michael Hohensee, Jeronimo Maze, Garry Goldstein, Dirk Englund, Frank Koppens, Shimon Kolkowitz, Emre Togan, Norman Yao, Ania Jayich, Nicholas Chisholm, Florent Massou, and GeneWei Li.

In addition to the Lukin group at Harvard and the Vuletić group at MIT, I greatly enjoyed my interactions with the Walsworth group at the Harvard-Smithsonian Center for Astrophysics and received numerous pieces of experimental advice from Dr. David Phillips and Dr. Irina Novikova.

The hollow-core fiber experiment benefited from many custom-machined parts. For this my thanks go to Louis Defeo, Stan Cotreau, Peter Morley, and the personnel from the Harvard and MIT machine shops.

I would furthermore like to thank Marilyn O'Connor, Adam Ackerman, Vickie Greene, and Jean O'Connor from the Physics Department, Susan Wieczorek and Ellen Holloway from SEAS, Joanna Keseberg from CUA, and Maureen Howard from RLE for all their help. My thanks also go to everybody at the Cronkhite Graduate Center for taking care of my physical well-being during long years of my stay there. I will miss the Cronkhite dinning hall very dearly. Lastly, my thanks go to all my friends, and to Christina for being a special person in my life.

Finally, I would like to thank my family, my parents Viera and Július, and my older brother Ján, for their unconditional love, inspiration, and limitless support that made this work possible in the first place.

Dedicated to my parents Viera and Július,
and my older brother Ján.

Chapter 1

Introduction

1.1 Motivation

Realization of a physical system in which a weak light pulse controls the propagation of another light pulse has been a long standing focus of both optical science and engineering [15]. Such a system is an optical equivalent of the electronic transistor and is often referred to as an all-optical switch. In addition to its scientific appeal, such a system promises important applications for optical communication and computation in telecommunication networks, particularly if integrated with modern fiber optical technologies.

Implementation of an all-optical switch controlled with a single photon per switching event would represent the fundamental limit of nonlinear optics (NLO). Further motivation for development of such a device has been provided by potential applications in quantum information science, such as the realization of key protocols from quantum telecommunication [14]. These applications could eventually enable provably secure telecommunication over long distances as well as scalable quantum computers. In addition to applications in quantum information processing, achieving a controllable interaction between weak light pulses is motivated by the need to decrease the energy required for a single switching event in classical telecommunication and information processing systems. This decrease would reduce the total energy consumption of the system, as well as remove restrictions on component density and operating speed dictated by the limits of local power dissipation.

Nonlinear interactions between light pulses containing one or even a few photons are very difficult to achieve. The direct interaction cross-section of photons is vanishingly small, i.e. two photons in vacuum can literally pass through each other without interacting. Nevertheless, photon-photon interaction can be achieved if the optical properties of the medium, in which the photons propagate, change in the presence of those photons. This way the medium acts as a mediator for the photon-photon interaction. Such interaction, however, requires a medium with low photon loss and an optical nonlinearity that is significant at light intensities corresponding to the presence of a single photon.

1.2 Improving the odds

The internal state of a single atom and, thus, its optical properties can change by absorption of a single photon. This makes atoms, as well as "artificial" atoms such as quantum dots [36] or certain point defects in the diamond lattice like nitrogen-vacancy centers [30], good candidates for a physical implementation of a single photon switch.

The probability of interaction between a single atom and a single photon resonant with a particular transition of that atom can be described as $p = \frac{\sigma_o}{A}$, where an atom with resonant scattering cross-section σ_o is sitting in the middle of a spot with area A within which a photon with wavelength λ is localized. Nevertheless, since $\sigma_o \sim \lambda^2$ and since diffraction makes it difficult to localize photons to spots with $A \sim \lambda^2$, the probability of interaction between a single photon and a single atom is in practice small. Additionally, for a switching event to take place, both the the photon that controls the switch operation and the signal photon have to interact with the same atom, which means the probability of a switching event in a system based on a single atom is p^2. Engineering these atom-photon interactions, such that the interaction probability becomes comparable to unity, is therefore necessary for achieving nonlinear optics at low light levels. Our work approaches this problem by developing techniques that increase the effective atom-photon scattering cross-section through the use of optically dense, coherently controlled atomic ensembles and overcome diffraction effects by confining these ensembles within a hollow photonic waveguide.

The task of achieving interaction between a single atom and a single photon can be somewhat simplified by sending the single photon through an atomic ensemble. If the ensemble is optically dense (i.e. opaque), the photon will interact with one of the atoms in the ensemble, but we will not know which one. To realize a switching event between two photons in this ensemble, the second photon that we send in has to interact with the same atom as the first photon did. The use of an atomic ensemble thus increases the probability of the switching event from p^2 to p.

As we will derive in Chapter 2, the probability of interaction between a single atom and a single photon can also be expressed as

$$p \sim \frac{\mu^2}{\hbar^2}\frac{E^2}{\Gamma_e}\tau, \tag{1.1}$$

where E is the peak amplitude of the electric field of the photon, τ is the time the atom is exposed to this field, and Γ_e and μ are the linewidth and strength of the atomic transition. Increasing τ while holding E constant effectively increases the atom-photon interaction probability. As an alternative to the conventional method, which achieves this by injecting the photon into a cavity, we developed a technique that increases τ by creating a stationary pulse of light inside an atomic ensemble [8]. Our technique builds on the previously known slow light [46] and stored or "stopped" light [60, 76] techniques, but, unlike the latter, allows for decoupling of the light pulse's group velocity from its electric field magnitude. This is achieved by dynamically turning the atomic ensemble into a system that could be viewed as an effective cavity and by leveraging the ensemble's optical depth into an effective finesse of this cavity. The experimental demonstration of the stationary light pulse, which forms the core of the first part of this work, was done in a room-temperature rubidium vapor. In this system, the lifetime of the stationary light pulses, and hence the potentially achievable atom-photon interaction time τ, was limited to $\sim 10\ \mu s$ by atomic-motion-induced decoherence.

To overcome the experimental limits associated with a system based on traditional spectroscopy cells filled with room temperature vapors, we developed a new experimental system that would combine the recently developed single-mode hollow-core photonic crystal fiber [25] with a laser-cooled atomic ensemble. This approach allows us to use NLO techniques based on ensembles of isolated cold atoms, while the waveguiding properties of the fiber enable us to work with light pulses transversely focused to an area with diameter $\sim \lambda$ propagating in this focused form over distances not limited by diffraction. As a result, the optical depth of the system is determined only by the number of atoms inside the fiber and large optical depths, such as those assumed in recent proposals for single photon interaction studies [19], can be achieved even with low density ensembles. Additionally, filling the hollow-core fiber with laser-cooled atoms instead of a room-temperature vapor yields two important benefits. First, atoms with temperatures low enough that the Doppler broadening of the atomic transition from the thermal motion becomes negligible have atom-photon scattering cross-section about 100-times bigger than when they are at room temperature. Second, the cold atoms can now be trapped in the center of the hollow core of the fiber. This makes our system potentially suitable for NLO techniques relying on long atomic coherence times, since trapping prevents the atoms from collisions with the fiber wall that lead to loss of atoms or atomic coherence. The outcome of this effort, which forms the second part of this work, is a setup that allows us to load up to $\sim 30,000$ laser-cooled rubidium atoms into a hollow optical fiber with $\sim 7\ \mu m$ diameter core. This results in a medium with an optical depth of ~ 150 whose transparency is controllable through optical nonlinearities currently sensitive to a few hundred photons [7].

1.3 Nonlinear Optics at Low Light Levels

The implementation of few-photon nonlinear optics has until now only been feasible in the context of cavity quantum electrodynamics (QED) when single quantum emitters, such as neutral atoms or quantum dots, are placed inside narrow-band, high-finesse cavities. In these systems, the original nonlinearities of the optical medium created by the single emitter are amplified by the cavity finesse to the point where they can be controlled by the field of a single photon. Over the last decade, several experiments have demonstrated nonlinear optical phenomena with single intracavity photons [12, 91, 35, 27]. However, these experiments remain technologically challenging and must compromise between cavity bandwidth, mirror transmission and atom-photon interaction strength. Consequently, large nonlinearities are accompanied in these systems by substantial losses at the input and output of the cavity.

An alternative approach is based on coupling single emitters or ensembles of emitters to a propagating light field confined to an area comparable to the diffraction limit. This results in the electric field from a single photon being sufficiently large to cause nonlinear behavior on a single pass and without the environment of an optical cavity. Such tight confinement can be achieved either in free space by focusing the light beam with a large numerical aperture lens [11] or under conditions provided by a photonic waveguide. In particular, systems based on hollow core photonic crystal fibers [25], hollow antiresonant reflecting waveguides (ARROWs) [97], optical nanofibers [88], and nanostructure plasmonic waveguides allowing subdiffraction propagation [29] have all been actively explored in the last few years.

Hollow core photonic crystal fibers (PCFs, also known as photonic bandgap fibers), that guide light through interference [51] instead of total internal reflection [80], are now available off the shelf and can be integrated with conventional optical fibers [9]. When filled with molecular gas, these fibers have shown significant enhancements in the efficiency of processes such as stimulated Raman scattering [10] and four-wave mixing [56]. Recently, both room-temperature and ultra-cold atoms have successfully been loaded into PCFs [38, 87, 21] and observations of electromagnetically induced transparency with less than a micro-Watt control field have been reported [38].

Optical nanofibers [88] are created when a glass optical fiber is heated close to its melting point and carefully pulled. The resulting tapered section, which can be significantly less than an optical wavelength in diameter, can still guide light in single mode via total internal reflection. However most of the light now propagates outside of the fiber in the form of tightly focused evanescent field to which room temperature [85] or laser cooled [69, 79] atoms can be coupled with single-atom single-photon interaction probability $\sim 10\%$ in the case of cold atoms.

Finally, efficient conversion of a single photon emitted by a single quantum dot into a single surface plasmon polariton propagating on a silver nanowire has also been recently demonstrated [1].

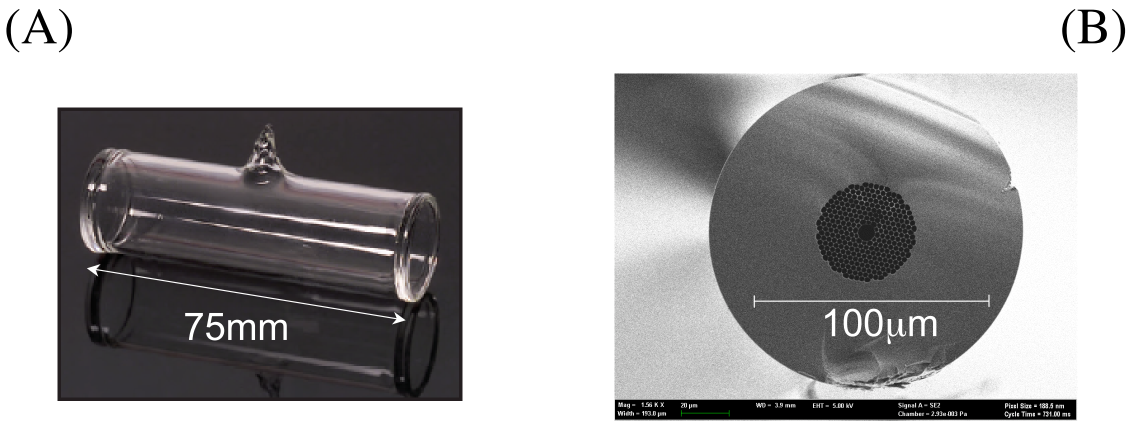

Figure 1.1: (A) Rubidium vapor cell. (B) Hollow core photonic crystal fiber.

1.4 Overview

The results presented in this thesis are organized as follows. Chapter 2 provides a brief introduction of the main tools from quantum optics and atomic physics used in this work: electromagnetically induced transparency (EIT), atom cooling and trapping techniques, and a toy model of single atom single photon interaction. Chapter 3 explains the theory of stationary light pulse creation and describes the experimental demonstration of a stationary light pulse in a room-temperature rubidium vapor. Chapter 4 introduces our apparatus for loading of laser-cooled atoms into a hollow-core photonic-crystal fiber and explores the mechanisms of the loading procedure. Chapter 5 describes our first nonlinear optics experiment demonstrated in this system involving an all-optical switch controlled by optical pulses containing less than a thousand photons. Finally, Chapter 6 summarizes the results of this work, and discusses future experiments in nonlinear optics at low light levels, as well as general outlooks beyond the single photon switch.

Chapter 2

Tools and techniques

In this chapter, we will first derive the probability of interaction between a single atom and a single photon. Understanding the mechanisms of this probability provides an important conceptual framework for nonlinear optics at low light levels. From this we will proceed to an overview of the phenomena based on electrically induced transparency (EIT), in particular slow light pulses and coherent light storage. We will build on these techniques in Chapter 3 and Chapter 5. In the last section of this chapter, we will briefly introduce some of the cooling and trapping techniques developed in the last three decades for neutral atoms. We will again stick mostly to conceptual descriptions with more details available for example in [65] and references therein. These techniques allow us to cool rubidium vapor from room temperature to $\sim 40\mu K$ and then guide and trap them inside a hollow optical fiber as described in Chapter 4.

2.1 Interaction between a single photon and a single atom: A toy model

Consider a single two level atom at rest (Fig. 2.1) interacting with electric field E oscillating at frequency ν that resonantly (i.e. $\nu = \omega_{ab}$) couples the ground state $|b\rangle$ to the excited state $|a\rangle$ with Rabi frequency $\Omega_p = \frac{\mu_{ab}}{\hbar}E$, where μ_{ab} is the electric dipole moment of the transition between the two levels. At time $t_0 = 0$, the atom is in its ground state $|b\rangle$. By absorbing a single photon from the electric field, the atom gets excited into state $|a\rangle$. Once in state $|a\rangle$, two things can happen. The atom either emits a clone of the originally absorbed photon and returns into state $|b\rangle$, or the atom can spontaneously emit a photon into a different mode of the electric field, which happens at a rate $\frac{\Gamma}{2}$, where Γ is the linewidth of the atomic transition. We can describe the system with a wavefunction $|\psi\rangle = a|a\rangle + b|b\rangle$ that obeys the Schroedinger equation $i\hbar\frac{\partial}{\partial t}|\psi\rangle = \hat{H}_{eff}|\psi\rangle$, with $|a|^2$ and $|b|^2$ representing the probabilities of the atom being in state $|a\rangle$ and $|b\rangle$. Using the stochastic wave-function approach [37]

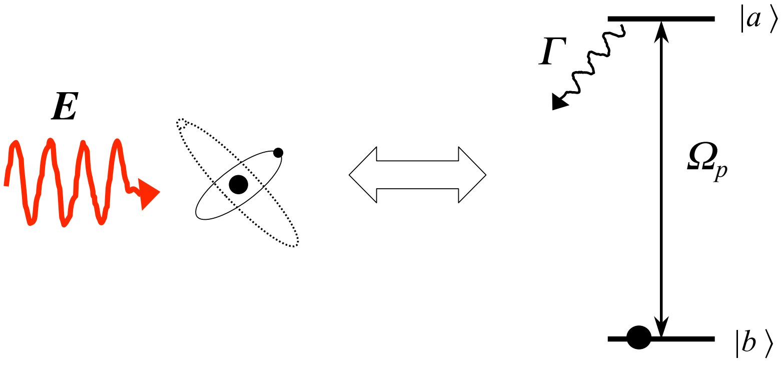

Figure 2.1: Two level atom interacting with electric field. The difference between energies of the two levels is $\hbar\omega_{ab}$.

with a non-Hermitian Hamiltonian for the system

$$\hat{H} = \hbar\omega_{ab}|a\rangle\langle a| - \hbar\frac{\Omega_p}{2}e^{-i\nu_p t}|a\rangle\langle b| - i\hbar\frac{\Gamma}{2}|a\rangle\langle a| + \text{c.c.}, \tag{2.1}$$

we obtain the following equations of motion:

$$\begin{aligned} \frac{d}{dt}\tilde{a} &= -\frac{\Gamma}{2}\tilde{a} + i\frac{\Omega_p}{2}b \\ \frac{d}{dt}b &= i\frac{\Omega_p^*}{2}\tilde{a} \end{aligned} \tag{2.2}$$

where we made the substitution $a = \tilde{a}\,e^{-i\nu t}$.

The probability $P(t_{int})$ that during the interaction time interval $t_{int} = t - t_0$, with $\Omega_p t_{int} \ll 1$, an interaction between the atom and the field took place, is then equal to the probability that the atom left state $|b\rangle$, i.e. $P(t_{int}) = 1 - |b(t)|^2$. Solving equations (2.7)and assuming $\Gamma^2 \gg 4|\Omega_p|^2$, we get that within a first-order approximation $b(t) \approx e^{-\frac{\Omega_p^2}{2\Gamma}t}$ and

$$P(t_{int}) \approx 1 - e^{-\frac{|\Omega_p|^2}{\Gamma}t_{int}} \approx \frac{\mu_{ab}^2}{\hbar^2}\frac{E^2}{\Gamma}t_{int}. \tag{2.3}$$

Assume the field E consists of a single photon pulse of temporal length τ_p propagating in vacuum with velocity c. The longitudinal spatial localization (or simply length) of the pulse and the peak amplitude of the field then can be written as $L_{pulse} \approx c\tau_p$ and $E_0 = \sqrt{\frac{2\hbar\nu}{\epsilon_o A c\tau_p}}$, respectively, with A being given by the transverse localization of the photon. For example, a photon in a Gaussian beam with waist w_o is localized to an area $A = \frac{\pi w_o^2}{2}$. If a single atom from Fig. 2.1 is suspended on the axis of the pulse's propagation, the quantity $g = \frac{\mu_{ab}}{\hbar}E_0$ would be referred to as the single photon Rabi frequency and the atom will ordinarily interact with the field of the single photon for time $t_{int} \approx \tau_p$. Combining this with (2.3), we obtain that the probability of interaction between a single photon and a single atom is

$$p \approx \frac{\mu^2}{\hbar^2}\frac{E_0^2}{\Gamma}t_{int} = \frac{2\mu_{ab}^2\nu\tau_p}{\hbar\epsilon_o A L_{pulse}\Gamma} = \frac{\sigma}{A}, \tag{2.4}$$

where the quantity

$$\sigma = \frac{\mu_{ab}^2\nu}{\hbar\epsilon c\frac{\Gamma}{2}} \tag{2.5}$$

is referred to as the resonant atom-photon scattering cross-section.

Under ordinary free-space conditions, τ_p is the time the photon will interact with (or spend in the vicinity of) the atom, but because of the way τ_p and L_{pulse} are related to E_0, p will remain constant even when we change the spatial or temporal length of the single photon pulse. However, if we increase the time the photon spends near the atom without decreasing E_0 – in other words, decouple the interaction time from the single photon pulse field amplitude and duration – the result will be an effective increase in the atom-photon scattering cross-section:

$$\sigma_{eff} = \frac{t_{int}}{\tau_p}\sigma_o \tag{2.6}$$

If the atom is moving at a velocity v_z parallel to the propagation direction of the field E, then due to Doppler shift the atom will perceive the field as oscillating at frequency $\nu' = \nu(1 \mp \frac{v_z}{c})$, where the minus sign corresponds to the atom moving in the same direction as the field propagation. Equations (2.2) will change to

$$\begin{aligned} \frac{d}{dt}\tilde{a} &= -\left(\frac{\Gamma}{2} - i\delta\right)\tilde{a} + i\frac{\Omega_p}{2}b \\ \frac{d}{dt}b &= i\frac{\Omega_p^*}{2}\tilde{a} \end{aligned} \tag{2.7}$$

where $\delta = -\frac{\nu v_z}{c}$. For an ensemble of atoms with mass m at temperature T, the probability density for v_z follows the Maxwell-Boltzmann distribution $f_{v_z} = \left(\frac{m}{2\pi k_B T}\right)^{1/2}\exp\left[-\frac{m v_z^2}{2k_B T}\right]$. Averaging the solutions of (2.7) over all possible v_z we find that for a large enough temperature (in the case of ^{87}Rb for $T \gg 30mK$), the atom-field interaction can be well approximated by assuming an atom at rest with excited state linewidth

$$\Gamma_D \approx \Gamma + \left(\frac{\nu}{c}\right)\sqrt{\frac{2\pi k_B T}{m}} \tag{2.8}$$

and scattering cross-section

$$\sigma_{Dopp} \approx \frac{\pi}{2}\frac{\Gamma}{\Gamma_{Dopp}}\sigma_o. \tag{2.9}$$

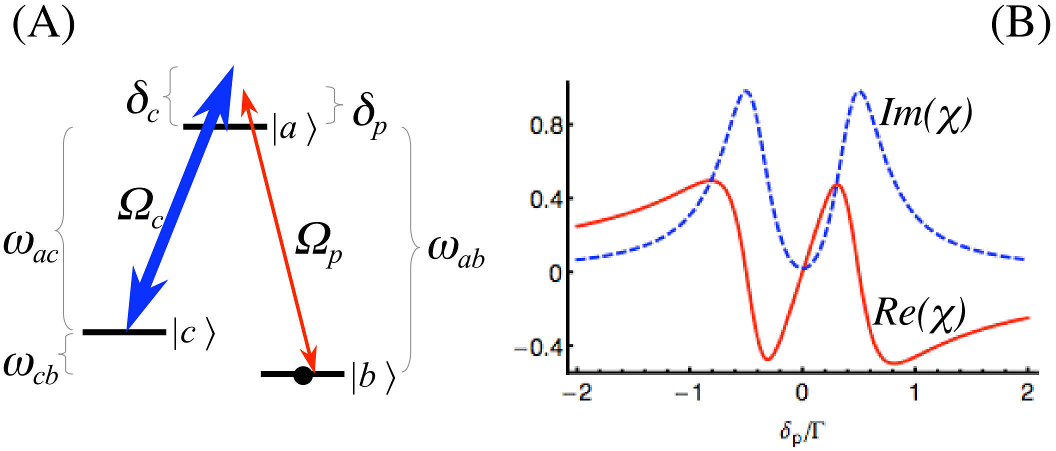

Figure 2.2: (A) Three level atom interacting with probe and control fields. (B) Real and imaginary parts of the susceptibility seen by the probe field for $\gamma = \frac{\Gamma}{100}$ and $\Omega_c = \Gamma$.

For comparison, the natural linewidth of the excited state of a ^{87}Rb atom is $\frac{\Gamma}{2\pi} \approx 6MHz$, while $\frac{\Gamma_D}{2\pi} \approx 600MHz$ at $T \approx 86°C$, which is the temperature of the rubidium vapor during the experiments described in Chapter 3.

2.2 Electromagnetically Induced Transparency

Consider a three-level atom such as the one in Fig. 2.2A interacting with two light fields – field $E_c = \frac{1}{2}\mathcal{E}_c e^{-i\nu_c t}$ + c.c. that couples state $|c\rangle$ to the excited state $|a\rangle$ with Rabi frequency $\Omega_c = \frac{\mu_{ac}}{\hbar}\mathcal{E}_c$ and field $E_p = \frac{1}{2}\mathcal{E}_p e^{-i\nu_p t} + c.c.$ that couples the ground state $|b\rangle$ to the excited state $|a\rangle$ with Rabi frequency $\Omega_p = \frac{\mu_{ab}}{\hbar}\mathcal{E}_p$. If the difference between the frequency of the probe field and the frequency of the control field, $\nu_p - \nu_c$, is equal to the frequency splitting between states$|c\rangle$ and $|b\rangle$ ω_{cb},the interaction Hamiltonian for the system reduces to $\hat{H}_{int} = -\hbar\frac{\Omega_p}{2}|a\rangle\langle b| - \hbar\frac{\Omega_c}{2}|a\rangle\langle c| + c.c.$ and the atom will be driven into a state $|D\rangle$ that is superposition of states $|c\rangle$ and $|b\rangle$, such that

$$|D\rangle = \frac{\Omega_c|b\rangle - \Omega_p|c\rangle}{\sqrt{\Omega_p^2 + \Omega_c^2}}. \tag{2.10}$$

Once in this state, also called the dark state [5], the atom's absorption paths from $|b\rangle$ and $|c\rangle$ will interfere destructively and the atom will stop interacting with both fields. For our purposes, we are interested in the propagation of the slowly varying envelope $\mathcal{E}_p$ of the field E_p through an ensemble of these atoms in the limit where $\Omega_c \gg \Omega_p$. Note that in this limit E_c and E_p are referred to as the control and probe fields, respectively.

To examine the behavior of this system in a more quantitative fashion, we employ a simplified version of the Maxwell-Bloch equations called the stochastic wave-function method [37]. We set the wave-function of the atom to be $|\psi\rangle = a|a\rangle + b|b\rangle + c|c\rangle$ and add two decay channels to the original Hamiltonian

$$\hat{H} = \hbar\omega_a b|a\rangle\langle a| + \hbar\omega_{cb}|c\rangle\langle c| - \mu_{ab}|a\rangle\langle b|\frac{1}{2}\mathcal{E}_p e^{-i\nu_p t} - \hbar\frac{\Omega_c}{2}e^{-i\nu_c t}|a\rangle\langle c| + \text{c.c.} \tag{2.11}$$

to effectively take into account incoherent loses in the system:

$$\hat{H}_{eff} = \hat{H} - i\hbar\frac{\Gamma}{2}|a\rangle\langle a| - i\hbar\gamma|c\rangle\langle c|. \tag{2.12}$$

Here Γ is mainly due to the finite lifetime of the excited state $|a\rangle$, while γ, although treated as a result of finite lifetime of state $|c\rangle$, is usually dominated by other phenomena that we will discuss later. The non-Hermitian Schroedinger equation $i\hbar\frac{\partial}{\partial t}|\psi\rangle = \hat{H}_{eff}|\psi\rangle$ yields the following equations of motion for the wave-function's coefficients:

$$\begin{aligned}
\dot{\tilde{a}} &= -(\frac{\Gamma}{2} - i\delta_p)\tilde{a} + \frac{i}{2}\Omega_c\tilde{c} + i\frac{\mu_{ab}}{2\hbar}\mathcal{E}_p b \\
\dot{b} &= i\frac{\mu_{ab}}{2\hbar}\mathcal{E}_p^*\tilde{a} \\
\dot{\tilde{c}} &= -(\gamma - i[\delta_p - \delta_c])\tilde{c} + \frac{i}{2}\Omega_c^*\tilde{a}.
\end{aligned} \tag{2.13}$$

Here $\delta_p = \nu_p - \omega_{ab}$ and $\delta_c = \nu_c - \omega_{ac}$ denote the mismatch between the carrier frequency of the probe and control fields from the their respective transitions, and substitutions $a = \tilde{a}\,e^{-i\nu_p t}$ and $c = \tilde{c}\,e^{-i\nu_c t}$ were made in order to to simplify the equations by eliminating the fast oscillating terms. At the same time, the propagation of the probe field $E_p = \frac{1}{2}\mathcal{E}_p e^{-i\nu_p t}e^{ik_p z} + c.c.$, with $k_p = \frac{\nu_p}{c}$, through a medium consisting of such three level atoms can be described in the slowly varying envelope approximation (SVEA) [82] as

$$\frac{\partial}{\partial z}\mathcal{E}_p + \frac{1}{c}\frac{\partial}{\partial t}\mathcal{E}_p = \frac{1}{2}\mu_o c\nu_p\mathcal{P}. \tag{2.14}$$

Here, $\mathcal{P}$ is the slowly varying envelope of the medium's polarization density defined as $P = n(\mu_{ba}ab^* + \mu_{ab}a^*b) = \frac{1}{2}\mathcal{P}e^{-i\nu_p t}e^{ik_p z} + \text{c.c.}$, with n being the number of atoms per unit volume, and where we for simplicity assumed that E_p and E_c are planar waves. Incidentally, since most calculations in this work assume $\Omega_c \gg \Omega_p$, unless otherwise stated we will take the approximation $b \approx 1$ and take $ab^* \approx a$, together with $cb^* \approx c$.

For continuous wave (CW) control and probe fields in the the $\Omega_c \gg \Omega_p$ limit, one can find a steady state solution to (2.13) by setting $\dot{\tilde{a}} = \dot{b} = \dot{\tilde{c}} = 0$ and taking the approximation $b \approx 1$:

$$\begin{aligned}
\tilde{a} &= i\frac{\mu_{ab}}{2\hbar}\frac{\gamma - i[\delta_p - \delta_c]}{(\frac{\Gamma}{2} - i\delta_p)(\gamma - i[\delta_p - \delta_c]) + \frac{|\Omega_c|^2}{4}}\mathcal{E}_p \\
\tilde{c} &= -\frac{\mu_{ab}}{4\hbar}\frac{\Omega_c^*\mathcal{E}_p}{(\frac{\Gamma}{2} - i\delta_p)(\gamma - i[\delta_p - \delta_c]) + \frac{|\Omega_c|^2}{4}}.
\end{aligned} \tag{2.15}$$

Combining (2.15) with (2.14), where we set $\frac{\partial}{\partial t}\mathcal{E}_p = 0$, will give us

$$\frac{\partial}{\partial z}\mathcal{E}_p = -\frac{\sigma_o n}{4}\frac{\Gamma\tilde{\gamma}}{\tilde{\Gamma}\tilde{\gamma} + \frac{|\Omega_c|^2}{4}}, \tag{2.16}$$

where $\tilde{\gamma} = \gamma - i[\delta_p - \delta_c]$ and $\tilde{\Gamma} = \frac{\Gamma}{2} - i\delta_p$, while $\sigma_o = \frac{\mu_{ab}^2 \nu_p}{\hbar\epsilon_o c\frac{\Gamma}{2}}$ is the resonant atom-photon scattering cross-section derived in the previous section. Integrating (2.16) along the propagation distance z results in

$$\mathcal{E}_p(z) = \mathcal{E}_p(0)\exp[-\frac{n\sigma_o\Gamma z}{4}\frac{\gamma - i[\delta_p - \delta_c]}{(\frac{\Gamma}{2} - i\delta_p)(\gamma - i[\delta_p - \delta_c]) + \frac{|\Omega_c|^2}{4}}]. \tag{2.17}$$

For $\Omega_c = 0$, (2.17) reduces to transmission through a two level medium

$$\mathcal{E}_p(L, \Omega_c = 0) = \mathcal{E}_p(0)\exp[-\frac{OD}{2}\frac{\frac{\Gamma}{2}}{\frac{\Gamma}{2} - i\delta_p}], \tag{2.18}$$

where

$$\text{OD} = \int_L n(z)\sigma_o dz \rightarrow n\sigma_o L, \tag{2.19}$$

is defined as the optical depth of the medium, with L being the length of the ensemble. Not surprisingly, the two-level medium is opaque when the probe field is on resonance, i.e. $\delta_p = 0$.

Consider now the case $\delta_c = 0$ and $|\Omega_c|^2 \gg \gamma\Gamma$. This condition is most often relatively easy to fulfill even with relatively small power in the control field, since for an atomic system in Fig. 2.2A $\Gamma \gg \gamma$ usually. When the probe field is on resonance, the medium's opacity will now be significantly reduced since $\mathcal{E}_p(L) \approx \mathcal{E}_p(0\exp[-\frac{\text{OD}\,\Gamma\gamma}{|\Omega_c|^2}]$ as demonstrated for the first time in [13]. In the limiting case of $\gamma \rightarrow 0$ the medium becomes completely transparent as predicted initially.

Fig. 2.2B shows the real part (solid line) and imaginary part (dashed line) of this medium's susceptibility

$$\chi(\delta_p, \delta_c) = \frac{n\sigma_o\Gamma}{4}\frac{\gamma - i[\delta_p - \delta_c]}{(\frac{\Gamma}{2} - i\delta_p)(\gamma - i[\delta_p - \delta_c]) + \frac{|\Omega_c|^2}{4}} \tag{2.20}$$

in units of $\frac{\sigma_o n}{2}$ for the case $\delta_c = 0$. The minimum in $Im(\chi)$ around $\delta_p = 0$ can be experimentally observed as a transmissive resonance with a full-width half-maximum frequency band for power transmission of

$$\Delta_{FWHM} = \sqrt{\frac{\ln 2}{\text{OD}}}\frac{|\Omega_c|^2}{\Gamma}\left(1 + \frac{2\gamma\Gamma}{|\Omega_c|^2}\right). \tag{2.21}$$

In addition to this transparency window, the steep linear slope in $Re(\chi)$ which overlaps with the transparency window, is also worth noticing as it leads to significantly reduced group velocity, coinciding with good transmission, for resonant light pulses propagating through this atomic ensemble.

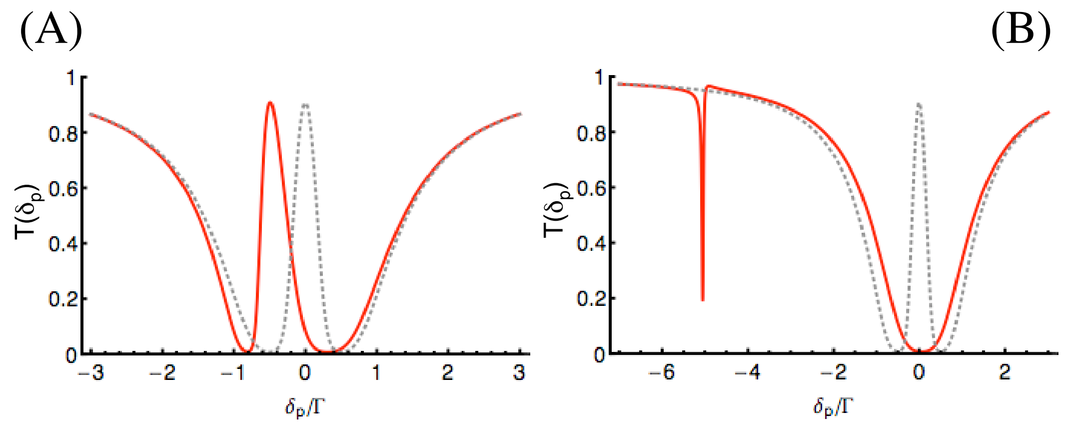

Figure 2.3: EIT medium transmission $T = \frac{P_{in}}{P_{out}} = \left|\frac{\mathcal{E}_p(z=L)}{\mathcal{E}_p(z=0)}\right|^2$ for (A) $\delta_c = -\frac{\Gamma}{2}$ and (B) $\delta_c = -10\Gamma$. OD $= 5$, $\gamma = \frac{\Gamma}{100}$, $\Omega_c = \Gamma$, and the dotted line plots represent $\delta_c = 0$ for comparison.

Two-photon absorption

It is worth briefly discussing the system's behavior when $\delta_c \neq 0$. As $|\delta_c|$ increases, the medium's transparency window becomes increasingly asymetric in frequency (see Fig. 2.3A). In the limit where $\delta_c^2 \gg \Gamma^2$ the medium will develop two separate absorption peaks as in Fig. 2.3B. The first one is roughly identical to the absorption of an ensemble of two-level atoms. The second one corresponds to a two-photon process, in which the absorption of a probe photon coincides with a control field photon being emitted while atom transfers from state $|b\rangle$ into state $|c\rangle$. This two-photon transition will be centered at

$$\delta_{p2} \approx \delta_c + \frac{|\Omega|^2}{4\delta_c}, \tag{2.22}$$

have a linewidth of

$$\Gamma_{2phot} \approx 2\gamma + \Gamma\frac{|\Omega|^2}{4\delta_c^2}, \tag{2.23}$$

and its effective scattering cross-section will be

$$\sigma_{2phot} \approx \sigma_o \frac{\frac{\Gamma}{2}\frac{|\Omega|^2}{|\Omega|^2+4\delta_c^2}}{\gamma + \frac{\Gamma}{2}\frac{|\Omega|^2}{4\delta_c^2}}. \tag{2.24}$$

EIT in a Doppler-broadened medium

To observe EIT in an ensemble of warm atoms, one has to make sure that the frequency difference between probe and control field, as seen by a moving atom, remains close the frequency split between levels $|b\rangle$ and $|c\rangle$ for atoms with different velocities. This can be achieved reasonably well if the probe and control fields are copropagating or if there is only a very small angle between them. This is in contrast with EIT experiments in cold atoms that can be performed with any probe-control geometry of convenience. For a Doppler-broadened medium of three-level atoms, the susceptibility then has to be averaged over the velocity distribution of the atoms and (2.20) becomes

$$\begin{aligned}\chi_{Dopp}(\delta_p,\delta_c) &= \frac{n\sigma_o\Gamma}{4}\left(\frac{m}{2\pi k_B T}\right)^{1/2} \\ & \int_{-\infty}^{+\infty} e^{-\frac{mv^2}{2k_BT}} \frac{\gamma - i\left[\delta_p-\delta_c-\frac{\nu_p-\nu_c}{c}v\right]}{(\frac{\Gamma}{2}-i\delta_p-i\frac{\nu_p}{c}v)(\gamma-i[\delta_p-\delta_c-\frac{\nu_p-\nu_c}{c}v])+\frac{|\Omega_c|^2}{4}}dv.\end{aligned} \tag{2.25}$$

For $|\delta_p|, |\delta_c| \ll \Gamma_D$ from (2.8), the susceptibility (2.25) can be approximated reasonably well by

$$\chi_{Dopp}(\delta_p,\delta_c) \approx \frac{n\sigma_{Dopp}\Gamma_D}{4}\frac{\gamma-i[\delta_p-\delta_c]}{(\frac{\Gamma_D}{2}-i\delta_p)(\gamma-i[\delta_p-\delta_c])+\frac{|\Omega_c|^2}{4}}. \tag{2.26}$$

2.2.1 Slow light

To analyze the propagation of a light pulse with carrier frequency ν_p and duration τ_p inside a medium consisting of three level atoms from Fig.2.2A, we take the time-domain Fourier transform of equations (2.13), which will yield

$$\begin{aligned}\tilde{a}(z,\omega) &= i\frac{\mu_{ab}}{2\hbar}\frac{\tilde{\gamma}-i\omega}{(\tilde{\Gamma}-i\omega)(\tilde{\gamma}-i\omega)+\frac{|\Omega_c|^2}{4}}\mathcal{E}_p(z,\omega) \\ \tilde{c}(\omega,z) &= -\frac{\mu_{ab}}{4\hbar}\frac{\Omega_c^*}{(\tilde{\Gamma}-i\omega)(\tilde{\gamma}-i\omega)+\frac{|\Omega_c|^2}{4}}\mathcal{E}_p(z,\omega)\end{aligned} \tag{2.27}$$

where $\mathcal{E}_p(z,\omega)$ is the Fourier transform of $\mathcal{E}_p(z,t)$ and we assume Ω_c to be time independent. Note that in the limit of very weak probe, $\dot{b} \sim \mathcal{O}(a\mathcal{E}_p) \sim \mathcal{O}(\mathcal{E}_p^2)$, which approaches 0. Combining 2.27 with the Fourier transform of (2.14), we get

$$\frac{\partial}{\partial z}\mathcal{E}_p(z,\omega) - \frac{i\omega}{c}\mathcal{E}_p(z,\omega) = -\chi(\omega)\mathcal{E}_p(z,\omega) \tag{2.28}$$

where

$$\chi(\omega) = \frac{n\sigma_o\Gamma}{4}\frac{\tilde{\gamma}-i\omega}{(\tilde{\Gamma}-i\omega)(\tilde{\gamma}-i\omega)+\frac{|\Omega_c|^2}{4}}. \tag{2.29}$$

Here the complex decay rates $\tilde{\gamma} = \gamma - i[\delta_p - \delta_c]$ and $\tilde{\Gamma} = \frac{\Gamma}{2} - i\delta_p$ are determined by the detunings of the frequency of the control field and the carrier frequency of the probe pulse from their respective atomic transitions.

If the pulse's bandwidth, $\sim \frac{1}{\tau_p}$, fits within the transparency window in Fig.2.2B (which is equivalent to $\Omega_c \tau_p \gg 1$) and $\frac{|\Omega_c|^2}{4} \gg \tilde{\Gamma}\tilde{\gamma}$, the solution to (2.28) can be approximated by

$$\mathcal{E}_p(z,\omega) \approx \mathcal{E}_p(z=0,\omega) \exp\left[-\frac{n\sigma_o\Gamma\tilde{\gamma}z}{|\Omega_c|^2}\right] \exp\left[\frac{i\omega z}{c}(1+\frac{n\sigma_o c\Gamma}{|\Omega_c|^2})\right]. \tag{2.30}$$

In the time domain this solution corresponds to a pulse that propagates with a group velocity

$$v_g \approx \frac{c}{1+\frac{n\sigma_o c\Gamma}{|\Omega_c|^2}} \approx \frac{|\Omega_c|^2}{n\sigma_o\Gamma} \tag{2.31}$$

determined by the magnitude of the control field. The pulse will get attenuated by a factor $\sim \exp[-\frac{n\sigma_o\Gamma\gamma L_{ensemble}}{|\Omega_c|^2}]$ after it passes through the atomic ensemble and pick up an overall phase $\sim \frac{n\sigma_o\Gamma(\delta_p-\delta_c)}{|\Omega_c|^2}$ per unit length of propagation.

When a pulse propagating in vacuum starts entering the atomic ensemble, its front edge will be slowed down to v_g while the back of the pulse will be still propagating at c. As a result, the pulse will shrink in length by a factor of $\frac{v_g}{c}$ while its peak field amplitude will remain unchanged. As the pulse propagates inside the medium, the energy in the electric field will also shrink by a factor of $\frac{v_g}{c}$ compared to the original pulse. The rest of the energy is stored in an atomic spin wave [63] consisting of atoms transferred into the "dark state" superposition between levels $|b\rangle$ and $|c\rangle$ from (2.10). This wave of atomic coherence will propagate together with the light pulse as can be seen in the second equation of (2.27). As the pulse exits the medium, the spin wave will be converted back into electric field energy and the pulse will stretch back to its original length.

It is worth noting that due to this pulse contraction, a single photon pulse will spend the same amount of time in the vicinity of a particular atom as it would in free space, despite the significant reduction in group velocity. Thus, ordinarily, $\sigma_{eff} = \sigma_o$ even in this system. However, the reduced group velocity can be used to our advantage and we will discuss how to do this at the end of Chapter 5.

Finally note that for $\gamma \rightarrow 0$ the group velocity achievable in this system has virtually no lower bound. For $\gamma > 0$, the lower limit on v_g is given by the losses in transmission one is willing to accept . Experimentally, values as low as a few meters per second have been observed in an ultra-cold atomic vapor [46], while values $\sim km/s$ can be easily achieved even in room temperature spectroscopy cells.

2.2.2 Light storage and dark state polaritons

The contraction of the pulse's spatial length due to the change of the group velocity between free space and the atomic medium will allow a light pulse with a free space length of several hundred meters to be completely localized inside an atomic ensemble for low enough group velocity and sufficiently high optical depth of the ensemble. The length of such an ensemble can be as small as a few tens of micrometers [46, 60] and it usually does not exceed a few centimeters [52, 76]. If the amplitude of the control field is decreased while the pulse propagates in the medium, the group velocity of the pulse will decrease as well. However, in this case, the spatial length of the pulse will remain the same as the group velocity decreases, and instead the electric field amplitude of the probe pulse will decrease proportionally with the control field, while additional energy from the electric field of the probe pulse is transferred into the atomic spin wave. Conversely, if the control field is increased, the probe pulse will speed up and energy will be transferred from the atomic spin wave into the electric field of the probe pulse.

In the limiting case when the control field is decreased to zero, the group velocity and the electric field of the probe pulse will both become zero as the pulse is completely stored in the form of atomic coherence. When the control field is turned on again, the process is reversed and the atomic coherence is converted back into a probe pulse propagating at group velocity $v_g \approx \frac{|\Omega_c|^2}{n\sigma_o\Gamma}$.

This process can also be quantitatively described in the framework of dark-state polaritons [33]. These wave-like excitations are superpositions of the electric field of the probe pulse and of the atomic spin coherence propagating together with the pulse and can in our case be defined as:

$$\Psi(z,t) = \cos\theta(t)\mathcal{E}_p(z,t) - \sin\theta(t)\sqrt{\kappa}\tilde{c}(z,t) \tag{2.32}$$

where $\cos\theta(t) = \frac{\Omega_c(t)}{\sqrt{\Omega_c^2(t)+\kappa}}$ and $\sin\theta(t) = \frac{\sqrt{\kappa}}{\sqrt{\Omega_c^2(t)+\kappa}}$ and $\kappa = \frac{n\sigma_o c\Gamma}{2}$. In the ideal limit when Ω_c changes adiabatically and $\gamma \longrightarrow 0$, Ψ obeys the following equation of motion [33]:

$$\left[\frac{\partial}{\partial t} + c\cos^2\theta(t)\frac{\partial}{\partial z}\right]\Psi[z,t] = 0 \tag{2.33}$$

which describes a shape-preserving propagation with velocity $v = v_g(t) = c\cos^2\theta(t)$:

$$\Psi(z,t) = \Psi\left(z - c\int_{t_0}^{t} d\tau\cos\theta(\tau), t_0\right) \tag{2.34}$$

Experimentally, stored light retrieval is limited by losses from the atomic coherence decay. However, the process is however fairly robust and works even when pulses are not fully confined in the ensemble (in which case only a fraction of the pulse gets stored) and under non-adiabatic conditions. Since the first two independent reports in 2001 in ultra-cold [60] and room temperature [76] gases, storage and retrieval of light pulses has been demonstrated in various ensembles, including solid state materials [89].

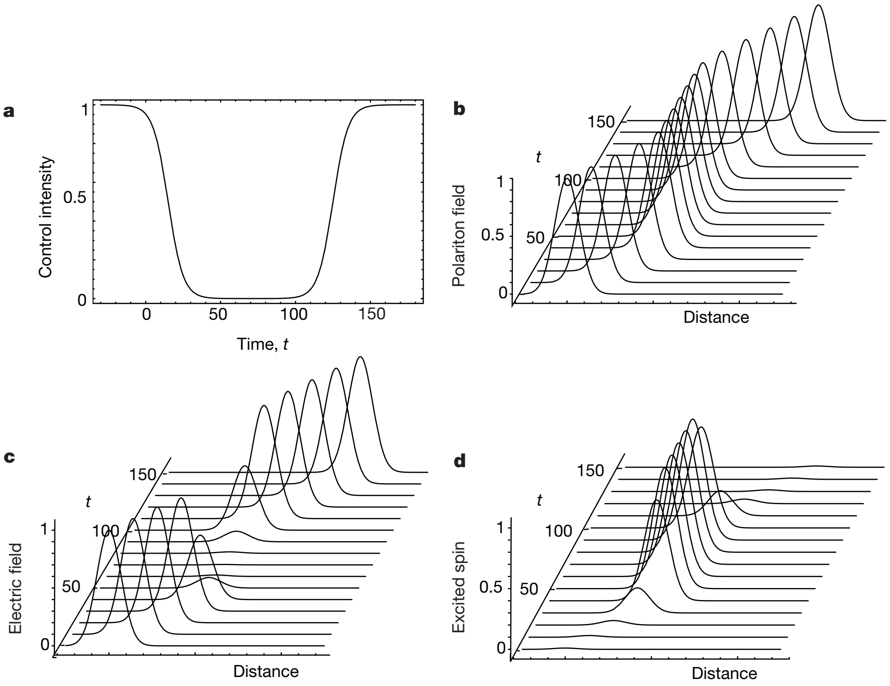

Figure 2.4: Stopping and reaccelerating a polariton. (a) shows the ramping of the control field during the process. (b), (c), and (d) show the amplitudes and propagation of the polariton Ψ, the electric field $\mathcal{E}_p$, and of the atomic spin coherence. Figure taken from [33].

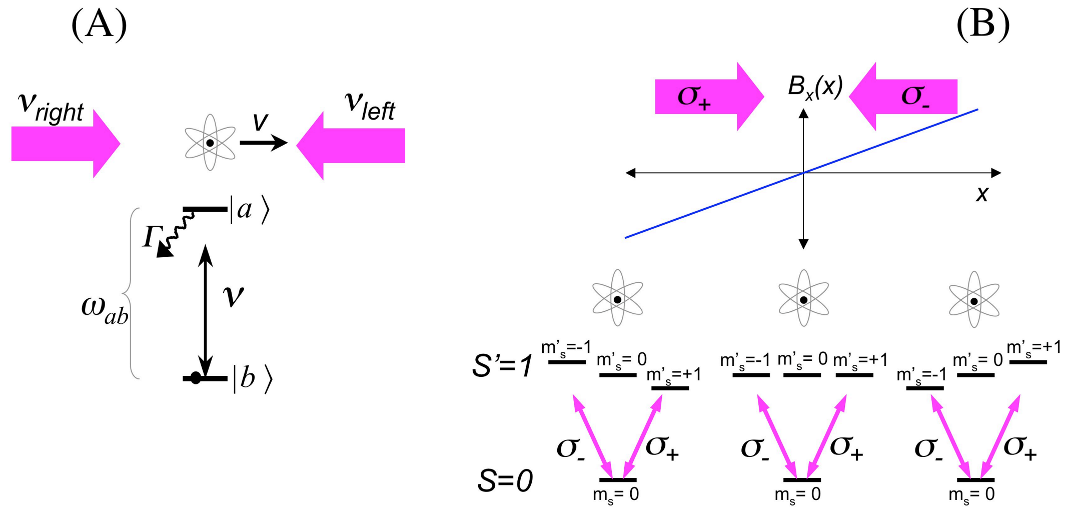

Figure 2.5: (A) Moving atom interacting with two counterpropagating fields. (B) Atom in magnetic field gradient interacting with two counterpropagating beams with opposite circular polarizations.

2.3 Atom Cooling and Trapping

2.3.1 Magneto Optical Trap

Consider a two level atom in the field of two counter-propagating light beams with frequencies ν_{left} and ν_{right} Fig.2.5A. For simplicity, we assume perpendicular polarization of the two beams to avoid the formation of a standing wave. If the atom is moving with velocity v to the right, then due to Doppler shift it will see the frequencies of the beams as $\nu'_{left} = \nu_{left}(1 + \frac{v}{c})$ and $\nu'_{right} = \nu_{right}(1 - \frac{v}{c})$. For the case of beams detuned to the red of the atomic transition, i.e. when $\nu_{left} = \nu_{right} = \omega_{ab} - \delta$ with $\delta < 0$, the atom will see the beam propagating leftwards as more resonant and will scatter photons from this beam at a higher rate then from the beam propagating rightwards. A similar situation will occur if the atom moves to the left, only this time the rightwards-propagating beam will be more resonant and thus scatter more photons. The difference between the scattering rate from the two beams gives rise to a velocity dependent damping force [65]:

$$F(v) = F_{right} - F_{left} = \hbar k \frac{\Gamma}{2} \frac{I}{I_{sat}} \left(\frac{1}{1 + \left[\frac{2(\delta - kv)}{\Gamma}\right]^2} - \frac{1}{1 + \left[\frac{2(\delta + kv)}{\Gamma}\right]^2} \right) \tag{2.35}$$

that will effectively cool the atoms in one dimension. Here $k = \frac{\nu}{c}$, $I = \frac{1}{2}\epsilon_o c|E|^2$ denotes the intensity of each beam, and $I_{sat} = \frac{\hbar\nu\Gamma}{2\sigma_o}$ is the saturation intensity of the atomic transition. For small velocities, $v \ll \frac{\Gamma}{k}$, $F(v) \approx -\alpha v$, with

$$\alpha = 2\hbar k^2 \frac{\left(2\frac{I}{I_{sat}}\right)\left(\frac{2\delta}{\Gamma}\right)}{\left(1+\left[\frac{2\delta}{\Gamma}\right]^2\right)^2}. \tag{2.36}$$

If we combine three perpendicular pairs of these beams the result will be cooling in all three dimensions. This cooling mechanism, referred to in the literature as Doppler cooling or "optical" molasses, is limited by by the random fluctuations of the atom's velocity that arise from spontaneous emission of the cooling beam photons by the atom, with the limit being $T_{Doppler} = \frac{\hbar\Gamma}{2k_B}$ [65].

While the mechanism described above will cool the atoms, it will not provide a spatial confinement mechanism since slowly moving atoms will be able to drift around in the beams. Spatial confinement is achieved for atoms with multiple Zeeman sublevels by adding a relatively weak inhomogeneous magnetic field with a zero at the beam intersection, $B_x = b\,x$, and by using opposite circular polarizations for each pair of the counterpropagating beams [78]. The simplest example of such atom would be an atom with a spin $S = 0$ ($m_s = 0$) ground state and a spin $S' = 1(m'_s = -1, 0, +1)$ excited state (Fig.2.5B) consisting of three degenerate (i.e. of the same energy) levels. Note that in this atom σ_+ light only couples state $|S = 0, m_s = 0\rangle$ to $|S' = 1, m'_s = +1\rangle$, while σ_- light couples state $|S = 0, m_s = 0\rangle$ to $|S' = 1, m'_s = -1\rangle$. This magnetic field can be provided, for example, by two coils with identical currents running in opposite directions – so called anti-Helmholtz configuration, which near the center actually provides approximately constant field gradients in all three spatial directions. In this setup, when an atom is displaced from the center $x = 0$ by $\Delta x > 0$, the degeneracy of the excited state will be lifted due to Zeeman effect. Each of the three levels, that originally had the same energy, will be shifted according to its m_s number by $\Delta E_Z = \mu m_s B = g_s \mu_B b m_s x$, where $\mu_B = \frac{e\hbar}{2m_e}$ is the Bohr magneton and $g_s \approx 2$ is the electron spin g-factor. Consequently, the atom will become more resonant with the leftward beam than with the rightward beam and the difference in the scattering rate from the two beams will result in a restorative force that will push it back towards the origin. A similar thing happens when $\Delta x < 0$, except now the magnetic field will shift the levels in the opposite direction and the atom will be more resonant with the rightward beam. The overall force on he atom will then be:

$$\begin{aligned} F(\Delta x, v) &= F_{right} - F_{left} \qquad (2.37) \\ &= \hbar k \frac{\Gamma}{2} \frac{I}{I_o} \left(\frac{1}{1+\left[\frac{2(\delta - kv - \beta\Delta x)}{\Gamma}\right]^2} - \frac{1}{1+\left[\frac{2(\delta + kv + \beta\Delta x)}{\Gamma}\right]^2} \right) \end{aligned}$$

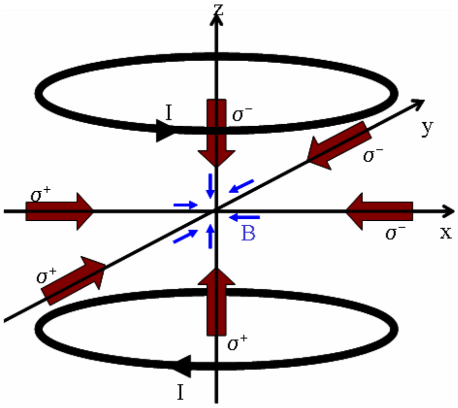

Figure 2.6: The complete MOT schematics. Figure taken from [22].

where $\beta = \frac{\mu b}{\hbar}$. For small enough Δx and v, 2.37 can be aproximated as

$$F(\Delta x, v) \approx 2\hbar k \frac{\left(2\frac{I}{I_o}\right)\left(\frac{2\delta}{\Gamma}\right)}{\left(1 + \left[\frac{2\delta}{\Gamma}\right]^2\right)^2}(-\beta\Delta x - kv). \tag{2.38}$$

Since a pair of anti-Helmholtz coils provides a field gradient in all three directions, this trap can be realized by simply adding the coils to the 3-D Doppler cooling setup discussed earlier as seen in Fig. 2.6. This trap can be loaded from room temperature vapor from which it collects the atoms from the low velocity tail of the Maxwell-Boltzmann distribution. Naturally, atoms will be lost from this trap when they collide with the fast atoms in the surrounding vapor and the MOT thus has an equilibrium size in terms number of trapped atoms when the loss rate and the capture rate become equal. In our case this technique allowed us to collect a cloud of $\sim 10^7$ atoms cooled to $\sim 140\mu K$ for $\delta \approx -\frac{\Gamma}{2}$. An additional decrease of the trapped atom temperature by a factor of ~ 3 can be achieved by shutting off the magnetic field, usually after the MOT is close to or has reached equlibrium, increasing δ to $\sim -5\Gamma$, and letting the cloud expand for a short time in the field of the trapping beams. This technique is called polarization gradient cooling [26] and its cooling mechanism is described as Sisyphus cooling [65]. The name comes from the nature in which energy is removed, when the slowly moving atoms climb a a series of potential hills – in this case created by the superposition of the counterpropagating σ_+ and σ_- fields – that are switched into potential valleys when the atoms get to the top.

Temperature measurement

The temperature of the laser-cooled atomic cloud can be measured by monitoring the cloud's expansion in free space after the cooling beams are shut off. The approach that we used involved taking absorptive pictures of the expanding cloud and measuring its radius. For a cloud with an initial Gaussian spatial density distribution and a Maxwell-Boltzmann velocity distribution, the time-dependent radius along direction $i \in \{x, y, z\}$ can be described by

$$r_i^2(t) = r_{oi}^2 + v_{oi}^2 t^2, \tag{2.39}$$

where r_{oi} is the initial radius of the cloud in the i direction and the spread velocity $v_{oi} = \sqrt{\frac{2kT_i}{m}}$ is given by the atoms' temperature in that particular direction.

2.3.2 Magnetic Traps

These traps are based on gyroscopically stabilized precession of a magnetic moment in a magnetic field. An atom with a magnetic moment $\vec{\mu} = \gamma_\mu \vec{J}$ placed in a magnetic field $\vec{B}$ will experience a potential $V = -\vec{\mu} \cdot \vec{B}$. Here $\vec{J}$ is the angular momentum and γ_μ is the moment's gyromagnetic ratio. As a result, the magnetic field will exert a torque $\vec{\mathcal{T}} = \vec{\mu} \times \vec{B}$ on the magnetic moment, causing it to precess with angular frequency $\omega_L = -\gamma_\mu B$. Consider an inhomogeneous magnetic field such as the one in Fig. 2.7, in which $B_x(x, y) = b\,x$, $B_y(x, y) = b\,y$ and thus $\vec{B}(0, 0) = 0$. In such a field, an atom with magnetic moments aligned with $\vec{B}$ will be attracted towards regions of high $|\vec{B}|$ and will move away from the origin. Such an atom is called a "high-field seeker". On the other hand, an atom with magnetic moment anti-aligned to $\vec{B}$, so called "low-field seeker", will be subjected to a force in the direction in which the magnetic field decreases due to their effort to minimize the potential energy. This will of course attract them to the origin, in the vicinity of which two things can happen depending on the atom's trajectory. If the atom passes directly through the origin (red trajectory in Fig. 2.7), its magnetic moment will become aligned with the magnetic field and the atom will be lost, as it just turned into a "high-field seeker". This is called a"Majorana flop". On the other hand, if the change of the magnetic field along the atom's trajectory remains smaller than its magnetic moment's precession frequency, the magnetic moment will follow the change in the magnetic field and stay anti-aligned (gray trajectory in Fig. 2.7). An atom on such trajectory will thus become trapped due to the attractive force towards the minimum in $|\vec{B}|$. In the weak field limit, the depth of the trap can be described by the Zeeman effect, which shifts the energies of the atom's states. An atom in an state whose energy is shifted upwards will thus be a "low-field seeker," while an atom in a state whose energy is shifted downwards will become a "high-field seeker." For an atom in a state described by quantum numbers $|J, F, m_F\rangle$, the trap depth is given by

$$U = \mu_B g_F m_F B \tag{2.40}$$

where $\mu_B = \frac{e\hbar}{2m_e}$ is the Bohr magneton and g_F is the Landé g-factor.

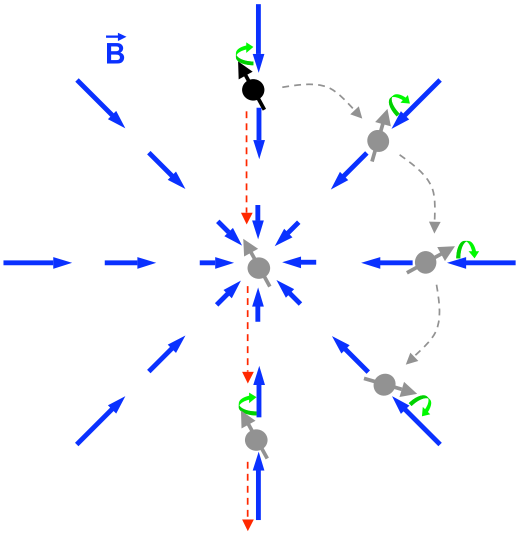

Figure 2.7: Magnetic trap. Magnetic moments on trajectories avoiding the $B = 0$ region at the origin will follow the direction of the magnetic field. This allows them to stay in the low field seeking state attracted to the origin. When a magnetic moment passes through the origin though, it will come out as a high field seeker and will be lost.

Due to the limited practically achievable depths, magnetic traps are usually loaded with atoms pre- cooled, for example, by a MOT, and optically pumped into the appropriate Zeeman state. For $\mu_B g_F m_F \frac{\partial B_z}{\partial z} \gg g$, the trap will keep the atoms confined against gravity and allow the atomic cloud to “hover” in free space.

In addition to collisions with room temperature background gas in the vacuum system, losses from this trap come mainly from Majorana flops and other mechanisms causing undesired changes magnetic moment direction, such as certain types of collisions between the trapped atoms. Under sufficiently good vacuum conditions and with implementation of techniques that prevent Majorana flops, lifetimes of tens of seconds can be achieved in this trap. Additionally, magnetically trapped atomic clouds can be transported around the experimental system by moving the magnetic field minimum.

2.3.3 Optical Dipole Trap

Consider a two level atom placed placed into the field E of a far detuned, $|\Delta| = |\nu_{laser} - \omega_{ab}| \gg \Gamma$, laser beam. Interaction with the field will lead to an energy shift

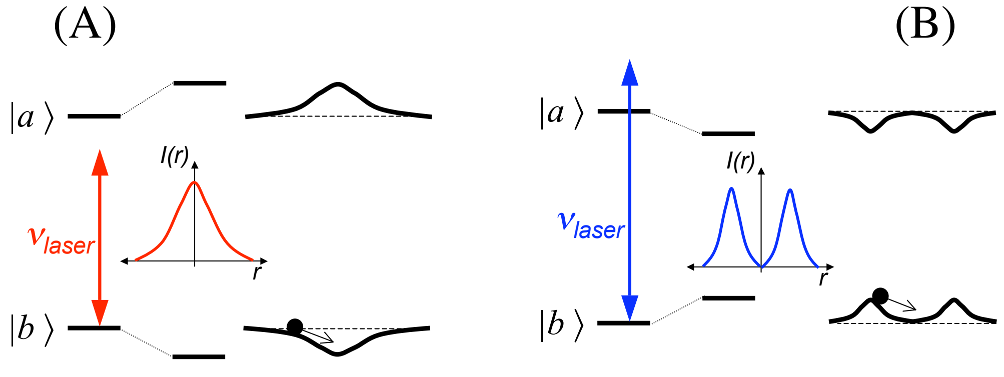

Figure 2.8: Level shifts and dipole trap potentials for a two level atom. (A) For red detuned light ($\Delta < 0$), a beam with a Gaussian profile creates an attractive potential for atoms in the ground state. (B) For a blue detuned light ($\Delta > 0$), an attractive potential for the atoms in the ground state can be created from a hollow beam.

of the atomic states, also known as AC-Stark shift [39]

$$\Delta E = \pm\frac{|\langle e|\mu|g\rangle|^2}{\Delta}|E|^2 = \pm\frac{3\pi c^2}{2\omega_{ab}^3}\frac{\Gamma}{\Delta}I. \tag{2.41}$$

Here the plus (minus) sign corresponds to the ground (excited) state and $I = I(r)$ is the spatially dependent laser beam intensity. Consequently, for re-detuned fields, $\Delta < 0$, the atom in its ground state $|b\rangle$ will be attracted into a high intensity region of the beam, while for blue-detuned fields, $\Delta > 0$, the atom in its ground state will be attracted towards low intensity areas of the beam (Fig. 2.8).

Thus, a single beam with a Gaussian spatial profile tuned below resonance can create a three dimensional nearly harmonic potential for atoms in its focal spot. This process is similar to trapping dielectric particles with optical tweezers due to their induced dipole moment [6]. The maximum depth of this trap will be

$$U_{dip} = \frac{3\pi c^2}{2\omega_{ab}^3}\frac{\Gamma}{\Delta}I_o, \tag{2.42}$$

with I_o being the maximum beam intensity at the focus, and the trap will be approximately harmonic near the center.

Similar to the case of magnetic traps, optical dipole traps are usually loaded with atoms that were initially cooled in a MOT, but optical pumping into a particular level of the ground state is often not necessary. In addition to collisions with background gas, the lifetime of atoms in this trap are limited by the atoms' scattering of photons from the trapping beam at a rate

$$\Gamma_{sc} = \frac{3\pi c^2}{2\omega^3}\left(\frac{\Gamma}{\Delta}\right)^2 I(r). \tag{2.43}$$

However, given that the trap depth is $\sim \frac{\Gamma}{\Delta}$ and the scattering rate scales as $\sim \left(\frac{\Gamma}{\Delta}\right)^2$, the heating can be suppressed to almost negligible levels with sufficiently large detuning. Experimentally observed trapping times at the order of seconds are routinely reported in the literature.

Compared to red-detuned dipole traps, blue-detuned traps are somewhat more difficult to set up as they either require a set of several Gaussian beams formed into sheets with cylindrical lenses or the use of non-Gaussian optics such as axicons, phase plates, or holograms. Their main advantage is that the atoms spend most of the time in the dark and thus the scattering-induced heating is greatly reduced. Consequently, fields with smaller detuning can be used which allows one to achieve deep traps even with relatively low laser power.

Finally, optical dipole traps at a “magic” wavelength are an interesting special case. At such a wavelength of the trapping light, the energy shift of both the ground state and the excited state will be identical due to the trap light’s interaction with the higher excited states of the atom. This has important implications for spectroscopy measurements done on atoms confined in this way, since it removes the dependence of the results on the intensity and beam-shape of the trapping light, and on the distribution of the atoms in the trap.

Chapter 3

Stationary pulses of light

Several techniques to generate stationary light pulses in an atomic medium have recently been proposed [54, 4]. The present work is related conceptually to the ideas of Ref. [4], but here we use a different approach in which the spatial modulation of the optical properties of the EIT medium is achieved by using two counter-propagating control fields. This approach, in the ideal limit, involves spatial modulation only of the absorptive properties of the medium. The use of such a dissipative effect for coherent control of light is a novel phenomenon, closely related to earlier work on matched pulse propagation in EIT [42, 16]. Although there exists a substantial body of work on localization of light in random dielectrics [18], Bragg gratings, and photonic bandgap materials [55, 93, 83], the unique feature of the present method is that it allows us to accurately control the creation of a stationary light pulse and its release. Conceptually, we are able to radically change the properties of an optical medium – from being completely transparent to behaving like a mirror constructed from multiple thin layers of two alternating dielectrics – on time scales significantly shorter than the time the propagating light pulse spends inside the medium.

The present method can be understood qualitatively by considering a three-state "lambda" configuration of atomic states (Figure 3.1). A large ensemble of N stationary atoms is initially prepared in the ground state $|g\rangle$. We use forward and backward control beams, with time varying Rabi-frequencies $\Omega_+(t)$ and $\Omega_-(t)$, respectively, to manipulate a weak pulse of signal light. In our experimental realization the two control fields have identical frequencies but opposite propagation directions. Usually, EIT [13] corresponds to simultaneous propagation of the forward control and signal beams. When their frequency difference matches the level splitting between the ground state and a metastable ("spin-flipped") state $|s\rangle$ the medium becomes transparent for the signal light, while the sharp atomic dispersion allows one to slow and localize an input signal pulse in the medium [46, 52]. By turning the control beam off while the pulse is in the medium [33], the signal amplitude vanishes while its state is stored in a stationary spin coherence. This atomic excitation can be converted back into a light pulse, propagating in the forward or backward direction, by application of the corresponding control beam [60, 76, 98]. The atomic coherence can be converted into a stationary photonic excitation if the medium is illuminated simultaneously by forward and backward control beams. Specifically, if the two create a standing wave pattern, the EIT effect suppresses the signal absorption everywhere but in the nodes of the standing wave, resulting in a sharply peaked, periodic modulation of the atomic absorption for the signal light (Figure 3.1B). Illumination by these beams also results in partial conversion of the stored atomic spin excitation into sinusoidally modulated signal light, but the latter cannot propagate in the medium due to Bragg reflections off the sharp absorption peaks, resulting in vanishing group velocity of the signal pulse. Only after one of the control beams is turned off does the pulse acquire a finite velocity and thus can leave the medium in the direction of the remaining control beam.

3.1 Dark-state polariton picture

To quantify these effects theoretically, consider the interaction of atoms with resonant optical fields represented by plane waves. We decompose the signal field into components propagating in the forward and backward directions along the z axis with wave-vectors $\pm k$ and slowly varying amplitudes $\mathcal{E}_\pm$.

Following [33, 4] we introduce two components $\Psi_\pm$ of a coupled excitation of light and an atomic spin wave ("dark-state polariton") corresponding to forward and backward signal fields, respectively. In the experimentally relevant case of small group velocities, the polariton components are represented by $\Psi_\pm = g\sqrt{N}\mathcal{E}_\pm/\Omega_\pm$, where g is the atom-field coupling constant [82]. Further assuming slowly varying pulses and negligible spin decoherence, we find that the components evolve according to

$$\begin{aligned} \frac{\partial}{\partial z}\Psi_+ &= -\alpha_-\xi(\Psi_+ - \Psi_-) - \frac{1}{c}\frac{\partial}{\partial\tau}(\alpha_+\Psi_+ + \alpha_-\Psi_-), \\ \frac{\partial}{\partial z}\Psi_- &= -\alpha_+\xi(\Psi_+ - \Psi_-) + \frac{1}{c}\frac{\partial}{\partial\tau}(\alpha_+\Psi_+ + \alpha_-\Psi_-) \end{aligned} \tag{3.1}$$

and the spin coherence $S = N^{-1/2}(\alpha_+\Psi_+ + \alpha_-\Psi_-)$ with $\alpha_\pm = |\Omega_\pm|^2/(|\Omega_+|^2 + |\Omega_-|^2)$. A detailed derivation of these equations, which describe two slow waves coupled due to periodic modulation of atomic absorption and group velocity, can be found in Ref. [2]. The first term in the right hand side of (3.1) is proportional to an absorption coefficient ξ near resonant line center. When ξ is large this term gives rise to the pulse-matching phenomenon [42, 41]: whenever one of the fields is created the other will adjust itself within a short propagation distance to match its amplitude such that $\Psi_+ - \Psi_- \to 0$. The scaled time, $\tau(t) = \int_0^t dt(|\Omega_+|^2 + |\Omega_-|^2)/g^2N$, reflects the group velocity reduction associated with atomic dispersion.

Finally, the center frequency of the signal light was chosen to match its wave-vector to that of the periodic absorption grating created by the standing wave formed

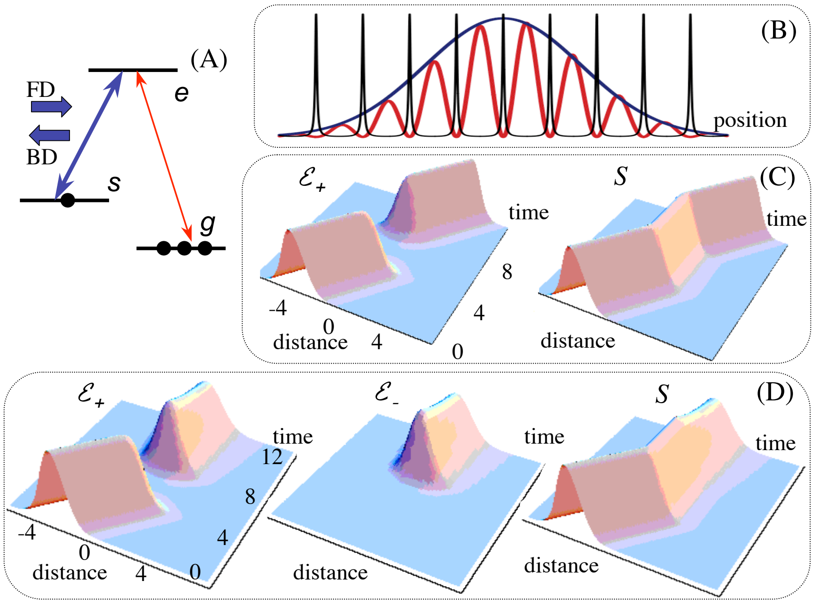

Figure 3.1: Physics of stationary pulses of light. (A) Schematic of the atomic system. The signal beam (red arrow) is resonant with the transition from the ground to the excited state ($|e\rangle$) and the control fields (blue arrows) are tuned to resonance between the $|s\rangle$ state and the excited state. (B) Schematic illustration of the spatial variation of the medium absorption (black line), and the electric field (red line) in the stationary pulse in the medium along the direction of the control beam. Blue line represents initial atomic spin coherence. (C) Storage of the weak signal pulse in Raman coherence. Calculated evolution is shown for the forward signal pulse and atomic spin wave amplitudes as a function of distance (in the units of compressed pulse length l) and time (in units of l/v_g^0). While the forward pulse propagates the forward control beam is turned off (at the time $t = 4l/v_g^0$) and the pulse is stored in a stationary spin coherence. At the time $t = 8l/v_g^0$ the forward control field is turned back on re-creating the propagating pulse. Calculations are based on Eqs.(3.1) with Gaussian pulses and $\alpha_+ = 1, \alpha_- = 0$. Figure (D) shows calculated evolution of the forward and backward signal components and atomic spin wave amplitude for the case when the stored coherence is illuminated (at the time $t = 8l/v_g^0$) by forward and backward control beams with equal Rabi-frequencies. Here stationary signal pulses are created. The main contributions to the dynamics include a slow spreading of the amplitudes as well as small shifts (on the order of $1/\xi$) of forward and backward components in the corresponding directions relative to the atomic coherence. Calculations are based on Eqs.(3.1) with $\alpha_+ = \alpha_- = 1/2, \xi l = 10$. All simulations assume that $v_g \ll c$, in which case the polaritons are mostly atomic and amplitude of the spin coherence does not change significantly while the pulse is in the medium. Amplitudes of fields and coherence are normalized to their initial value at $t = 0$.

by the forward and backward control fields. Due to the steep atomic dispersion, this condition can in the ideal limit be satisfied by a small detuning of the signal light, in direct analogy with other EIT-based processes [42].

In the case of the forward signal field propagating in the presence of only one (forward) control field, (3.1) has a simple solution $\Psi_+(z,t) = \Psi_+(z - c\tau(t), 0)$, which describes a coherent deceleration as shown in Figure 3.2C. Specifically, when the forward control beam is turned off, the polariton is stopped, the signal light vanishes, and a stationary spin excitation is created. Note that the spatial length of the spin excitation l is determined by the length of the compressed pulse corresponding to a product of the input pulse duration and the initial group velocity v_g^0. Finally, when the forward control beam is turned back on, the propagating signal pulse is re-created.

When both control beams are turned on simultaneously, forward and backward signal components are both generated. The electric field amplitudes for both forward and backward signal light are proportional to the amplitudes of the corresponding control fields, as required by the pulse matching condition [42, 41]. Interesting insight into the propagation dynamics can be gained by considering the dispersion relation associated with Eqs. (3.1): $\omega = -ck(\xi[\alpha_+ - \alpha_-] - ik)/(\xi - ik[\alpha_+ - \alpha_-])$, where ω is the Fourier frequency corresponding to the scaled time τ and k is the spatial wave-vector of the signal pulse envelopes. For small wave vectors and a large absorption coefficient, this corresponds to a linear dispersive medium with a group velocity $v_g = c \times (|\Omega_+|^2 - |\Omega_-|^2)/g^2 N$. Thus, the time-domain solution describes the coupled motion of the $\Psi_\pm$ envelopes at a group velocity proportional to the intensity difference between the two control fields. When the control Rabi frequencies are identical, the group velocity v_g vanishes and a stationary pulse of light is created as illustrated in Figure 3.1D. The electric field amplitudes of the two signal components are then equal $\mathcal{E}_+ = \mathcal{E}_-$, corresponding to sinusoidally modulated signal amplitude, and the dispersion relation becomes $\omega = ick^2/\xi$. In the time-domain this corresponds to a slow spreading of the stationary pulse at a rate $\delta l/l \sim c\tau/(\xi l^2)$, which determines the maximal holding time. Hence, in an optically dense medium ($\xi l \gg 1$) a stationary photonic excitation can be controllably created.

3.2 Making a mirror out of an atomic ensemble

To gain deeper understanding of the properties of an EIT system with two counter propagating control fields, we will now analyze in more detail the behavior of the medium with time-independent control fields in order to see the effects probe and control field frequency variations have on the system's mirror-like features.

Additionally, it is interesting to compare the system's behavior for various experimentally relevant temperature limits – an ensemble of "frozen" atoms with all atomic motion suppressed, an ensemble of cold or ultra-cold atoms where during the time the pulse is stationary the atoms move on average by distance less or comparable to the wavelength of the light, and an ensemble of hot or room-temperature atoms where the atoms on average move by many wavelengths during this time. We will see that while applying two counter-propagating control fields will turn the EIT system into a mirror-like structure for both the cold and hot atomic ensembles, there will be some notable differences.

We will use two approaches for this. The first approach follows the qualitative Bragg grating picture from the beginning of the chapter and requires a medium consisting of motionless atoms. The second approach uses a simplified version of Maxwell-Bloch equations and treats the system as a wave mixing problem. While the second approach is still valid in the limit of "frozen" atoms, it can take into account the thermal atomic motion washing out the Bragg grating imprinted by the standing wave formed by the control fields. We will see that both approaches yield equivalent sets of equations coupling the forward and backward propagating probe fields.

3.2.1 Coupled modes in a Bragg grating

For an idealized system, in which the atoms are completely at rest, for equal Rabi frequencies of the forward and backward control fields, $\Omega_+ = \Omega_- = \Omega_c$, the medium's spatially dependent susceptibility can be directly inferred from (2.29) as

$$\chi(\omega, z) = \frac{n\sigma_o\Gamma}{4}\frac{\tilde{\gamma} - i\omega}{(\tilde{\Gamma} - i\omega)(\tilde{\gamma} - i\omega) + |\Omega_c|^2\cos^2(k_c z)} \tag{3.2}$$

where $k_c = \frac{\nu_c}{c}$. For on-resonant control and probe fields, this results in medium with narrow Lorentzian absorption spikes with amplitude $\frac{\sigma_o n}{2}$ spaced by distance $\frac{\lambda_c}{2}$ as in Figure 3.1B.

Following the treatment in [2], we can write the Maxwell's equation for a spatially modulated medium in 1D

$$c^2\frac{\partial^2}{\partial^2 z}E(z,\nu) + \nu^2[1 + \chi(z,\nu)]E(z,\nu) = 0 \tag{3.3}$$

where $E(z,\nu) = \mathcal{E}_+(z,\omega)e^{ik_p z} + \mathcal{E}_-(z,\omega)e^{-ik_p z}$ with $\omega = \nu - \nu_p$. Here $k_p = \frac{\nu_p}{c}$ and ν_p is the carrier frequency of the probe field. Taking the Fourier series expansion of (3.2) $\chi(z,\omega) = \sum_n \chi_n(\omega)e^{ink_c z}$ and comparing the terms with the same spatial frequency in (3.3), we obtain a set of equations describing the coupling between the forward and backward propagating probe fields:

$$\begin{aligned} \left(-i\omega + c\frac{\partial}{\partial z}\right)\tilde{\mathcal{E}}_+ &= i\left(c\Delta k + \frac{\nu_p}{2}\chi_0\right)\tilde{\mathcal{E}}_+ + i\frac{\nu_p}{2}\chi_2\tilde{\mathcal{E}}_- \\ \left(-i\omega - c\frac{\partial}{\partial z}\right)\tilde{\mathcal{E}}_- &= i\frac{\nu_p}{2}\chi_{-2}\tilde{\mathcal{E}}_+ + i\left(c\Delta k + \frac{\nu_p}{2}\chi_0\right)\tilde{\mathcal{E}}_- \end{aligned} \tag{3.4}$$

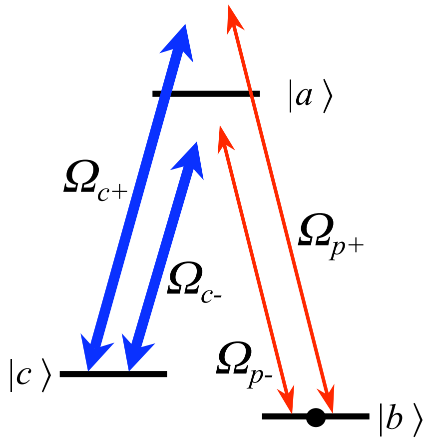

Figure 3.2: Three level system interacting with two counter-propagating probe fields and two counter-propagating control fields.

where we made the substitution $\mathcal{E}_{\pm} = \tilde{\mathcal{E}}_{\pm} e^{\mp i\Delta k z}$ with $\Delta k = k_p - k_c$ and we used $\chi_n(\omega) = \frac{k_c}{\pi}\int_0^{\pi/k_c} \chi(\omega, z) e^{-ink_c z} dz$. We find

$$\chi_0 = i\frac{2c}{\nu_p}\frac{\sigma_o n}{4}\frac{\Gamma}{\tilde{\Gamma} - i\omega}\sqrt{\frac{(\tilde{\gamma} - i\omega)(\tilde{\Gamma} - i\omega)}{(\tilde{\gamma} - i\omega)(\tilde{\Gamma} - i\omega) + |\Omega_c|^2}} \tag{3.5}$$

while

$$\chi_{\pm 2} = i\frac{2c}{\nu_p}\frac{\sigma_o n\Gamma}{4}\frac{k_c}{\pi}\int_0^{\frac{\pi}{k_c}} \frac{(\tilde{\gamma} - i\omega)e^{\mp 2ik_c z}}{(\tilde{\Gamma} - i\omega)(\tilde{\gamma} - i\omega) + |\Omega_c|^2 \cos^2(k_c z)} dz \tag{3.6}$$

will in general require numerical integration.

3.2.2 Wave mixing and Maxwell-Bloch equations

Consider a three-level system interacting with two counter-propagating probe fields, E_{p+} with carrier frequency ν_{p+} propagating forward with wave number $k_{p+} = \frac{\nu_{p+}}{c}$ and E_{p-} with carrier frequency ν_{p-} propagating backward with wave number $k_{p-} = \frac{\nu_{p-}}{c}$, and two counter-propagating control fields, E_{c+} with carrier frequency ν_{c+} propagating forward with wave number $k_{c+} = \frac{\nu_{c+}}{c}$ and E_{c-} with carrier frequency ν_{c-} propagating backward with wave number $k_{c-} = \frac{\nu_{c-}}{c}$ (Fig.3.2). The two probe fields couple state $|b\rangle$ to state $|a\rangle$ with Rabi frequencies $\Omega_{p\pm} = \frac{\mu_{ab}}{\hbar}\mathcal{E}_{p\pm}$ where $\mathcal{E}_{p\pm}$ are the slowly varying envelopes of the probe fields, while the two control fields couple state $|c\rangle$ to state $|a\rangle$ with Rabi frequencies $\Omega_{c\pm} = \frac{\mu_{ac}}{\hbar}\mathcal{E}_{c\pm}$. For simplicity, we will assume $\Omega_{c\pm} \gg \Omega_{p\pm}$. Note that the detunings of the fields from the atomic transitions,

$\delta_{p\pm} = \nu_{p\pm} - \omega_{ab}$ and $\delta_{c\pm} = \nu_{c\pm} - \omega_{ac}$ can also account for Doppler shifts in case of moving atoms.

In this system the forward and backward probe will be coupled by a range of wave mixing processes whose common feature is that they start with absorption of a single photon from one of the probe fields and conclude with emission into the other probe field. The simplest example of such a process would be a four-wave mixing process in which the atom sequentially absorbs a photon from E_{p+}, emits a photon into field E_{c+}, absorbs a photon from field E_{c+} and finally emits a photon into field E_{p-}. During this process the atom transfers temporarily into state $|c\rangle$, but returns back into state $|b\rangle$ at the end of the cycle. This process will lead to generation of E_{p-} even if the field was not originally present. The process can also be reversed, in which case it will start with absorption of a photon from E_{p-} and finish with emission of a photon into E_{p+}. In addition to four-wave mixing processes, in which the cycle consists of four events, the photons from E_{p+} can be converted into E_{p-} photons (and vice versa) in processes consisting of 6, 8, or more absorption/emission events. During these processes, in addition to the two photons from the probe fields, photons in the control fields will be absorbed/emitted. It is worth noting that for these process to be energy conserving, we require $\nu_{p+} - \nu_{c+} = \nu_{p-} - \nu_{c-}$.

To determine the effects of these mixing processes on the propagation of the probe fields, we will first calculate the medium's polarization density defined in section 2.2 of the previous chapter, $P = n(\mu_{ba}ab^* + \mu_{ab}a^*b)$. We will do this using a simplified version of the Maxwell-Bloch equations known as the stochastic wave-function apporach [37] and then combine the result with equation (2.14). In particular, we are interested in the components of the polarization density with spatial variations $\sim e^{ik_{p+}z}$ and $\sim e^{-ik_{p-}z}$ as these will dictate the evolution of the slowly varying envelopes $\mathcal{E}_{p\pm}$ of the probe fields in (2.14).

The hermitian part of the Hamiltonian for the system in Fig.3.2 will be

$$\begin{aligned}
\hat{H} = \quad & \hbar\omega_a b|a\rangle\langle a| + \hbar\omega_{cb}|c\rangle\langle c| \\
- \quad & \frac{1}{2}\mu_{ab}|a\rangle\langle b| \left(\mathcal{E}_{p+}e^{-i\nu_{p+}t}e^{ik_{p+}z} + \mathcal{E}_{p-}e^{-i\nu_{p-}t}e^{-ik_{p-}z}\right) \\
- \quad & \frac{1}{2}\hbar|a\rangle\langle c| \left(\Omega_{c+}e^{-i\nu_{c+}t}e^{ik_{p+}z} + \Omega_{c-}e^{-i\nu_{c-}t}e^{-ik_{p-}z}\right) + \text{c.c.}
\end{aligned} \tag{3.7}$$

If we assume the atom's wave-function to be $|\psi\rangle = a|a\rangle + b|b\rangle + c|c\rangle$ and use the stochastic wave-function approach, the Schroedinger equation will yield the following equations of motion for the wave-function's coefficients:

$$\begin{aligned}
\dot{a} &= -i\omega_{ab}a + i\frac{\mu_{ab}}{2\hbar}b\left(\mathcal{E}_{p+}e^{-i\nu_{p+}t}e^{ik_{p+}z} + \mathcal{E}_{p-}e^{-i\nu_{p-}t}e^{-ik_{p-}z}\right) \\
&\quad + \frac{i}{2}c\left(\Omega_{c+}e^{-i\nu_{c+}t}e^{ik_{p+}z} + \Omega_{c-}e^{-i\nu_{c-}t}e^{-ik_{p-}z}\right) \\
\dot{b} &= i\frac{\mu_{ab}}{2\hbar}a\left(\mathcal{E}^*_{p+}e^{i\nu_{p+}t}e^{-ik_{p+}z} + \mathcal{E}^*_{p-}e^{i\nu_{p-}t}e^{ik_{p-}z}\right)
\end{aligned} \tag{3.8}$$

$$\dot{c} = -i\omega_{cb}c + \frac{i}{2}a\left(\Omega^*_{c+}e^{i\nu_{c+}t}e^{-ik_{p+}z} + \Omega^*_{c-}e^{i\nu_{c-}t}e^{ik_{p-}z}\right)$$

where for now we have not included the decay channels. To remove the fast spatial oscillations from this set of equations, we employ the following substitutions:

$$\begin{aligned} a &= \sum_{m=0}^{\infty}\left(a_{+[2m+1]}e^{i[k_{p+}+mk_{c+}+mk_{c-}]z} + a_{-[2m+1]}e^{-i[k_{p-}+mk_{c+}+mk_{c-}]z}\right) \\ c &= c_0 + \sum_{m=1}^{\infty}\left(c_{+2m}e^{i[k_{p+}+(m-1)k_{c+}+mk_{c-}]z} + c_{-2m}e^{-i[k_{p-}+mk_{c+}+(m-1)k_{c-}]z}\right) \end{aligned} \tag{3.9}$$

which amounts to spatial frequency decomposition of the coefficients a and c.

In the special case of $\delta_{c+} = \delta_{c-}$, the wave-mixing processes will result in $\nu_{p+} = \nu_{p-} = \nu_p$. For cold atoms with negligible Doppler broadening, this means that both control fields have the same frequency. For hot atoms, this assumption can be safely made when both control fields have the same frequency and we work with the approximation from section 2.1 of the previous chapter that replaces Γ with Γ_D from (2.8) and σ_o with σ_{Dopp} from (2.9). In this special case, (3.8) can be further simplified by making the substitutions

$$\begin{aligned} a_{\pm[2m+1]} &= \tilde{a}_{\pm[2m+1]}e^{-i\nu_p t} \\ c_{\pm 2m} &= \tilde{c}_{\pm 2m}e^{-i[\nu_p-\nu_c]t} \end{aligned} \tag{3.10}$$

to remove the fast time dependences. Making these substitutions, followed by comparing the terms oscillating at the same spatial and temporal frequencies, results in the following set of differential equations, into which we now added the decay channels from (2.12) :

$$\begin{aligned} \dot{\tilde{a}}_{+1} &= -\tilde{\Gamma}_{+1}\tilde{a}_{+1} + i\frac{\mu_{ab}}{2\hbar}\mathcal{E}_{p+} + \frac{i}{2}\Omega_{c+}\tilde{c}_0e^{-i\Delta kz} + \frac{i}{2}\Omega_{c-}\tilde{c}_{+2} \\ \dot{\tilde{a}}_{-1} &= -\tilde{\Gamma}_{-1}\tilde{a}_{-1} + i\frac{\mu_{ab}}{2\hbar}\mathcal{E}_{p-} + \frac{i}{2}\Omega_{c-}\tilde{c}_0e^{+i\Delta kz} + \frac{i}{2}\Omega_{c+}\tilde{c}_{-2} \\ \dot{\tilde{c}}_0 &= -\tilde{\gamma}_0\tilde{c}_0 + \frac{i}{2}\tilde{a}_{+1}\Omega^*_{c+}e^{+i\Delta kz} + \frac{i}{2}\tilde{a}_{-1}\Omega^*_{c-}e^{-i\Delta kz} \end{aligned} \tag{3.11}$$

while for $m > 0$

$$\begin{aligned} \dot{\tilde{a}}_{\pm[2m+1]} &= -\tilde{\Gamma}_{\pm[2m+1]}\tilde{a}_{\pm[2m+1]} + \frac{i}{2}\Omega_{c\pm}\tilde{c}_{\pm 2m} + \frac{i}{2}\Omega_{c\mp}\tilde{c}_{\pm[2m+2]} \\ \dot{\tilde{c}}_{\pm 2m} &= -\tilde{\gamma}_{\pm 2m}\tilde{c}_{\pm 2m} + \frac{i}{2}\Omega^*_{c\mp}\tilde{a}_{\pm[2m-1]} + \frac{i}{2}\Omega^*_{c\pm}\tilde{a}_{\pm[2m+1]} \end{aligned} \tag{3.12}$$

for $m > 0$. Here $\Delta k = k_p - k_c$ and $\tilde{\Gamma}_{\pm[2m+1]} = \frac{\Gamma_{\pm[2m+1]}}{2} - i\delta_p$ and $\tilde{\gamma}_{\pm 2m} = \gamma_{\pm 2m} - i[\delta_p - \delta_c]$ are the complex decay rates of the components of the wave-function coefficients a and c with spatial frequencies $\sim (2m+1)k$ and $\sim 2mk$. In addition to the finite lifetimes of the states $|c\rangle$ and $|a\rangle$, the decay rates $\gamma_{\pm 2m}$ and $\Gamma_{\pm[2m+1]}$ will be determined by the thermal motion of the atoms since this motion will wash out the the periodicity of those higher-order components.) The coupling between $\mathcal{E}_{p+}$, $\mathcal{E}_{p-}$, and the medium's polarization density determined by a can be found by comparing the components of (2.14) with the same temporal and spatial frequencies, which yields:

$$\begin{aligned}\left(-i\frac{\omega}{c}+\frac{\partial}{\partial z}\right)\tilde{\mathcal{E}}_{+} &= i\Delta k\tilde{\mathcal{E}}_{+}+i\frac{n\sigma_o\Gamma}{2}\frac{\hbar}{\mu_{ab}}\tilde{a}_{+1}(\omega)e^{i\Delta kz} \\ \left(-i\frac{\omega}{c}-\frac{\partial}{\partial z}\right)\tilde{\mathcal{E}}_{-} &= i\Delta k\tilde{\mathcal{E}}_{-}+i\frac{n\sigma_o\Gamma}{2}\frac{\hbar}{\mu_{ab}}\tilde{a}_{-1}(\omega)e^{-i\Delta kz}\end{aligned} \tag{3.13}$$

where again we made the substitution $\mathcal{E}_{\pm}=\tilde{\mathcal{E}}_{\pm}e^{\mp i\Delta kz}$. We expect that after solving for $\tilde{a}_{\pm 1}$, (3.13) can be rearranged into the form

$$\begin{aligned}\left(-i\frac{\omega}{c}+\frac{\partial}{\partial z}\right)\tilde{\mathcal{E}}_{+} &= (i\Delta k+a_{11})\tilde{\mathcal{E}}_{+}+a_{12}\tilde{\mathcal{E}}_{-} \\ \left(-i\frac{\omega}{c}-\frac{\partial}{\partial z}\right)\tilde{\mathcal{E}}_{-} &= a_{21}\tilde{\mathcal{E}}_{+}+(i\Delta k+a_{22})\tilde{\mathcal{E}}_{-}\end{aligned} \tag{3.14}$$

which is equivalent to (3.4) and describes the same spatial-temporal dynamics as (3.1).

Hot atoms

Atoms at $T \approx 80\,^{\circ}\mathrm{C}$ will travel $\sim 260\ \mu m$ in $1\ \mu s$. For our experimental system, the spatial periodicity of c_0 is $\sim 4\ cm$, while the spatial periodicity of the $2m^{th}$ order component of c will be $\sim \frac{1}{m}\frac{\lambda}{2}$, where $\lambda \approx 795\ nm$ is the wavelength of the probe and control fields. Thus, at the time scales of the experiment, which in our case are μs, the hot atoms will move by many λ and any spatial dependency with periodicity $\sim \lambda$ or less imprinted on the atomic ensemble will be lost before it can have an effect on the probe propagation. We therefore set $\gamma_{\pm 2m} \to \infty$ for $m > 0$, which allows us to simplify (3.11) and (3.12) to

$$\begin{aligned}\dot{\tilde{a}}_{+1} &= -\tilde{\Gamma}_{+1}\tilde{a}_{+1}+i\frac{\mu_{ab}}{2\hbar}\mathcal{E}_{p+}+\frac{i}{2}\Omega_{c+}\tilde{c}_0e^{-i\Delta kz} \\ \dot{\tilde{a}}_{-1} &= -\tilde{\Gamma}_{-1}\tilde{a}_{-1}+i\frac{\mu_{ab}}{2\hbar}\mathcal{E}_{p-}+\frac{i}{2}\Omega_{c-}\tilde{c}_0e^{+i\Delta kz} \\ \dot{\tilde{c}}_0 &= -\tilde{\gamma}_0\tilde{c}_0+\frac{i}{2}\tilde{a}_{+1}\Omega^{*}_{c+}e^{+i\Delta kz}+\frac{i}{2}\tilde{a}_{-1}\Omega^{*}_{c-}e^{-i\Delta kz}\end{aligned} \tag{3.15}$$

by neglecting the higher-order components of a and c. Here, $\tilde{\Gamma}_{\pm 1}=\tilde{\Gamma}=\frac{\Gamma_D}{2}-i\delta_p$. Notice that spatial periodicity of c_0 given by Δk can survive for tens of μs before being washed out by the atomic motion. From the wave mixing point of view, the

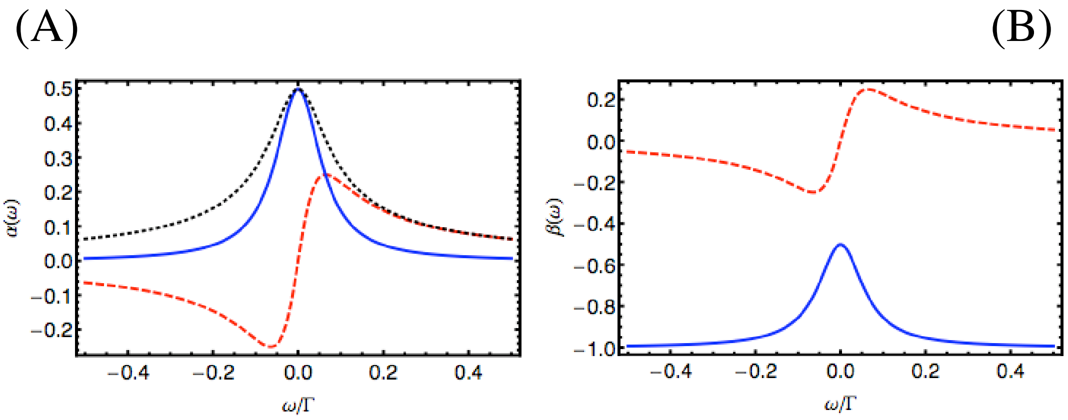

Figure 3.3: Hot atoms cross and self coupling terms. (A) The cross coupling term $\alpha = a_{12} = a_{21}$ from (3.14) as a function of ω in units of $\frac{n\sigma_{Dop}}{2}$: imaginary part (dashed, red), real part (solid, blue), and absolute value (black, dotted). (B) The self coupling term $\beta = a_{11} = a_{22}$ from (3.14) as a function of ω: imaginary (dashed, red) and real part (solid, blue). Here $\delta_c = \delta_p = 0$, $\frac{\Gamma_D}{2\pi} \approx 600\,\text{MHz}$, $\frac{\Gamma}{2\pi} = 6\,\text{MHz}$, and $\frac{\Omega_c}{2\pi} = 15\,\text{MHz}$.

thermal atomic motion suppresses all wave mixing processes, except for the two four-wave mixing processes described at the beginning of this subsection. Solving (3.15) will indeed allow us to rearrange (3.13) into the form of (3.14). In particular, for the special case of $\Omega_{c+} = \Omega_{c-} = \Omega_c$, we will find

$$\begin{aligned} a_{12} = a_{21} = \alpha &= \frac{n\sigma_{Dop}}{8}\frac{\Gamma_D}{\tilde{\Gamma} - i\omega}\frac{\frac{|\Omega_c|^2}{2(\tilde{\gamma}_0 - i\omega)}}{(\tilde{\Gamma} - i\omega) + \frac{|\Omega_c|^2}{2(\tilde{\gamma}_0 - i\omega)}} \qquad (3.16) \\ a_{11} = a_{22} = \beta &= -\frac{n\sigma_{Dop}}{4}\frac{\Gamma_D}{\tilde{\Gamma} - i\omega}\frac{\tilde{\Gamma} - i\omega + \frac{|\Omega_c|^2}{4(\tilde{\gamma}_0 - i\omega)}}{(\tilde{\Gamma} - i\omega) + \frac{|\Omega_c|^2}{2(\tilde{\gamma}_0 - i\omega)}} = -\frac{n\sigma_{Dop}}{4}\frac{\Gamma_D}{\tilde{\Gamma} - i\omega} + \alpha \end{aligned}$$

The plots of the frequency dependency of these cross coupling and self coupling terms from (3.14) for the case of hot atoms can be seen in Figure 3.3.

Cold atoms

At temperatures such as those in experiments described in Chapters 4 and 5, the atoms will move during the time scales of the experiment by distances $\sim \lambda$ or even less. For instance, at $T = 1\ mK$ the atom will move by $\sim \frac{\lambda}{2}$ in $1\ \mu s$, while at $T = 40\ \mu K$ – corresponding to rubidium atoms just released from a MOT followed by polarization gradient cooling – the atoms will move by $\sim \frac{\lambda}{10}$ in $1\ \mu s$. Thus for cold atomic ensembles, the higher spatial frequency components of a and c resulting

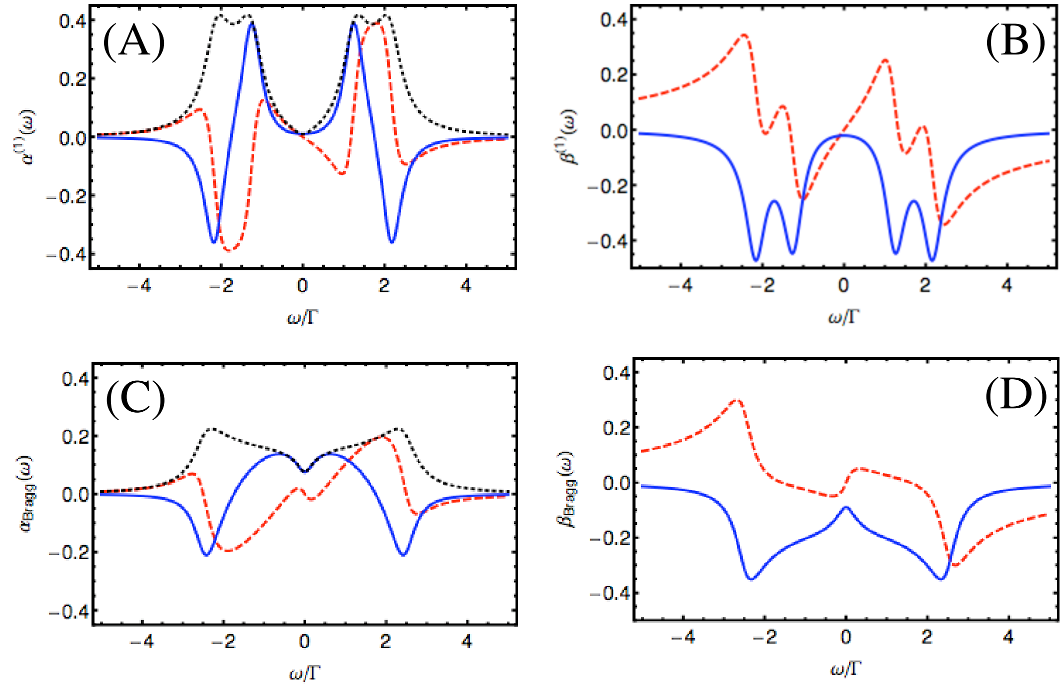

Figure 3.4: Cross and self coupling terms for cold atoms in units of $\frac{n\sigma_o}{2}$:imaginary part (dashed, red), real part (solid, blue), and absolute value (black, dotted). (A) The cross coupling term $\alpha^{(1)} = a_{12} = a_{21}$ and (B) the self coupling term $\beta^{(1)} = a_{11} = a_{22}$ resulting from the truncated solution (3.18) for cold but not stationary atoms. (C) The cross coupling term $\alpha_{Bragg} = a_{12} = a_{21}$ (3.6) and (D) the self coupling term $\beta_{Bragg} = a_{11} = a_{22}$ (3.5) obtained from the Bragg grating treatment valid for stationary atoms. Here $\delta_c = \delta_p = 0$, $\frac{\Gamma}{2\pi} = 6\,\text{MHz}$, $\frac{\gamma_0}{2\pi} = 0.1\,\Gamma$, and $\frac{\Omega_c}{2\pi} = 15\,\text{MHz}$.

from the higher-order wave mixing processes will not decay fast enough and cannot be neglected. Consequently, to calculate $\tilde{a}_{\pm 1}$ from (3.11), the contributions from terms described by (3.12) must also be taken into account. For very cold atoms, whose thermal movement is negligibly small as in the case of near BEC temperatures, the decay rates of the higher spatial frequency components of a and c will be independent of their order, which will present a dilemma about how many terms from (3.12) need to be included. For atoms at such low temperature, the coupled-mode approach from the previous subsection is therefore more practical.

On the other hand, the thermal motion of the atoms from the examples at the beginning of the previous paragraph will be sufficient to wash out some of the higher-order spatial terms but not all of them. For those cases, the proposed approach [31] for practical purposes is to define

$$\begin{aligned} \Gamma_{\pm[2m+1]} &= \kappa^m \Gamma \\ \gamma_{\pm 2m} &= \kappa^m \gamma_0 \end{aligned} \tag{3.17}$$

where $\kappa > 1$ is a temperature dependent fitting parameter that accounts for the increased sensitivity of the higher frequency spatial components to the thermal motion of the atoms.

Finally, one can take a somewhat heavy-handed approach of arbitrarily keeping only the terms $a_{\pm 1}$, c_0 and $c_{\pm 2}$ in expansion (3.9), and setting $\Gamma_{\pm 1} = \Gamma$ and $\gamma_{\pm 2} = \gamma_0$. This approach was proposed and used in [59] to describe their experimental demonstration of stationary light pulses in cold atomic ensembles. It provides a surprisingly good qualitative description of the significantly different behavior of cold atoms from hot atoms when it comes to stationary light pulse creation. Taking this approach and solving the truncated version of equations (3.11) and (3.12), one obtains

$$\begin{aligned} a_{11} = a_{22} = \beta^{(1)} &= -\frac{n\sigma_o\Gamma}{4} \frac{\tilde{\Gamma} - i\omega + \frac{|\Omega_c|^2}{2(\tilde{\gamma}_0 - i\omega)}}{\left(\tilde{\Gamma} - i\omega + \frac{|\Omega_c|^2}{2(\tilde{\gamma}_0 - i\omega)}\right)^2 - \frac{|\Omega_c|^4}{16(\tilde{\gamma}_0 - i\omega)^2}} \\ a_{12} = a_{21} = \alpha^{(1)} &= \frac{n\sigma_o\Gamma}{16(\tilde{\gamma}_0 - i\omega)} \frac{|\Omega_c|^2}{\left(\tilde{\Gamma} - i\omega + \frac{|\Omega_c|^2}{2(\tilde{\gamma}_0 - i\omega)}\right)^2 - \frac{|\Omega_c|^4}{16(\tilde{\gamma}_0 - i\omega)^2}} \end{aligned} \tag{3.18}$$

for the terms in (3.14) in the case when $\Omega_{c+} = \Omega_{c-} = \Omega_c$.

The plots of the frequency dependency of these cross-coupling and self-coupling terms from (3.14) for the case of cold atoms can be seen in Figure 3.4. Here we plotted both the results from (3.18) and the coupling terms obtained from the Bragg-grating-picture treatment in the previous subsection.

It is interesting to compare the behavior of the cross coupling term for $\delta_p = \delta_c = \omega = 0$, i.e. on resonance, for hot and for cold atoms. For hot atoms the absolute value of cross coupling term has a maximum on resonance, and thus the coupling between the forward and backward propagating probes is the strongest there. On the other hand, for cold atoms the absolute value of the cross-coupling has a minimum on resonance. In the limit $|\Omega_c|^2 \gg \tilde{\gamma}_0\tilde{\Gamma}$, the value of this minimum is $\alpha(\omega = 0) \rightarrow \frac{\sigma_o n \gamma_0 \Gamma}{3|\Omega_c|^2}$. At the same time, the condition for low loss propagation in an EIT medium in which $\gamma_0 \neq 0$ is $|\Omega_c|^2 \gg OD\ \gamma_0\Gamma$. As a result, we can expect that for realistic experimental conditions $\alpha(\omega = 0) \ll 1$, i.e. the coupling between the forward and backward propagating probe fields will be weak. This means that cold atoms will not make a very good mirror on resonance and that our scheme most likely will not lead to creation of stationary light pulses in cold atomic ensembles. The wave-mixing picture view of this would be that the higher-order wave-mixing processes, present in the case of cold atoms, will bypass the grating created by the standing wave control fields. This grating failure was observed experimentally by [59] and is theoretically explored in more detail in [71]. However, two variations on our method that resolve this problem and allow stationary pulse creation in cold atoms have been already proposed [59, 74]. The latter proposal is based on the forward and backward fields having opposite polarizations, while the former uses forward and backward control fields of slightly different frequencies and includes a successful experimental demonstration.

3.2.3 Phase matching

Processes based on either reflection from a Bragg grating or wave mixing work best when the phase-matching condition is satisfied [15]. Conceptually, this occurs when the wave number of the probe field is equal to the to the wavenumber of the pump field (grating) in the case of wavemixing (Bragg reflection). In our case, phase-matching can be attempted by minimizing the imaginary part of the complete self-coupling term in (3.14), $\tilde{\beta} = \beta + i\Delta k$. This can be accomplished in two ways – either by changing the probe carrier frequency such that $\delta_p < 0$ while keeping δ_c constant (Fig. 3.5A) or by changing the control field frequency such that $\delta_c > 0$ (Fig. 3.5B). However, the first option can not be used for creation of stationary light pulses in hot atomic ensembles. When a light pulse with $\delta_p \neq 0$, whose bandwidth is not significantly smaller than the EIT transparency window, is stored in an atomic ensemble and then retrieved with resonant control field, the retrieved pulse will have a carrier frequency with $\delta_p' = 0$. For experimentally realistic pulse storage in warm vapors, the relation between the bandwidth of the probe pulse τ_p and the EIT transparency window Δ_{FWHM} is $\tau_p \approx \Delta_{FWHM}$, and thus the initial phase matching arrangement will be lost during the storage and retrieval stages of the stationary pulse creation.

On the other hand, the second option in which $\delta_p - \delta_c$ is kept at zero but δ_c is adjusted such that $Im(\tilde{\beta})$ is minimized, preserves the initial phase matching arrangement during the whole stationary pulse creation process.

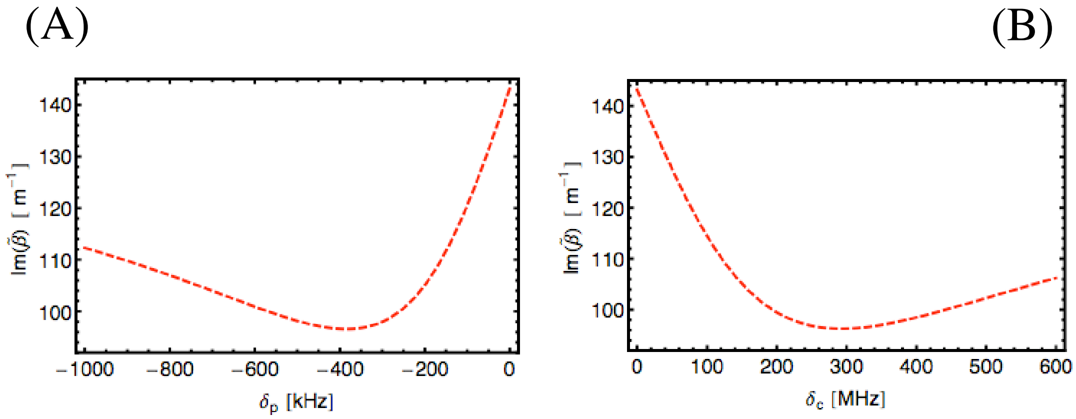

Figure 3.5: Phase matching in hot atoms. (A) Minimizing phase mismatch by adjusting δ_p while keeping $\delta_c = 0$. (B) Minimizing phase mismatch by adjusting δ_c while maintaining $\delta_p - \delta_c = 0$. Note the different frequency scale from (A). Here $\frac{\Gamma_D}{2\pi} \approx 600\,\text{MHz}$, $\frac{\Omega_c}{2\pi} = 15\,\text{MHz}$, and $n \approx 10^{12}\,cm^{-3}$.

3.3 Experimental results

Our experimental apparatus used to demonstrate these effects in a room-temperature atomic ensemble is shown in Figure 3.6 . A magnetically shielded 4 cm long ^{87}Rb vapor cell is maintained at T ∼ 90 °C (atom number density is $10^{12} - 10^{13}$ cm^{-3}). The signal field is generated by an extended cavity diode laser. The control beam, generated by a locked Ti:Sapphire laser, is split on a polarizing beam splitter (PBS) to provide both forward and backward control fields. The signal laser is phase-locked to the control laser with a frequency offset corresponding to the hyperfine splitting of ^{87}Rb (6.84 GHz). All three fields have circular polarizations in the cell but their intensities are controlled independently by acousto-optic modulators (AOMs). Programmable pulse generators which govern the AOM allow us to manipulate the timing, amplitude, duration and shape of the pulses independently. The beams overlap inside the cell at an angle of $\sim 10^{-4}$ rad. PD1 and PD3 are fast photodiodes used for heterodyne detection of the the signal amplitude using a reference beam (black line). These are followed by a spectrum analyzer running in zero span mode with a detection bandwidth of 3 MHz. The CW power of the signal beam is 250 μW, while the powers of the forward and backward control beams are independently adjusted between 8.0 mW and 40 mW. The beam size inside the cell is about 2 mm.

Long-lived hyperfine sublevels of the electronic ground state $S_{1/2}$ with $F = 1, 2$ are used as the storage states $|g\rangle, |s\rangle$, respectively, coupled via the excited state $P_{1/2}$. The hyperfine coherence time is limited by atomic diffusion out of the beam volume, and is enhanced with a Ne buffer gas of 6 torr (resulting in spin-coherence lifetimes in the

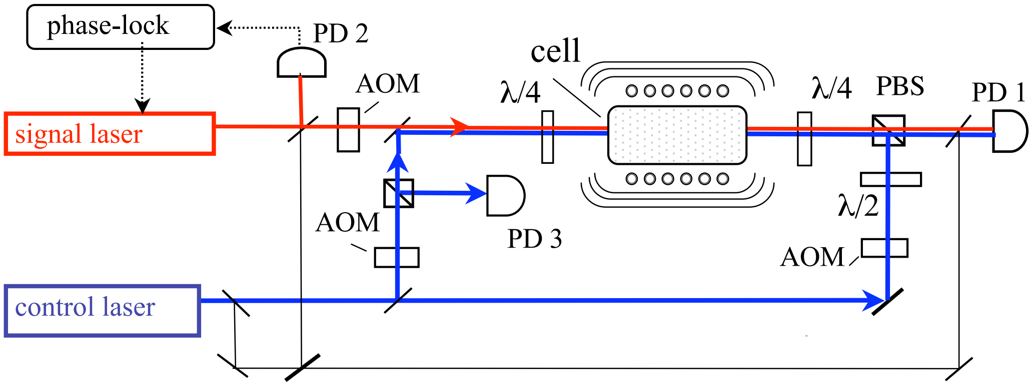

Figure 3.6: The experimental setup.

μs to ms range [52, 76]). Note that the Doppler shifts due to atomic motion do not directly affect the spin coherence when the control and the signal beams propagate colinearly in forward and backward pairs.

3.3.1 Continuous wave study

We first consider continuous wave (CW) excitation of the atomic Rb. Without the control beams the atomic medium is completely opaque to the forward signal beam. When the forward control field is present, a sharp, few-100-kHz-wide resonance appears in the transmission spectrum of the signal beam, corresponding to EIT (curve (i) in Fig.3.7A). Turning on the backward control beam in the CW regime greatly reduces the EIT transmission (curve (iii)), while at the same time generating a reflected signal beam that is detected in the backward direction (curve (ii)). The peak reflection is a substantial fraction (up to $\sim 80\%$) of the input signal beam. As discussed in the previous section, phase matching can be achieved by operating at a non-zero control field detuning as can be seen in Figure 3.8. This minimizes the difference between the frequency corresponding to peak EIT transmission and the frequency corresponding to peak reflection as predicted in Fig.3.5B.

These results demonstrate the possibility of coherent control of light via simultaneous driving of the medium with forward and backward control beams. Specifically, the signal light cannot propagate in the modulated EIT medium, but instead of absorbing the signal the medium reflects it as a high quality Bragg mirror. This effect is analogous to that predicted theoretically in [4]. However, the broad lineshape of the curve (ii) indicates that periodic modulation of the absorptive rather than dispersive properties are at the origin of the observed Bragg reflection [55]. We note, in particular, good agreement between the present experimental results and a theoretical model based on the resonant EIT medium with forward and backward control fields (Figure

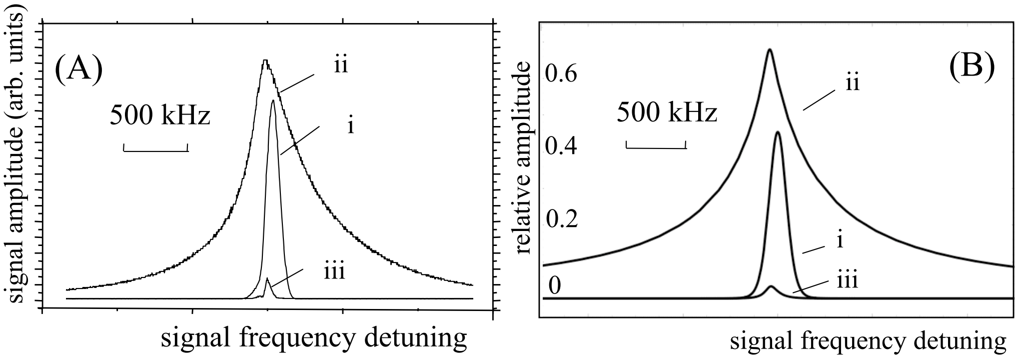

Figure 3.7: The results of CW experiments (A) Curve (i) represents the EIT signal transmission when the forward control beam is on and the backward control beam is off. Transmission is approximately 50% at EIT resonance. Curve (ii) is the reflected signal and curve (iii) is the signal transmission when both forward and backward control fields are on. (B) Corresponding theoretical simulations of the transmission and reflection of signal field from the medium composed of atoms in Figure 1A. Parameters correspond to atomic Rb, $\Omega_+ = \Omega_- = 2\pi \times 15$ MHz, the spin decoherence rate of 3 kHz, and medium length corresponding to resonant attenuation of e^{-15}. The small frequency shift in the reflection resonance accounts for wave-vector matching to satisfy Bragg condition.

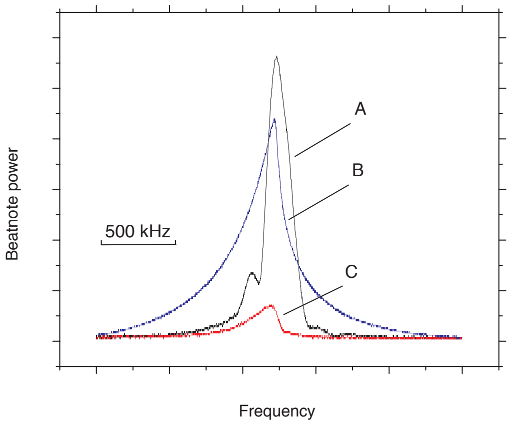

Figure 3.8: Phase matching with $\delta_p - \delta_c = 0$. The curve labels A-C correspond to labels i-iii in Figure 3.7, but instead of i $\delta_c \approx 0$ here $\delta_c \sim 200\,$MHz, roughly as predicted in Fig.3.5. The EIT and reflection peaks now occur at the same frequency.

3.7). At the same time, a qualitatively different lineshape is expected for dispersive Bragg gratings [4, 83].

3.3.2 Trapping a pulse of light

Turning to experiments with pulsed light, we first map the input signal pulse onto an atomic coherence of the Rb atoms [60, 76]. This procedure corresponds to Fig. 3.1C and its experimental observation is shown by curve (i) in Figure 3.9A. The atoms are first optically pumped into the lowest state using a 400 μs-long pulse of the forward control field. A Gaussian-shaped signal pulse of roughly 5 μs duration then enters the medium where it is slowed to $v_g^0 \sim 6\,\text{km/s}$. The forward control beam is subsequently turned off. As a rule, a fraction of the signal pulse leaves the cell before that time, leading to the first peak of the curve (i). When the forward control field is turned back on, the stored atomic excitation is converted back into light which is detected in the forward direction (second peak of the curve (i)). The amplitude of the retrieved light decays with increasing storage interval with a characteristic time scale of about 20 μs, corresponding to decay of the hyperfine coherence caused by atomic diffusion. Similar experimental results are obtained by detecting the signal light in the backward direction when the stored coherence is retrieved with the backward control beam [98].

We next consider the retrieval of the atomic excitations by simultaneous application of the forward and backward control beams. When the intensities of the beams are carefully adjusted, the output signal pulses in both the forward and backward directions are greatly suppressed (curves (ii) and (iii) in Figure 3.9A). Both channels exhibit small leakage. We attribute the first peak to photons retrieved near the cell boundaries, which do not experience sufficient Bragg reflections to be trapped efficiently. The long tail is likely due to a slow spreading of the stored pulse. When the backward control beam is turned off, the released pulse is detected in the forward channel (curve (ii)). During the pulsed experiments depicted here, the control and probe fields have detuning $\delta_c = \delta_p \sim 200MHz$ in order to keep close to the phase-matching condition in Fig.3.8. We observed similar results for $\delta_c = \delta_p \sim 0$, but the observed magnitude of the released stationary pulse was notably smaller. Additionally, the presence of signal light inside the cell during the simultaneous application of the two control beams was verified directly by monitoring fluorescence from the side of the cell (Figure 3.9B). For times when the signal output in the forward and backward directions is greatly suppressed, we observed significant enhancement of the signal light fluorescence (curve (iii) in Figure 3.9B) due to residual atomic absorption.

These observations provide evidence for controlled conversion of the stored atomic coherence into a stationary photonic excitation in the cell. Note, in particular, that the magnitude of the fluorescence drops sharply after the backward control pulse is turned off. This drop is followed by a gradual decay associated with the exit of the slow pulse from the medium. This behavior is in qualitative agreement with

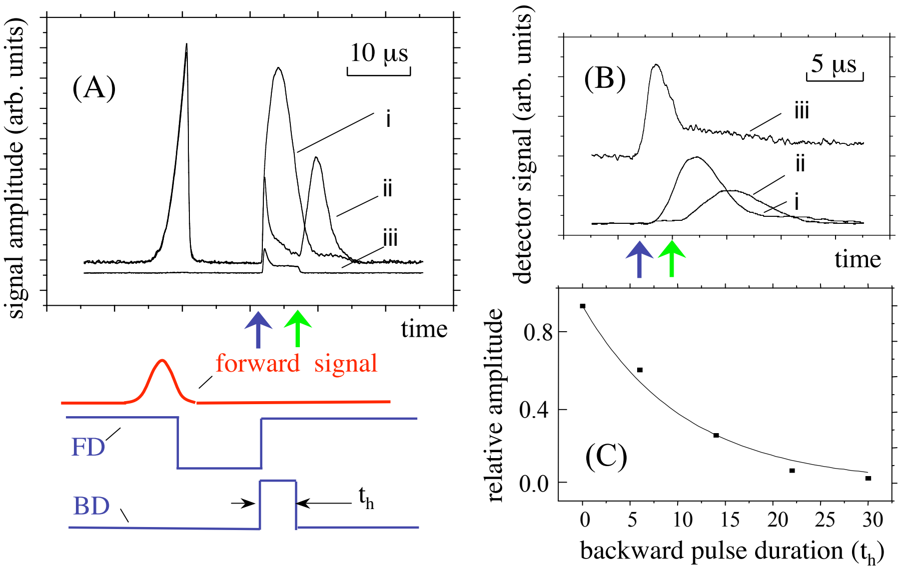

Figure 3.9: Results of pulsed experiments. (A) Detected output signals from the Rb cell. Curve (i) is the signal detected in the forward direction resulting from pulse storage in a spin coherence. The left peak represents the fraction of the signal pulse that leaves the cell before the trapping has begun. (We were able to suppress this fraction to $\sim$ 10 %.) It is delayed by $\sim$ 10 μs compared to the original pulse (see timing diagram below). The right peak in curve (i) appears only after the forward control is turned on, and thus represents the stored and retrieved signal. Curve (ii) is the same except the forward and backward control beams are both turned on as shown on the timing diagram and marked by the blue arrow. Curve (iii) is the signal in the backward direction under the same conditions. (This curve is plotted on a different scale with the peak signal about a factor of five weaker than that on curve (ii)). The pulse is released in the forward direction when the backward control is turned off (green arrow). On the timing diagram, the rise time edges of the control pulses are about 0.1 μs. Note that the frequencies of the two control fields do not need to be exactly equal. This is in agreement with theory and was verified by obtaining results similar to those in curve (ii) with backward control beam shifted by 80 MHz from the forward control beam. (B) Rb fluorescence measured at the side of the cell. Curve (iii) is fluorescence associated with signal light during the release with both forward and backward control beams on. Background fluorescence associated with control beams is subtracted. Curves (i) and (ii) (shown for reference) correspond to the same signals as curves (i) and (ii) in Fig.3A. Note that fluorescence measurements are carried out under conditions differing from those for other data (including Fig.3A) since the photodetector inserted inside the magnetic shields introduces stray magnetic fields resulting in shortened spin coherence and storage times; this measurement is also detection-bandwidth limited. (C) Dependence of the released signal pulse magnitude on the backward control pulse duration t_h.

our simple model, which predicts the light intensity in the stationary pulses to be double that of the slowly propagating pulse. As shown in Figure 3.9C, the magnitude of the released pulse decreases exponentially with increasing trapping time with a characteristic time constant of about 7 μs. Note that only a part of this decay is due to the hyperfine coherence decay. Other decay mechanisms include spreading of the stationary pulse as well as imperfect EIT. We anticipate that improvements in efficiency can likely be achieved, e.g., by initial optical pumping into a single atomic sublevel, using an atomic system with larger level spacing or sharper absorption lines of cold atom clouds.

3.4 Outlook

Finally, we outline possible avenues opened by this work. First, we note that our procedure is based on a passive medium and in the ideal limit is not accompanied by optical loss or gain hence avoiding the associated noise. We therefore anticipate that our method preserves the quantum states of light pulses. This is in contrast, e.g. to Bragg gratings based on gain modulation [55].

Second, although the present work demonstrates stationary light localization and storage in one dimension, it should be possible to controllably localize and guide stationary photonic pulses in three spatial dimensions by using control beams with properly designed wavefronts. An experimental study we conducted in this direction can be found in Appendix C.

Third, controlled conversion of propagating light into stationary light pulses opens interesting possibilities for enhanced non-linear optical processes by combining the present technique with the resonant enhancement of non-linear optics via EIT [43, 81, 48]. This combination may enable controlled interactions involving quantum few-photon fields [44, 62, 75, 73] analogous to those feasible in cavity QED [64]. Finally, extension of the present ideas to other systems might be possible using, for example, dynamic modulation of photonic bandgap materials.

Chapter 4

Cold atoms inside a hollow optical fiber

Laser-cooled atoms trapped inside a single-mode photonic waveguide result in a system with unique properties and many potential applications. The use of an optical dipole trap inside a hollow optical waveguide with the goal of guiding trapped cold atoms over macroscopic distances was first theoretically proposed in [72]. Due to the difficulty of guiding light inside low-refractive-index regions, the initial experimental demonstrations done with simple glass capillaries struggled with rapid attenuation of the trap beam coupled into the capillary. Additionally, speckle patterns forming as a result of multimode propagation of light in the capillary would create attractive spots on the capillary walls and cause significant atom losses. In these experiments, the best atom guiding was achieved with evanescent-light fields from blue-detuned laser light injected into the annular glass region of the capillary [68]. However, the nature of light propagation in the capillaries made it fundamentally impossible to attempt efficient nonlinear optical processes in these confined atomic ensembles.

In the last few years, two new experimental approaches to interaction between photons in a waveguide and cold atoms have been introduced. In the first approach, cold atoms are trapped close to a tapered optical nanofiber [79, 69], such that the evanescent field of the guided probe light interacts strongly with them. The second approach, described in this work, uses single-mode hollow-core photonic crystal fibers introduced in [25] and relies on the principles described in [72]. Cold atoms here are trapped by the field of a nearly Gaussian guided mode propagating in a single-mode optical waveguide, which can additionally guide the probe light in the same mode.

The procedures, which allow us to obtain an ensemble of cold atoms trapped inside a hollow single-mode waveguide, are described in this chapter.

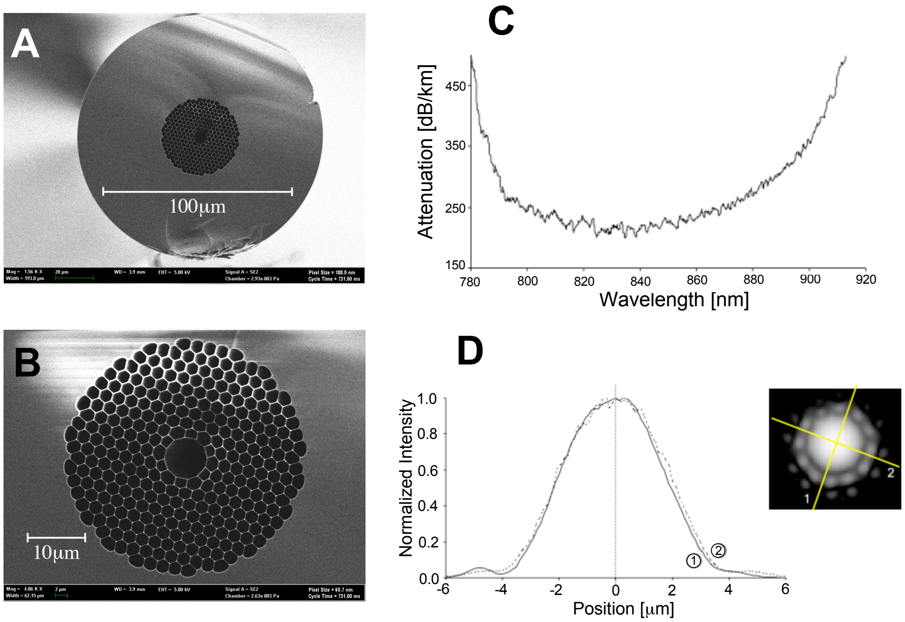

Figure 4.1: Hollow core photonic crystal fiber, model *HC-800-02*, from Blaze Photonics (A) Scanning electron microscope (SEM) image of a cleaved fiber. (B) Detail of the photonic crystal region with the hollow core in the center. Manufacturer's specifications for: (C) losses of guided mode propagating in the fiber as a function of wavelength and (D) near field intensity distribution of the guided mode.

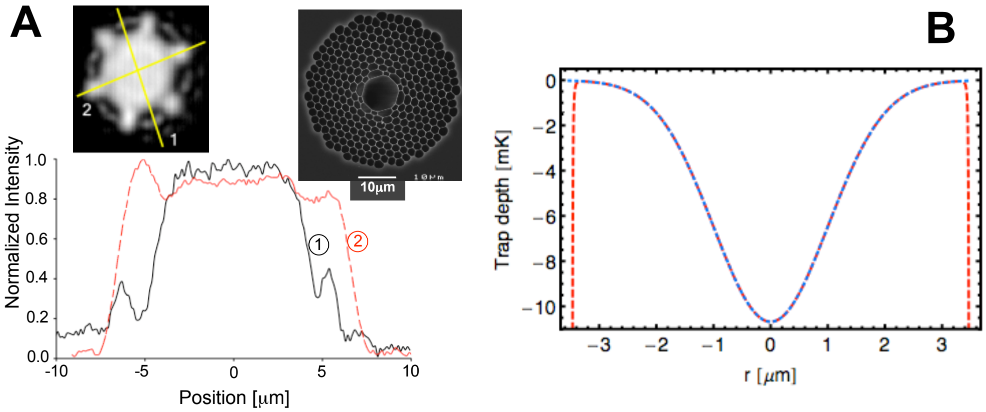

Figure 4.2: (A) Hollow core fiber, model *HC-800-01* from Blaze Photonics: Near field intensity distribution of the guided mode and SEM image of the photonic crystal region (images taken from the manufacturer's spec sheets). (B) Dipole trap potential inside the fiber for 25mW of 802nm trap light (blue curve) assuming a Gaussian beam with $w_0 = 2.0\ \mu m$ guided inside the *HC-800-02* model of the hollow-core fiber. The red dashed curve includes the wall attraction potential as a C_4/r^4_{wall} term with the nominal value of $C_4 = 8.2 \times 10^{-56} Jm^4$ taken from [95, 58]

.

4.1 Preliminary considerations

4.1.1 Fiber selection

At the time this experiment was being started, we were able to obtain two different models of hollow-core photonic crystal fiber (PCF) whose range of guided wavelengths included those corresponding to D_1 and D_2 transitions in rubidium at 795 nm and 780 nm (Fig. 4.1 and 4.2A). We decided to use model *HC-800-02* (Fig. 4.1) for the experiment since the field distribution of the guided mode here was closer to a Gaussian profile. The concern in the case of *HC-800-01* (Fig. 4.2A) was that, because of the flatness of the guided mode distribution, there might not be enough intensity gradient within the hollow core to keep the atoms from interacting with the wall. While the results of [87] suggest that this probably would not have been a problem, the additional advantage of *HC-800-02* is that it has a smaller mode field diameter than *HC-800-01*, which results in higher probability of interaction between a single photon and a single atom.

Lastly, our measurements of the expansion of the guided mode of the *HC-800-02* in the far field showed that this mode is well approximated by a Gaussian beam with minimal waist inside the fiber of $w_0 = 1.9 \pm 0.2\,\mu$m.

4.1.2 Wall attraction and vacuum inside the fiber

During the preliminary "why this may not work" discussions, two issues arose that could have made atom trapping inside the fiber impossible.

Due to the small size of the hollow core, the possibility that attractive forces from the core wall would cancel the dipole trap potential had to be considered. A brief literature search [95, 58] and a quick approximate calculation revealed that atom-wall attractive forces become dominant only for distances less than a fraction of a micrometer (Fig. 4.2A). Thus for our fiber with a 7 μm diameter core, this should not significantly affect the shape or depth of the dipole trap potential.

The second issue concerned the amount of room-temperature background gas inside the fiber. While achieving pressures of 10^{-9} torr or less within the general volume of the vacuum chamber is a relatively straight-forward process, the small diameter of the fiber core and the associated pumping speeds could lead to an unacceptable lower bound on the pressure achievable inside the fiber that would severely limit the lifetime of the trapped atoms. A simple back-of-the-envelope calculation based on the expansion of a one dimensional gas cloud at room temperature predicts that the pressure inside the fiber would reach 10^{-6} torr in about a day, while getting down to 10^{-8} torr would take a little more than a month. Unfortunately, this model neglects possible outgasing from the fiber walls, which could make the final pressure predictions less optimistic. Cooling the fiber to liquid-nitrogen or even liquid-helium temperatures [47] would resolve the problem by turning the inner surface of the hollow core into a sorption pump, but it would also add another layer of technical complexity to the system. We finally decided not to worry about the problem using the following reasoning. First, given that the fiber is manufactured by pulling a bunch of semi-melted glass capillaries, the inner wall of the fiber core is most likely very clean and thus the amount of outgasing should be very small. Second, even if the vacuum in the middle of the fiber is not very good, it will be much better near the fiber tip and – to access the benefits of the system – trapping the atoms in that region would be sufficient. Ultimately, our experimental observations, such as the one in Fig. 4.7B, show that the atoms' lifetime inside the fiber can reach tens of milliseconds, which suffices for most of our needs.

4.1.3 Optical depth inside the fiber

The optical depth (OD) of a medium describes how much an on-resonant light beam passing through this medium is attenuated:

$$P_{out} = P_{in} e^{-\mathrm{OD}} \tag{4.1}$$

Here P_{in} and P_{out} denote the power in the beam before and after passing through the medium. In most experiments, the transverse dimension of the optical medium is much larger than the diameter of the light beam, which means that the atomic density over the illuminated area is assumed to be uniform. In this case, the OD of the atomic ensemble can be easily connected to the number of atoms N_{hom} interacting with the light beam resonant with atomic transition of scattering cross-section σ_o:

$$\mathrm{OD}_{\mathrm{hom}} \approx n\sigma_o L = \frac{N_{hom}\sigma_o}{A_o}. \tag{4.2}$$

Here, n is the atomic density, L is the length of the medium, $A_o = \pi w_o^2$ is the nominal area of the incident light beam, and the "≈" sign can be replaced by "=" for an idealized beam with uniform intensity distribution and radius w_o.

In our experiment, the atoms are confined within the optical trap created by the guided light inside the fiber. Consequently, the radial extent of the atomic cloud is comparable or smaller than the beam area of the single-mode probe light beam propagating through the fiber. To get a more accurate expression for optical depth as a function of atom number in the ensemble, we have to make a correction of the scattering cross-section σ_o based on the atoms' radial distribution in the beam. This correction can be derived from equation (2.4) in section 2.1 – an atom sitting at the edge of a beam sees a smaller electric field and therefore appears to have a smaller scattering cross-section than an atom on the beam's axis. Assuming a Gaussian beam with waist w_o and an axially symmetric atomic density $n(r, z)$, the expression for optical depth on resonance will be

$$\mathrm{OD}_{\mathrm{fiber}} = \frac{2}{\pi w_o^2} \int_{L_{cloud}} 2\pi \int_0^{r_{core}} n(z,r)\sigma_o e^{-\frac{2r}{w_o^2}} r dr dz \tag{4.3}$$

where the normalization factor $\frac{2}{\pi w_o^2}$ results from the Gaussian beam intensity distribution and we took $\sigma(r) = \sigma_o\, e^{-\frac{2r}{w_o^2}}$ as the position-dependent scattering cros-section in a Gaussian beam. In general, (4.3) can be simplified into a form similar to (4.2)

$$\mathrm{OD}_{\mathrm{fiber}} = \eta\, N_{at}\, \frac{\sigma_o}{A_o} \tag{4.4}$$

with η given by the radial distribution of atoms in the fiber-confined cloud. The highest value of η corresponds to all atoms being localized on the axis of the fiber, in which case $\eta = 2$. For illustration, two additional noteworthy cases of cloud distribution are $n(r) \sim e^{-\frac{2r}{w_o^2}}$, in which case $\eta = 1$, and $n(r) \sim \frac{1}{A_o}$ (uniform distribution of the N_{at} atoms over the nominal area of the beam) in which case $\eta \approx 0.86$. With the measured beam waist of guided light inside the fiber being $w_0 = 1.9 \pm 0.2\,\mu$m, we can predict that ~ 100 atoms inside the fiber can create an optically dense medium ($OD = 1$).

Note that the optical depth for a given number of atoms inside the fiber does not depend upon the length of the atomic cloud. Additionally, our treatment leading to (4.3) assumes a sufficiently dilute cloud of atoms, so that that effects altering

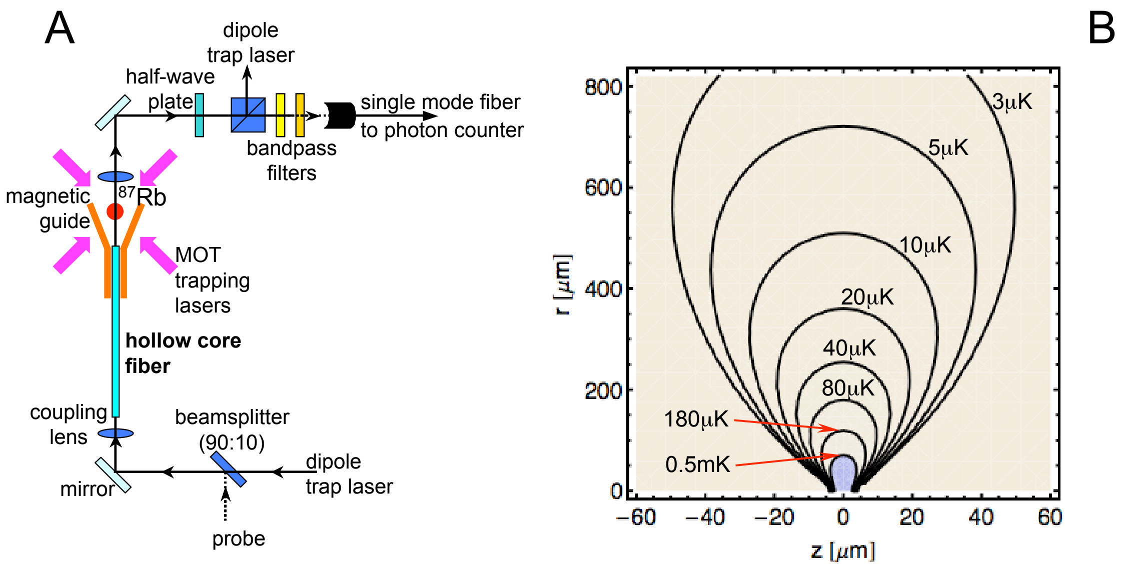

Figure 4.3: (A) The schematics of the experiment. (B) Contour plot of the dipole trap potential above the fiber tip resulting from the diverging beam coming from the fiber tip. The contour labels correspond to a 10 mK deep trap inside the fiber resulting from ∼25 mW of 802 nm trap light inside the fiber.

the guiding properties of the fiber, such as lensing, can be neglected. Finally, the off-resonant OD for the system, in the limit of a weak probe, can be written as

$$\mathrm{OD}(\delta) = \frac{\mathrm{OD}_{\mathrm{fiber}}}{1 + 4\frac{\delta^2}{\Gamma^2}}. \tag{4.5}$$

4.2 From a room-temperature vapor in free space to cold atoms inside the fiber

Our apparatus (Fig. 4.3A) makes use of a 3 cm-long piece of single-mode hollow-core PCF vertically mounted inside an ultra-high vacuum chamber. Inside the fiber, the atoms are radially confined by a red-detuned dipole trap formed by a single beam guided by the fiber itself. The small diameter of the guided mode allows for strong transverse confinement (trapping frequencies $\omega_t/2\pi \sim 50 - 100\,\mathrm{kHz}$) and deep trapping potential ($\sim 10\,\mathrm{mK}$) at guiding light intensities of a few milliwatts. Since the atoms are pulled toward high light intensity, the diverging beam coming from the fiber tip creates a potential gradient outside the fiber that attracts cold atoms from the vicinity of the fiber end into the fiber core (Fig. 4.3B). During the experiment, a laser-cooled cloud of ^{87}Rb atoms is collected into a magneto-optical trap, transferred

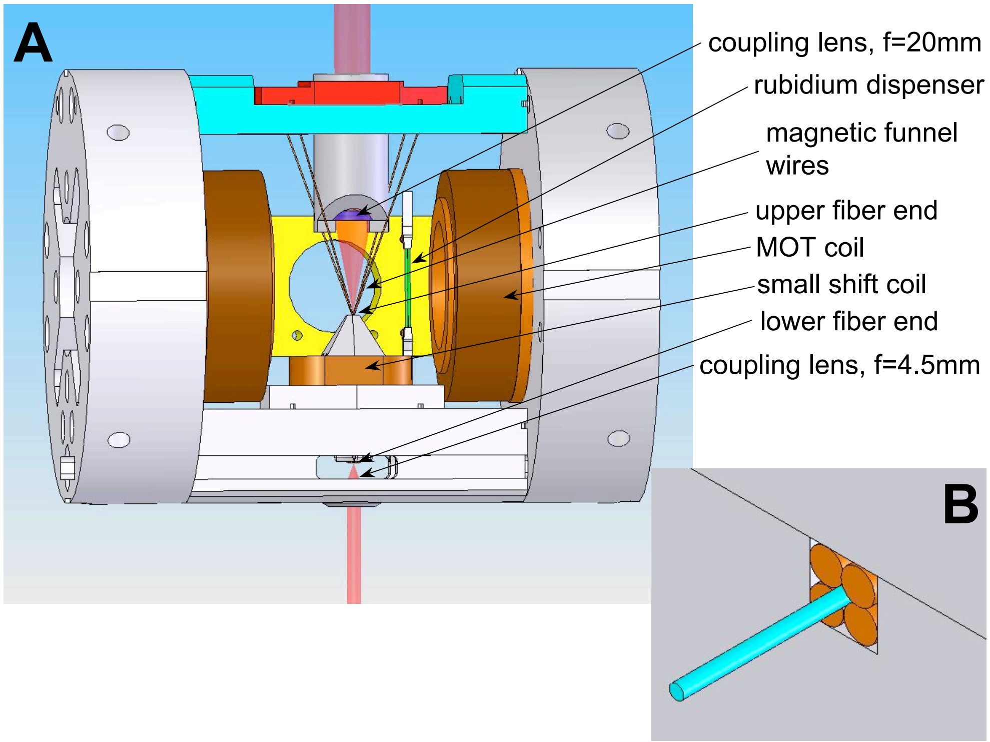

Figure 4.4: (A) Fiber assembly. (B) The anchoring of the fiber inside the mount.

into the vicinity of the upper tip of the PCF, and loaded into a red-detuned dipole trap guided inside the hollow-core fiber.

To probe the atoms in the fiber, we monitor the transmission of two very low power ($\sim 1\,\mathrm{pW}$) probe beams with single-photon counters. One of the beams is coupled into the single mode PCF from the bottom, as shown in Fig. 4.3A). After this probe emerges from the upper fiber tip, it is collimated by the top coupling lens and then passed through a series of optical filters that separate the probe photons from other light beams coupled into the fiber during the experiments. Finally, the probe is coupled into a single-mode fiber connected into a photon counter. This last step provides spatial filtering that ensures that only photons propagating in the guided mode of the PCF reach the photon counter. A second probe beam (not shown in the schematics) is coupled into the fiber from the top, is collimated by the bottom coupling lens after it exits the lower fiber tip, and passes through a set of frequency and spatial filtering stages identical to those the bottom-coupled probe passes through before reaching a single-photon counter.

4.2.1 Fiber mounting structure

The hollow-core fiber (Fig. 4.1) used in the experiment, *HC-800-02*, has a $7\,\mu$m diameter hollow core, and guides light with wavelengths between 780 nm and 900 nm. The fiber is the centerpiece of a custom-made, ultra-high vacuum compatible assembly mount that includes coupling and imaging optics, as well as magnetic field generating structures (Fig. 4.4A).

The fiber piece is held between four Kapton coated copper wires, which run parallel to the fiber and fan out upwards in an upside-down pyramid configuration above the fiber (shown in Fig. 4.4 and 4.5). The diameter of these wires was chosen such that when the wires are packed in a tightly fitting rectangular slit (Fig. 4.4B), the fiber snugly fits into the space between them. Besides anchoring the fiber, the wires gently compress it, which makes the fiber birefringent in a well defined manner. This is a fairly important feature, since the polarization properties of an uncompressed PCF tend to drift. Finally, when current of the appropriate direction is applied to them, the wires can act as a magnetic guide that allows us to focus the atomic cloud as it is being transferred towards the fiber tip.

In addition to these wires, a parallel pair of coils (main axis horizontal, perpendicular to the fiber) is integrated into the fiber mount. Their symmetry center is located slightly above the fiber tip to create a magnetic quadrupole field for the initial stages of the experiment.

Besides the current-carrying structures, several optical elements are integrated into the fiber mount as well. Two short focal-length lenses allow coupling of light into the guided mode of the fiber ($f \approx 20$ mm for the lens above the fiber, $f = 4.5$ mm for the lens below). These lenses allow us to couple light into the single mode of the PCF with efficiency up to $\sim 40\%$ for light with wavelength 795 nm or longer and up to $\sim 25\%$ for light in the 780-785 nm range. We believe this less than ideal coupling is caused by imperfections in the cleaving of this particular fiber piece, as we have been since able to produce fiber pieces into which we can couple up to 70% of the incoming light. Additionally, a single lens with $f \approx 25$ mm (visible in Fig. D.6 B and C) is used for magnified absorption imaging of the atoms near the fiber entrance in the area of the magnetic guide.

4.2.2 Loading procedure

The starting point of our fiber loading procedure is a standard six-beam magneto-optical trap (MOT) located approximately 6 mm above the upper tip of the fiber piece (Fig. 4.5A). The required light fields are provided by three crossed retro-reflected beams with one-inch diameter, while the magnetic field is realized by two circular coils inside the vacuum chamber operated in an anti-Helmholtz configuration. During a ~ 1 s loading phase we collect about 10^7 ^{87}Rb atoms at a temperature of $\sim 100\,\mu$K in the MOT from the room-temperature rubidium vapor produced inside the vacuum

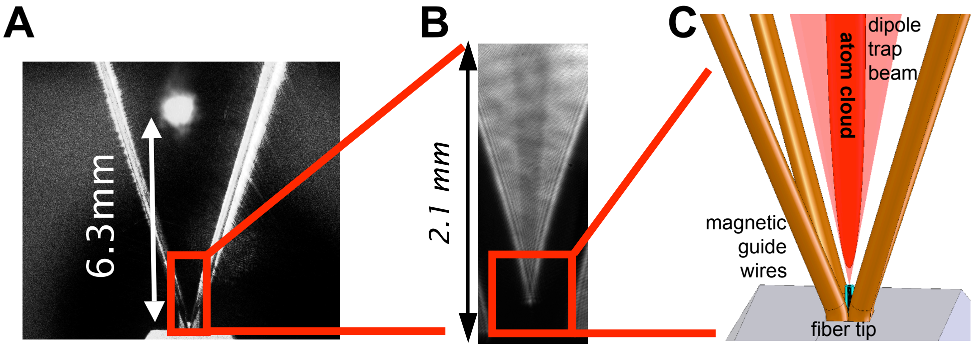

Figure 4.5: The loading procedure: (A) Atoms collected in a MOT above the fiber. (B) Absorbtion image of the atoms in the magnetic funnel area above the fiber. (C) The atoms are transferred into a red detuned dipole trap inside the fiber.

chamber by a heated dispenser. Following this step, the magnetic fields are ramped up over a period of 40 ms to compress the cloud, the frequency of the trapping beams is moved from the initial 15 MHz off-resonance to 50-60 MHz, and their power is reduced by a factor of ~ 4 . Finally, the magnetic fields are shut off, and the atomic cloud is allowed to slowly expand for 1 ms[1] in the optical molasses of the intersecting beams as it undergoes polarization gradient cooling. Following this last cooling step, which lowers the cloud temperature to $\sim 40\ \mu$K, we transfer the atoms downwards into the vicinity of the fiber tip using one of the three methods described at the end of this chapter (Fig. 4.5B).

During the transfer stage, which takes $\sim$ 40 ms, the fiber-guided dipole trap is turned on, so that when the atoms start approaching the fiber face, they are captured by the expanding beam of the dipole trap and pulled into the hollow core of the PCF(Fig. 4.5C). Initially, we operated the dipole trap slightly red-detuned of the rubidium D_2 line, i.e. at $782-785\,\text{nm}$ and used powers of $5-8\,\text{mW}$, which is sufficient to provide a trap depth up to $\sim 10\,\text{mK}$ inside the fiber. In the last year, we switched to a 25 mW dipole trap operating at 802 nm. This allowed us to retain a trap depth of $\sim 10\,\text{mK}$ inside the fiber, but the larger detuning from the rubidium lines made optical filtering easier and reduced scattering-induced heating. In most of the experiments, unless stated otherwise, the dipole trap is coupled into the lower end of the fiber and propagates upwards.

After the end of the transfer stage, we usually wait $\sim 5\,\text{ms}$ before we perform the experiments, which allows the captured atoms to move into the fiber. Additionally,

---

[1] The data presented in Chapter 5 were obtained with the atomic cloud expanding for 10 ms in this step. However, 1 ms is sufficient for the polarization gradient cooling and the shorter expansion time results in more atoms loading into the fiber.

if magnetic guiding was used in the transfer process, this step gives the transient magnetic fields time to vanish. Typically, the duration of the actual experiments ranges from 100 to 400 μs, during which we modulate the optical trap, as discussed below. The whole cooling, trapping, and data collection cycle is repeated every 1.5 s. For the probe transmission scans such as those shown in Fig. 4.6A, each data point corresponds to a single run of the experiment (or multiple runs in the case of data averaging). Between these runs, the frequency of the probe laser is changed, and a new atomic sample is prepared in the fiber. Compared to doing a full frequency scan during one experimental cycle, this approach allows the probe at each frequency to interact with a nearly identical atomic cloud.

Incidentally, we can easily reduce the number of atoms loaded into the fiber by either by collecting fewer atoms into the MOT (e.g. by decreasing the loading time) or by lowering the power in the fiber guided dipole trap.

4.3 Atoms inside the fiber

4.3.1 Modulated dipole trap

Absorption profiles associated with atomic resonance lines are signature of interaction between atoms and light guided through the PCF. If the atoms are probed inside the dipole trap, we observe a unique profile shown in Fig. 4.6A. The dipole trap introduces a power-dependent, radially varying AC-Stark shift [39], which results in broadening and a frequency shift of the absorption profile (blue data points in Fig. 4.6A). Comparison with the calculated profile based on the dipole trap parameters suggests that the atoms are loaded inside the fiber. For the experiments described below, we avoid broadening of the atomic transition by synchronous square-wave modulation of the dipole trap and the probe beam with opposite phase (Fig. 4.6B) at a rate much higher than the trapping frequency (Fig. 4.6C). When using this technique and scanning the probe laser over a particular hyperfine transition, we typically observe a narrowed absorption profile as shown in figure 4.6A (black data points). The shape of this resonance is completely determined by the natural line profile of the transition

$$T_{nat} = \exp\left(-\frac{\mathrm{OD}}{1+4\frac{\delta_p^2}{\Gamma_e^2}}\right), \tag{4.6}$$

where Γ_e is the lifetime of the excited atomic state, $\delta_p = \omega_p - \omega_0$ is the detuning of the probe laser from resonance, and OD is the optical depth as defined in (4.4).

4.3.2 Are the atoms really inside?

Unfortunately, the construction of the fiber mount does not allow us to obtain an image of the atoms inside the fiber, which would provide direct proof of successful

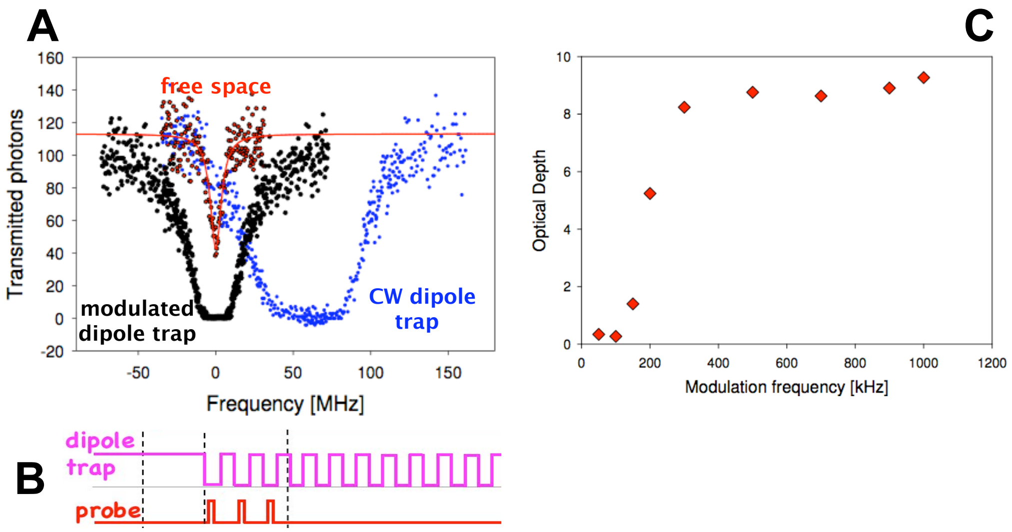

Figure 4.6: Atoms inside the fiber: (A) Transmission of the fiber as a function of probe frequency with constant dipole trap (broad blue data curve centered at ∼ 60 MHz) and with modulated dipole trap (narrower black data curve centered at 0 MHz). For comparison, the red curve shows the absorption profile as seen through the fiber when the atomic cloud is still in the MOT area. (B) Modulation scheme for probe and dipole trap: The probe is broken into ∼ 100 short pulses that interact with the atoms when the dipole trap is off. (C) Detected optical depth of the atomic cloud inside the fiber as a function of the dipole trap modulation frequency.

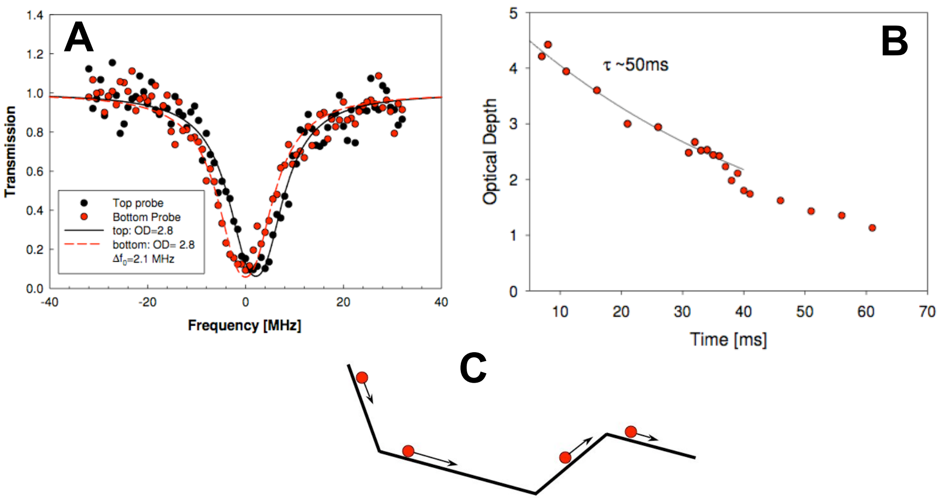

Figure 4.7: Atoms inside the fiber: (A) Doppler shift of the falling atom cloud observed by using two probes propagating through the fiber in opposite directions. (B) Lifetime of the atoms inside the fiber (C) A sketch of the potential experienced by the atoms as the load into the fiber-guided dipole trap.

loading. Detection of atoms exiting at the lower end of the fiber would be direct proof as well. This would also be a non-trivial task which basically comes down to single atom detection in free space. While we did build some infrastructure into the fiber assembly for this purpose, we have not yet attempted this. Instead, we rely on indirect signatures of the atoms loading into the fiber core.

One of these signatures is the shape of the atomic resonance absorption profile – described in 4.3.1 – altered by the AC-Stark shift induced by the fiber guided dipole trap. One could argue that, based on this profile only, it cannot be fully resolved whether the atoms are trapped right above the fiber face (within the Rayleigh length of the diverging beam) or actually inside the fiber core. An additional indirect signature can be obtained by deploying two probes propagating in opposite directions through the fiber. The observed absorption profiles show a distinct difference between the frequency centers of the two profiles (Fig. 4.7A) after the atoms are loaded into the dipole trap. This frequency difference is the result of a Doppler shift caused by motion of the atomic cloud with respect to the two beams. In this case, the observed shift corresponds to the cloud moving downwards with velocity 0.82 mm/ms. This shift can be observed for times exceeding 10 ms, which is evidence of the atoms moving inside the fiber core.

4.3.3 Lifetime of atoms inside the fiber

Once inside the fiber, the atoms are confined by the red detuned dipole trap only in the radial direction, while in the vertical direction they experience a free fall up to when they reach the lower end of the fiber. An example of the measured optical depth of the falling atomic cloud as a function of time is plotted in figure 4.7B. Here, the zero on the time axis corresponds to the instant when the optical depth in the fiber is the largest. In this measurement, each point on the graph corresponds to a newly loaded atomic cloud for which the dipole trap was kept on continuously until the point in time when the OD was measured using the modulation described in 4.3.1. The ‘kink’ in the data near 40 ms corresponds to the free-falling atoms reaching the lower end of the fiber. Up to this point the atoms decay out of the dipole trap exponentially with a time constant of $\sim$ 40 ms. We explain the data after the ‘kink’ as part of the atomic cloud leaving the fiber and part of the cloud reflecting back from the potential change associated with the dipole-trap beam being coupled into the lower end of the fiber. To verify this, we are currently working on detecting the atoms exiting at the lower fiber end.

As the atoms move inside the fiber, they are lost from the dipole trap mostly through two mechanisms. The first and more obvious one is caused by collisions with the background gas present due to imperfect vacuum within the PCF core. The second mechanism originates from the presence of higher-order modes propagating through the PCF. These modes interfere with the fundamental mode and create a longitudinal variation of the dipole trap potential, which is otherwise smooth in the axial direction. This corrugation allows the longitudinal velocity of the atoms to couple into the radial motion of the atoms. The longitudinal velocity of the atoms can be quite large, since they gain kinetic energy from falling into the dipole trap potential (Fig. 4.7C). This coupling heats the atoms in the transverse direction and ejects them from the dipole trap. As a result, we have observed a decay constant of the atoms inside the fiber ranging from 10 ms up to 100 ms depending on the velocity with which the atomic cloud moves inside the fiber.

These higher-order modes can be present in all single-mode fibers as their excitation during beam coupling from free space into fiber is virtually inevitable. However, these modes propagate with losses significantly larger than those of the fundamental mode and generally die away when propagating through fiber pieces longer than $\sim 1\,\mathrm{m}$. For a short piece of fiber, like the one used in the experiment, the losses of the higher order modes will not be sufficient to suppress their presence. Unfortunately, even small amount of power propagating in a higher mode will lead to a significant modulation of the original potential, since this modulation is the result of interference between the dominant (Gaussian-like) and the higher-order mode.

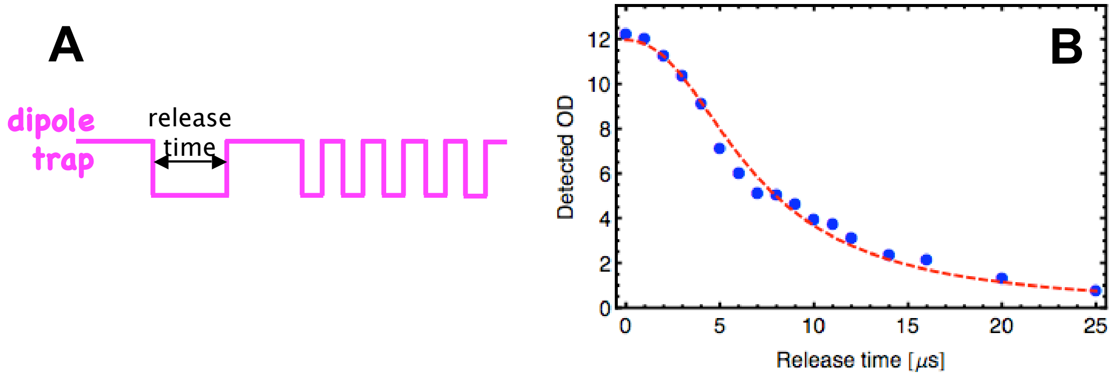

Figure 4.8: Temperature estimate from a TOF measurement: (A) The time sequence diagram: After the atoms are released from the trap and then recaptured, the trap is modulated for the OD measurement. (B) Optical depth of the recaptured cloud as a function of the release time. The dashed red line represents a fit based on the Gaussian cloud expansion model.

4.3.4 Length of the atomic cloud inside the fiber

In general, during the loading procedures the atoms arrive at the upper tip of the fiber with velocities of ~ 0.35 m/s over time intervals ~ 10 ms. Once they fall into the dipole trap potential, their velocity will reach up to ~ 1.4 m/s, depending on the depth of the dipole trap inside the fiber. Consequently, during the ~ 10 ms when the atoms are entering the fiber, the front edge of the atomic cloud is moving at ~ 1.4 m/s, while its rear edge is moving at ~ 0.35 m/s. Based on this, we estimate the length of the atomic cloud inside the fiber to be ~ 1 cm.

4.3.5 Temperature of the fiber confined atomic cloud

The tight confinement of the fiber-guided dipole trap will increase the temperature of the atoms compared to free space. To estimate the temperature of the atoms inside the fiber, we perform a time of flight (TOF) measurement, which will also allow us to estimate the radial distribution of atoms in the fiber. We first shut off the dipole trap and let the cloud expand, then turn the trap on again to recapture atoms that have not collided with the wall (Fig. 4.8A). After this, we modulate the dipole trap and measure the optical depth of the recaptured atoms. In a simple model that assumes a Gaussian distribution of the atoms in the radial direction $n(r) \sim e^{-(r/r_o)^2}$, the optical depth of the recaptured cloud as a function of the release time τ_r can be written as

$$\mathrm{OD}(\tau_r) \approx \mathrm{OD}_0 \left(1 - \exp\left[\frac{-\left(\frac{R_{core}}{r_o}\right)^2}{1 + \left(\frac{v_o}{r_o}\right)^2 \tau_r^2}\right]\right) \tag{4.7}$$

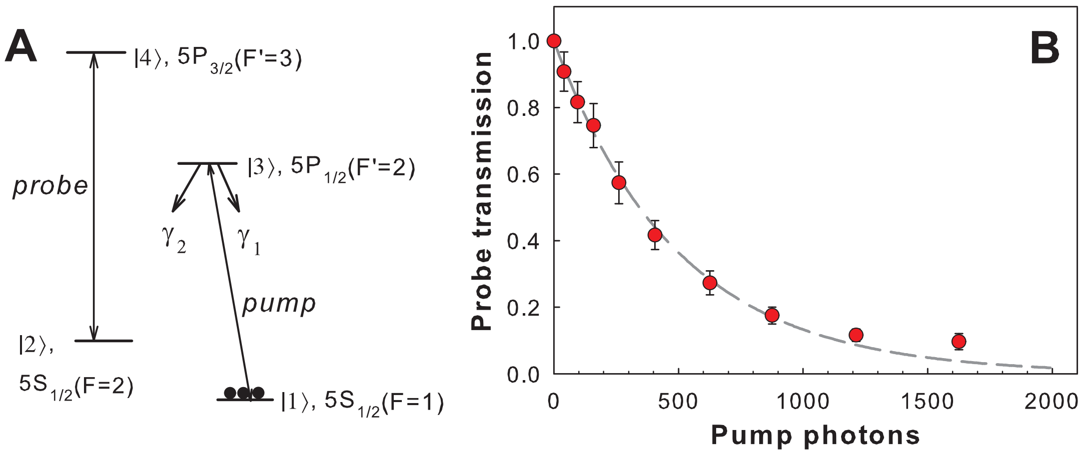

Figure 4.9: Nonlinear saturation based on incoherent few-photon controlled population transfer: (A) The atomic level scheme and the corresponding hyperfine states (for this level choice $\gamma_2 = \gamma_1$) (B) Transmission of the resonant probe through the fiber as a function of the number of pump photons

where $v_o = \sqrt{\frac{2kT_r}{m_{Rb}}}$ and R_{core} is the radius of the PCF core. We can extract the temperature of the cloud by fitting (4.7) to a set of release and recapture data with $A = \left(\frac{R_{core}}{r_o}\right)^2$ and $B = \left(\frac{v_o}{r_o}\right)^2$ as the fit parameters.

An example of such a measurement can be seen in figure Fig. 4.7B. Fitting (4.7) to this data set yields $T_r \approx 1.6$ mK and $r_o \approx 2.2\ \mu m$.

4.3.6 Nonlinear saturation based on incoherent few-photon controlled population transfer: Counting atoms inside the fiber

In the following experiment we would like to demonstrate nonlinear saturation based on incoherent population transfer in our mesoscopic atomic ensemble. Besides serving as an illustration of the strong interaction between photons and atoms in our system, this experiment allows us to calibrate the average optical depth of a single atom in the PCF confined ensemble.

Here, the transmission of the probe beam, which is coupled to a cycling atomic transition $|2\rangle \rightarrow |4\rangle$, is controlled via an additional pump beam transferring atoms from an auxiliary state $|1\rangle$ into state $|2\rangle$ (Fig. 4.9A). Initially, the state $|2\rangle$ is not populated, and the system is transparent for the probe beam. The incident pump beam, resonant with the $|1\rangle \rightarrow |3\rangle$ transition, is fully absorbed by the optically dense atom cloud, exciting the atoms to the $|3\rangle$ state. From there, the atoms can decay into the $|2\rangle$ state, where they then affect the propagation of the probe beam.

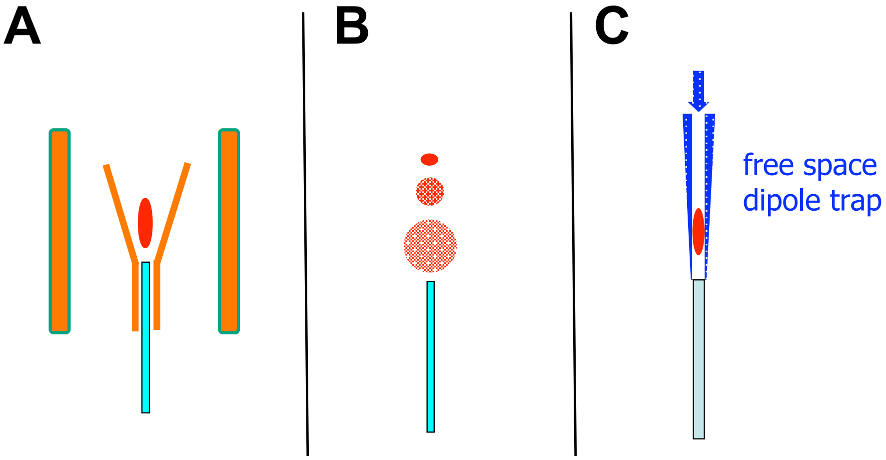

Figure 4.10: Schematics of the cloud transfer procedures: (A) Trapping and guiding in a magnetic funnel. (B) Free drop. (C) Free drop in a a hollow beam optical dipole trap.

In Fig. 4.9B, we present the observed transmission of the probe beam as a function of the total number of pump photons sent into the medium. We observe an exponential reduction of the transmission with increasing number of pump photons. In particular, we achieve a e^{-1} reduction of the initial probe transmission for a total number of only 400 pump photons. The efficiency of the incoherent population transfer is limited mainly by the branching ratio of the decay from the excited state $|3\rangle$ to the two ground states $|1\rangle$ and $|2\rangle$. In our case, the probability to decay to the $|2\rangle$ is $p = 1/2$. Hence ~ 200 atoms are transferred into the $|2\rangle$ state, which is sufficient to cause the observed significant absorption of the probe beam. This also means that for this particular atomic transition, 200 atoms inside the fiber core create a medium with OD = 1.

4.4 MOT to dipole trap transfer procedures

We have used three different procedures for transferring the laser-cooled atomic cloud from the MOT site to within the capture range of the fiber-coupled dipole trap (Fig. 4.10). The first procedure consists of letting the atomic cloud fall freely towards the fiber tip and it allowed us to load ~ 5000 atoms into the fiber core. The second transfer procedure was based on atom guiding in a magnetic funnel and resulted in loading of up to ~ 10000 atoms. Finally, the third procedure combines free fall with guiding in a hollow-beam optical dipole trap and using it we observed up to ~ 30000 atoms inside the hollow core of the PCF. While we are still working on a

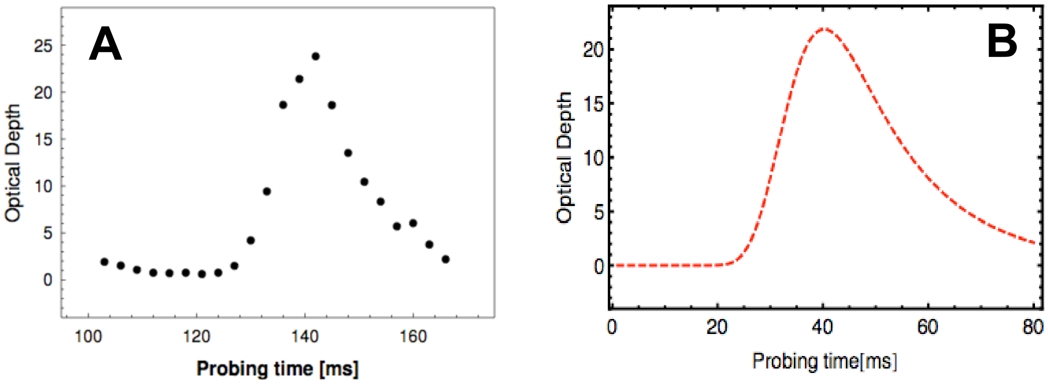

Figure 4.11: Dynamics of fiber loading from a free falling atomic cloud. (A) Experimental results with the MOT beams shut off at $t_0 = 100$ ms. (B) Numerical simulation the simple loading model based on (4.8) and (4.10) with $R_{capt} = 100\ \mu m$ and while the rest of the parameters corresponding roughly to the experimental conditions in our system: $\tau_d = 15$ ms, $r_o = 0.34$ mm, $v_o = 8.3\ cm/s$, $N_o = 7 \times 10^6$, and $y_o = 6.3$ mm.

more quantitative explanation of the relationship between the transfer procedures and the fiber loading efficiency, here we will discuss the implementation and qualitative descriptions of these three procedures.

4.4.1 Free fall

While this procedure loads the smallest number of atoms, it works surprisingly well given how easy it is to implement. Ironically, this was not the first method that we tried, and in fact it took us quite some time to realize that it could be used. Besides the simplicity of its implementation, an additional advantage includes the option to probe the progress of the atom loading during the transfer procedure.

The procedure consists of shutting off the MOT beams after the optical molasses stage and letting gravity run its course. The atoms will load into the dipole trap ~ 36 ms from the time the beams were turned of, which is the time it takes them to travel the 6.3 mm distance from the MOT site to the fiber face by free fall. An example of fiber loading from a free falling cloud can be seen in Fig. 4.11 A. After the MOT beams are turned off at $t_0 = 100$ ms and the atoms start falling, we can see OD ~ 3 resulting from the interaction between the atomic cloud and the probe beam propagating in free space after it exits the upper fiber tip. This initial OD then decays away as the atomic cloud expands and becomes less dense. The observed OD remains zero until about $t_1 \approx 130$ ms when the first atoms start arriving into the fiber tip vicinity where they get pulled into the dipole trap. As more atoms arrive and get loaded into the fiber, the OD rapidly increases until it reaches its maximum at $t_2 \approx 142$ ms. After this point the OD decreases due to decay mechanisms.

It should be noted that although this procedure generally loads atoms fairly robustly, it is somewhat sensitive to the power balance in the beams of the optical molasses. When there is an imbalance, the beams will impart a transverse drift velocity on the atomic cloud causing it to miss the capture area of the fiber-coupled dipole trap, which results in poor loading.

Modeling the loading dynamics

The dynamics of a dipole trap loading process can be generally described by a differential equation discussed in [57], where for the number of atoms inside the trap $N(t)$ we can write:

$$\frac{dN}{dt} = \left(\frac{dN}{dt}\right)_{inc} + \left(\frac{dN}{dt}\right)_{loss} = R_{inc}(t) - \frac{N}{\tau_d}. \tag{4.8}$$

In our case, $R_{inc}(t) = \left(\frac{dN}{dt}\right)_{inc}$ is the rate at which atoms load into the fiber, $\left(\frac{dN}{dt}\right)_{loss} = -\frac{N}{\tau_d}$ is the loss rate in which we assumed simple exponential decay and neglected density-dependent losses, and we can use the conversion of 200 atoms per unity OD from 4.3.6 to translate between optical depth and atom number.

In a simple way, we can model the dynamics of the dipole trap loading as atoms hitting a horizontal circular target with radius R_{capt} attached concentrically to the upper fiber tip. In this picture, the overall number of atoms that make it into the fiber core N_{fiber} is roughly equal to the number atoms present in the overlap between an infinite cylinder with radius R_{capt} and the atomic cloud at time $t_{drop} \approx 36$ ms, the average time it takes the atoms to reach the fiber face by free fall. Taking into account the expansion of the cloud (see Appendix E), we get

$$N_{fiber} \approx N_o \left(1 - Exp\left[\frac{-R_{capt}^2}{r_o^2 + v_o^2 t_{drop}^2}\right]\right) \tag{4.9}$$

where N_o is the number of atoms in the original cloud, r_o is the radius of the cloud at time $t_o = 0$, and $v_o = \sqrt{\frac{2kT_o}{mRb}}$ is the expansion velocity given by the cloud's initial temperature T_o. For our experimental conditions $N_o \sim 6 \times 10^6$, $T_o \sim 40\ \mu$K, $r_o \sim 0.35$ mm, the loading of ~ 5000 atoms into the fiber fiber core as observed in Fig. 4.11 A implies the capture radius of the dipole trap to be $R_{capt} \approx 100\ \mu m$. This is a highly counterintuitive result, especially when we compare the temperature of the cloud, which is $\sim 40\ \mu$K with the contours of the diverging dipole trap beam in Fig. 4.3B. We will return to this point later.

Going back to (4.8), we can describe the loading rate $R_{inc}(t)$ as a rate at which atoms in the free-falling cloud land at the previously described target with radius

R_{capt}. This allows us to express $R_{inc}(t)$ as

$$R_{inc}(t) \approx \frac{N_o\left(\frac{1}{2}gt+\frac{y_o}{t}\right)}{\sqrt{\pi}\sqrt{r_o^2+v_o^2t^2}}\left(1-Exp\left[\frac{-R_{capt}^2}{r_o^2+v_o^2t^2}\right]\right)Exp\left[\frac{-\left(\frac{1}{2}gt^2-y_o\right)^2}{r_o^2+v_o^2t^2}\right]. \tag{4.10}$$

The numerical solution of (4.8) then yields the curve in figure 4.11B, which has a rough qualitative agreement with the experimental results. Our loading model can be further improved by taking into account the dependence of R_{capt} on the vertical velocity of the approaching atoms.

Atom cooling by expansion

The counterintuitively large capture radius of the fiber-coupled dipole trap can be easily explained when one considers the position-dependent temperature[2] in the expanding atomic cloud. At time t_o, right after the optical molasses beams are turned on, both the cloud density and the velocity of the atoms have mutually independent Gaussian distributions. In other words, the velocity of a particular atom at this time is independent of its position in the cloud. However, after the cloud expands in free space, as it is doing during the free fall, this will no longer be true. In particular, one notices that the velocity distribution for atoms in the center of the cloud becomes narrower (Fig. 4.12B), which is equivalent to the atoms being colder. This has a rather simple explanation in the form that the fast atoms from the initial Maxwell-Boltzmann distribution fly away leaving the slow atoms behind. This can be seen in Fig. 4.12C that plots the transverse kinetic energy of atoms in the center. Combining this with Fig. 4.12B one sees that after t_{drop} there will be an area with radius comparable to R_{capt} with atoms which are about an order of magnitude colder than the initial cloud. The trade-off for this "cooling" is, of course, the decreasing density of the atomic cloud with time (Fig. 4.12D).

4.4.2 Magnetic funnel guiding

In this procedure, after the initial cooling stages in the MOT and optical molasses are completed, the atoms are optically pumped into the $|F=2, m_F=2\rangle$ state and then transferred into a magnetic quadrupole trap formed by the same coils which provide the MOT field. This trap is then adiabatically shifted towards the fiber tip by adding a vertically-oriented homogeneous offset field, which displaces the zero-field center of the quadrupole trap. In addition, the magnetic funnel is turned on, creating a transverse quadrupole field, in which the gradient increases with decreasing distance from the upper fiber tip. In particular, this transverse gradient reaches $\sim 6\,\mathrm{kG/cm}$ at the fiber tip, resulting in strong radial compression of the magnetic trap. The

---

[2] A more precise term to use here would be "position-dependent velocity distribution"

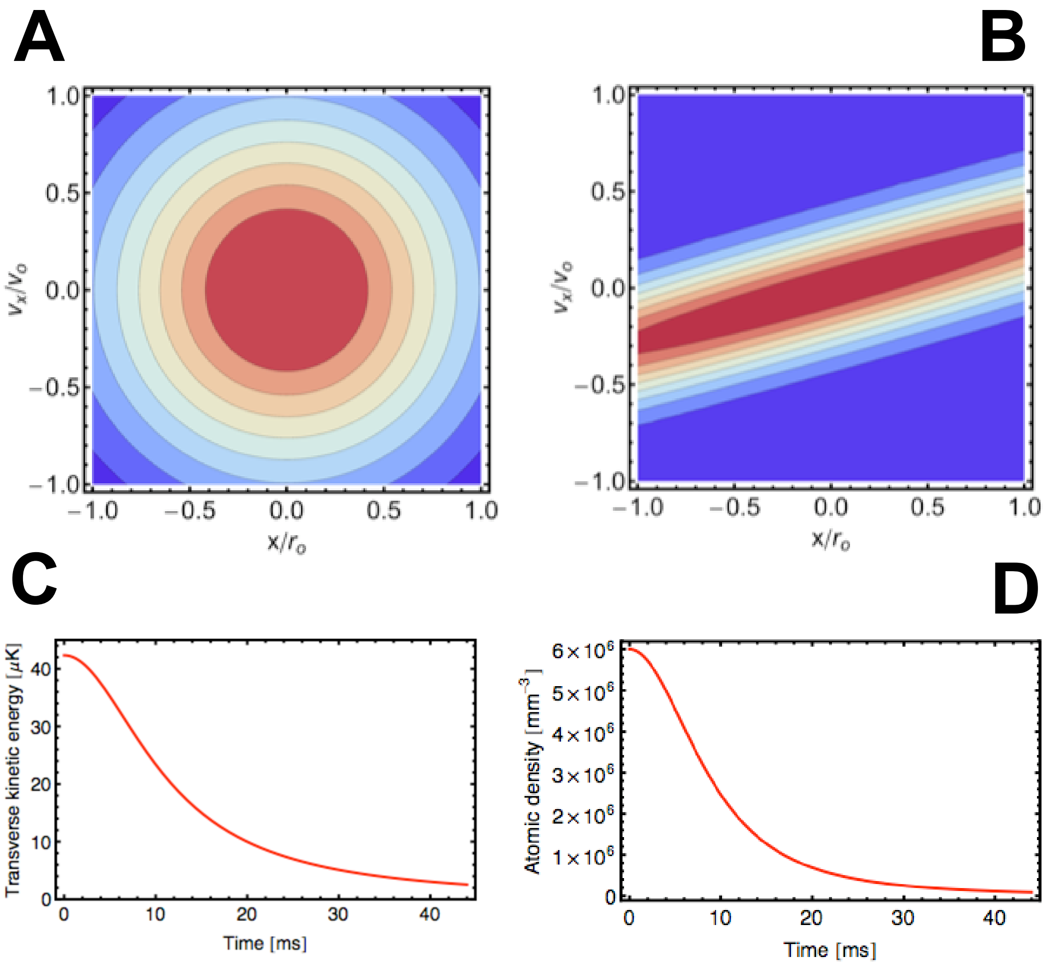

Figure 4.12: (A) Probability density function for position and velocity distribution in the x direction for an atom in the laser-cooled cloud at time $t_o = 0$, right after the molasses beam are turned off. (B) The same probability density function at time $t_{drop} = 36$ ms. (C) The transverse kinetic energy of atoms in the center of the cloud as a function of time. (D) Atomic density in the center of the cloud as a function of time. The atomic cloud parameters are $r_o = 1$ mm, $v_o = 9\ cm/s$, $N_o = 6 \times 10^6$, and $y_o = 6.3$ mm. These plots are based on calculations described in Appendix E.

complete transfer of the magnetic trap towards the fiber takes place over the course of 45 ms. This brings the atoms within a few hundred micrometers of the fiber tip and they load into the fiber as they arrive. An image of the atomic cloud guided by the magnetic funnel can be seen in Fig. 4.5B. At the end of the transfer period, all magnetic fields are shut off and the atoms are probed.

This procedure is the one that we originally planned to use for the loading sequence. However, it never worked quite as well as originally intended. Due to a design miscalculation, the MOT coils could not handle enough current to provide large enough magnetic field gradient to fully trap atoms against gravity. This made optimization of the system nearly impossible as the atoms kept leaking away and we were never able to magnetically trap more than a small fraction of the initial atomic cloud. Additionally, when current is pulsed through the funnel wires, the resulting heat pulse causes the fiber tip to shake slightly. Worse than that, the cumulative heat of the repeated experimental cycles would change the overall fiber coupling efficiency. This could be corrected by beam walking, but it would also require the system to run for about two hours before the fiber position stabilized and after that the funnel needed to be cycled constantly to maintain the steady state temperature of the fiber mount. While most of the data in Chapter 5 were obtained using this transfer procedure, we were relieved when we came up with the alternatives.

4.4.3 Hollow-beam atomic guide

An undesired consequence of the unrestrained expansion of the atomic cloud in 4.4.1 is that a part of the atoms cold enough to be pulled into the fiber-guided dipole trap will drift out of the trap's capture range during the time of the free fall. To herd these atoms back into the dipole trap's reach without the use of the magnetic funnel, we now use an atomic guide based on a hollow-beam blue-detuned dipole trap.

The hollow beam is generated using a combination of lenses and axicons (conical lenses) sketched out in Fig. 4.13A and described in more detail in Appendix D. This setup allows us to generate a vertical hollow beam that is close to collimated both in diameter and wall thickness in the region between the MOT site and ~ 1 mm above the fiber tip (Fig 4.13B). The idea behind this particular lens combination is to turn "inside out" an axicon-generated quasi-Bessel beam, which leads to an excellent suppression of light in the hollow part of the resulting beam [84]. The implementation itself was not without challenges as we had to work around the optics already in place for the other stages of the experiment. Additionally, due to differences between a real axicon and an idealized axicon, as well as extreme sensitivity to transverse alignment, attempts at either analytical description or numerical simulation of setups containing more than one axicon yielded results that were qualitative at best. Consequently, a significant part of the final design is the result of a trial-and-error approach. The winning combination of optics consist of two 175° axicons from Greyhawk Optics and a 75 cm focal-length lens between them, in addition to the $f \approx 20$ mm coupling

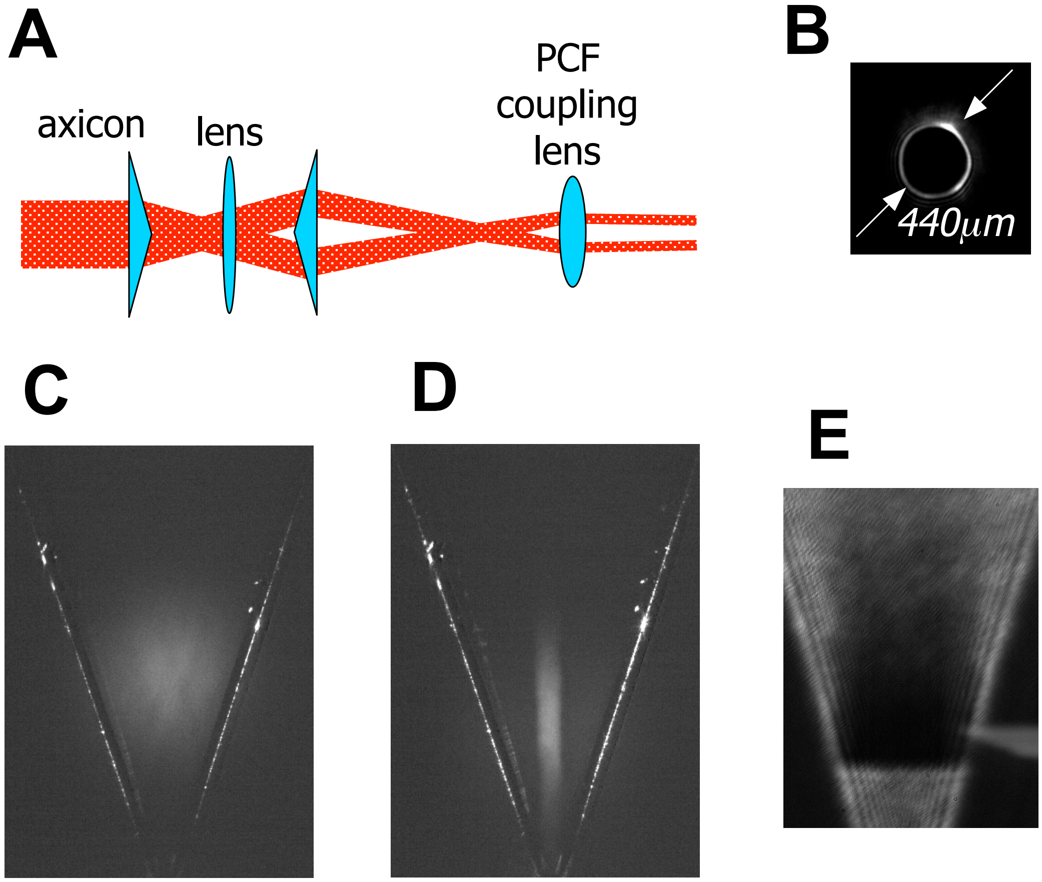

Figure 4.13: Hollow beam atomic waveguide (A) Schematics of the hollow beam generation. (B) CCD image of the hollow beam intensity distribution as expected about 1 mm above the fiber face. (C) Fluorescence image of the freely expanding atomic cloud 20 ms after its release from the optical molasses. (D) Fluorescence image of the atomic cloud guided by the blue detuned hollow beam 20 ms after the optical molasses beams are turned off. (E) Absorption image of the atoms collected in the hollow beam guide $\sim$ 1 mm above the fiber tip. Here, the hollow beam was intersected by a blue detuned Gaussian beam focused by a cylindrical lens into a sheet.

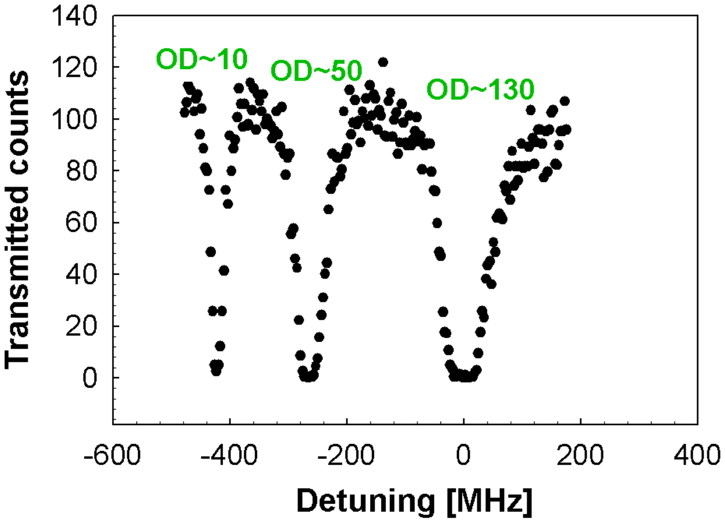

Figure 4.14: Frequency scan over the D_2 line of ^{87}Rb for $\sim$ 26000 atoms loaded inside the fiber. The atoms are optically pumped into the $F = 2$ state and then probed with linearly polarized light over the three transitions accessible from this state, $F = 2 \rightarrow F' = 1$ (left), $F = 2 \rightarrow F' = 2$ (middle), and $F = 2 \rightarrow F' = 3$ (right). The different observed optical depths agree nicely with the prediction (A.4) based on the relative strengths of these transitions determined by their Clebsh-Gordan coefficients.

lens above the PCF. Fine tuning of the hollow beam shape is done by adjusting the collimation of the input Gaussian beam.

The atom-guiding performance of the blue-detuned hollow beam generated with this setup can be seen in Fig. 4.13 C, D and E. The hollow beam with $P \approx 60$ mW and $\lambda \approx 780.20$ nm is turned on at the end of the atom cooling stage, and the atoms are then allowed to free-fall towards the fiber. Compared to the freely expanding cloud in 4.4.1, the use of the hollow beam guide improves the number of atoms loaded into the fiber by a factor of three to four.

4.5 Final remarks

Using the hollow-beam atomic guide, we achieved an optical depth of 100 inside the hollow core of the PCF for the first time in this experiment. We were able to push this a bit further further using a few additional tricks. First, splitting the fiber-coupled dipole trap and coupling it into the PCF simultaneously from both top and bottom appears to increase the capture range of the fiber-guided dipole trap above the fiber. We observed an increase in the number of loaded atoms by 30−50% this way, when the ratio between the powers of the exiting upward beam and entering downward beam above the fiber was between 1:1 and 1:2, and when we set the frequency difference between the beams to 20 MHz or more to avoid formation of a standing wave. Second, starting with a MOT cloud containing more atoms leads to more atoms loading into the fiber. Right now we can increase the number of initially collected atoms either by increasing the loading time (from 1s to 2s) or by increasing the rubidium vapor pressure. Using the former in combination with the two-beam fiber-coupled dipole trap and the blue-detuned hollow beam, we were able to observe OD ≈ 160, which is our current record. The rubidium vapor pressure could be increased by running more current through the rubidium dispensers, but we are somewhat reluctant to do this as it drastically decreases their lifetime. Additionally, if we optically pumped the atoms into an $m_F = 0$ state, a stronger atomic transition would be probed by the linearly polarized light. Overall, with the system in its current state, an optical depth of ~ 300 could probably be achieved.

Currently, the fundamental limit of our loading efficiency is that we rely on capturing the lower tail of the Maxwell-Boltzmann velocity distribution by the fiber-coupled dipole trap. Thus, the best we can do is to make sure that atoms in this tail are brought into the capture radius of this trap. This is the philosophy behind the use of both the magnetic funnel and the hollow-beam guide. To increase the loading efficiency, and thereby the number of loaded atoms, by an order of magnitude or more, one has to take a different approach. This involves increasing the phase space density of the atomic cloud, which in our current experiment remains more or less constant between the time the atoms are released from the optical molasses and the time they are loaded into the fiber core. In the most extreme case this means loading a Bose-Einstein condensate cloud into the fiber. This was successfully demonstrated in [21], but in our case it would lead to a severe decrease in the repetition rate of the experiment in addition to a somewhat increased technical complexity of the apparatus. A sufficient phase space density increase for our purposes can be achieved just by compressing and cooling the atomic cloud before it is moved to the vicinity of the fiber tip.

In conclusion, the tight confinement of light provided by the waveguide dramatically increases the electric field amplitude of the photons and allows them to propagate in this tightly focused form over distances unrestricted by diffraction. At the same time, the nearly stationary atoms transversely localized inside the waveguide create an optical medium with long coherence times that can almost perfectly overlap with the mode of the propagating light field. In addition, the probability of interaction between single photons and single atoms in the waveguide can approach unity, which in turn leads to large optical depths resulting from a small number of atoms. With the tools provided by atomic physics and quantum optics, atom-atom, atom-photon, and photon-photon interactions in this system have the potential to be engineered, controlled, and explored in ways that were previously not possible.

Chapter 5

Nonlinear optics with with tightly confined photons and atoms

In this chapter, we describe experiments that further demonstrate the strong atom-light coupling inside the hollow core PCF and allow us to control the optical properties of our system with light pulses containing as few as several hundred photons.

5.1 EIT with atoms confined to hollow core fiber

We now turn to coherent interaction between few atoms and photons in our system. To this end, we demonstrate electromagnetically induced transparency (EIT) [42, 32], where intra-atomic coherence induced by a control beam changes the transmission of a probe beam. For this we consider the 3-state 'Lambda' configuration of atomic states shown in Fig. 5.1A. In the presence of a strong control field, the weak probe field, resonant with the $|1\rangle \rightarrow |3\rangle$ transition, is transmitted without loss. The essence of EIT is the creation of a coupled excitation of probe photons and atomic spins ("dark-state polariton") [33] that propagates through the atomic medium with greatly reduced group velocity [46] and can be efficiently manipulated.

To demonstrate EIT, we first prepare the atoms in the $F = 1$ ground state, and then probe the medium with a linearly polarized probe tuned to the D1 $F = 1 \rightarrow F' = 1$ transition. In the absence of the control beam, the medium is completely opaque at resonance (Fig. 5.1C, black data points). In contrast, when a co-propagating control field resonant with the $F = 2 \rightarrow F' = 1$ transition is added, the atomic ensemble becomes transparent near the probe resonance (Fig. 5.1C, red data points). Figure 5.1D shows the individual pulse shape and its transmission and delay due to reduced group velocity v_g inside the atomic medium. For a probe pulse of half-width $t_p \sim 150\,\mathrm{ns}$ we observe a group delay t_d approaching $100\,\mathrm{ns}$, corresponding to reduction of group velocity to $v_g \approx 3\,\mathrm{km/s}$. Finally, Fig. 5.1E shows the resonant probe transmission as a function of the average number of photons contained in each

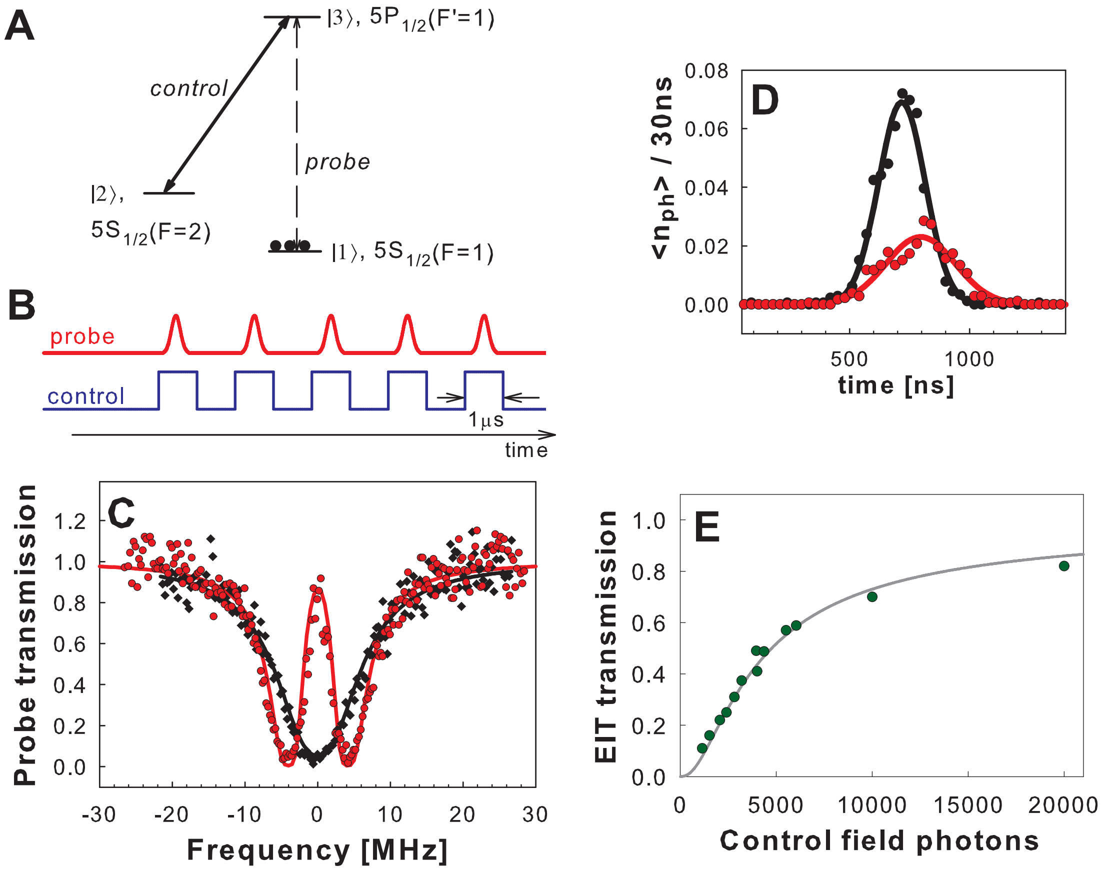

Figure 5.1: Electromagnetically induced transparency with atoms inside the fiber: (A) The atomic level scheme and the corresponding hyperfine states. (B) Both probe and control field are broken into a set of ~ 100 synchronized pulses sent through the fiber during the off-times of the dipole trap. (C) Transmission of the probe light through the fiber as a function of detuning from resonance in the presence of the control field (red data). The black data show probe transmission without the control field. (D) Individual probe pulse shape and delay. Here, $\langle n_{ph} \rangle$ represents the average number of photons detected in a 30 ns time bin. The reference pulse (black) is obtained without the presence of atoms, while the EIT pulse (red) is delayed. (E) Observed transmission of the probe pulses on resonance as a function of average number of photons in the $1\,\mu$s control field pulse and the prediction (grey line) obtained by evaluating eq. (5.2).

control field pulse. Remarkably, control pulses containing $\sim 10^4$ photons are sufficient to achieve almost complete transparency of an otherwise opaque system.

5.2 An all-optical switch inside a hollow optical fiber

The sensitive nature of the quantum interference underlying EIT enables strong non-linear coherent interaction between the dark-state polariton and additional light fields, which can be viewed as an effective photon-photon interaction [43, 81, 63]. An efficient nonlinear optical switch can be realized by adding to the EIT 'Lambda'-system a switch field coupling the state $|2\rangle$ to an excited state $|4\rangle$ (Fig. 5.2A), as proposed by Harris and Yamamoto [45]. In this scheme, the switching photons interact with flipped atomic spins within the slow dark-state polariton, causing a simultaneous absorption of a probe and a switch photon [94, 16, 20].

In our experiment, an additional switching field on the D2 $F = 2 \rightarrow F' = 3$ transition (Fig. 5.2A) controls the transmission through the EIT medium. Switching is achieved when all three involved light fields (probe, control and switching field) are overlapping in time (Fig. 5.2B). As shown in Figure 5.2C, in the absence of the switching field (red data), we observe high transmission of the probe beam on resonance due to EIT. When the switch field is turned on, this transmission is reduced. The strength of the reduction depends on the switch field intensity, which, for a fixed switch pulse length, is determined by the number of photons contained in the switch pulse (Fig. 5.2D). Experimentally, we observe best switching results for switch pulses of length $t_s \approx t_p + t_d$. We find a 50% reduction of the initial transmission for a total number of ~ 700 switch photons per pulse. Figure 5.2E presents the truth table of our switch. In the case of no probe pulse (0/0 and 0/1 settings of the switch) only background noise from the control field is detected, which is orders of magnitude smaller than the single photon per probe pulse.

5.2.1 Analysis of pulse transmission

We now turn to the detailed analysis of the nonlinear behavior of our atomic medium. In the case when the resonant control and switching pulses are longer than the weak probe pulse, the effect of the atomic medium on such probe pulses with carrier frequency ω_p is given by $\mathcal{E}_{\mathrm{out}}(t) = \frac{1}{\sqrt{2\pi}} \int \mathrm{d}\omega\, \mathcal{E}_{\mathrm{in}}(\omega)\, e^{\imath \frac{\mathrm{OD}}{2} f(\omega)}\, e^{-\imath \omega t}$, where $\mathcal{E}_{\mathrm{in}}(\omega)$ is the Fourier transform of the slowly varying envelope $\mathcal{E}_{in}(t)$ of the probe pulse. The frequency dependent atomic response to probe light $f(\omega)$ is given by [81, 45]

$$f(\omega) = \frac{\gamma_{13} \left(|\Omega_s|^2 - 4\delta_{12}\delta_{24} \right)}{\delta_{24} \left(4\delta_{12}\delta_{13} - |\Omega_c|^2 \right) - \delta_{13} |\Omega_s|^2}. \tag{5.1}$$

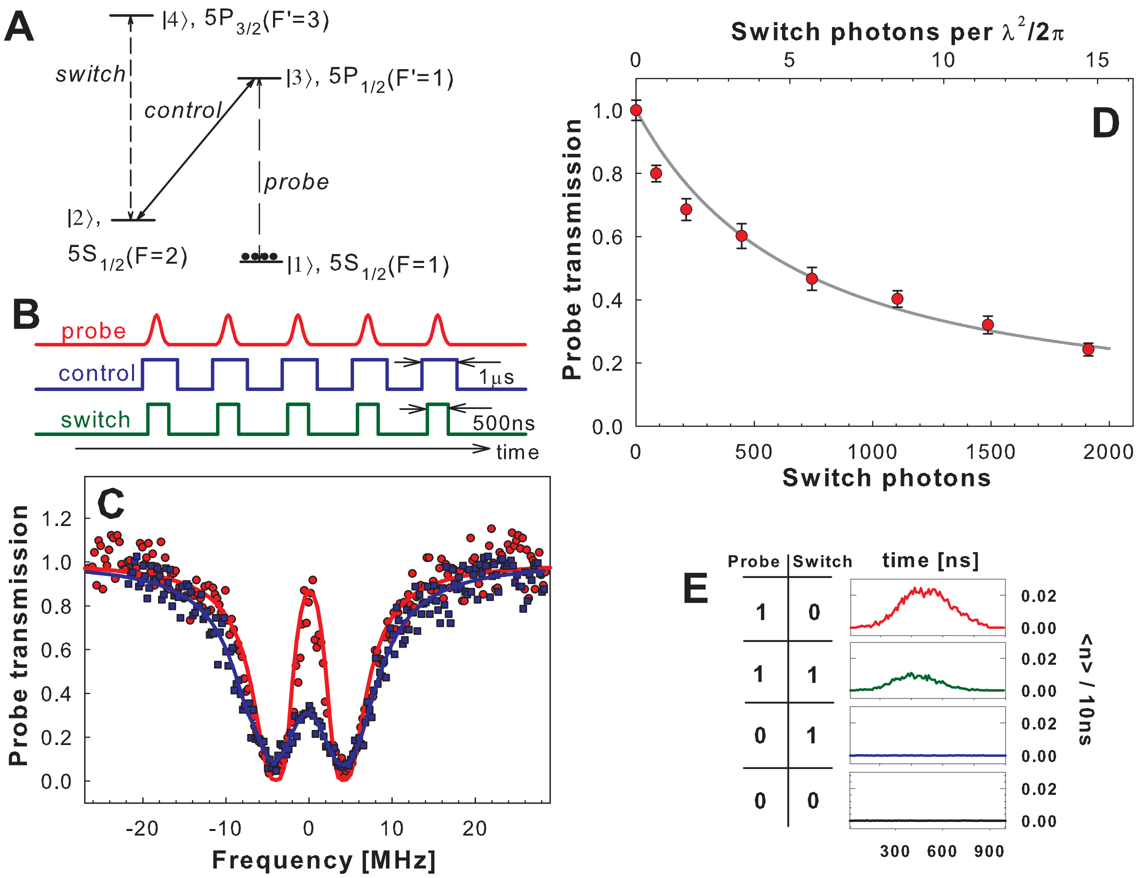

Figure 5.2: An all-optical switch: (A) The atomic level scheme with corresponding hyperfine states. (B) Probe, control and switch fields are broken into a set of ~ 100 synchronized pulses sent through the fiber during the off-times of the dipole trap. (C) Probe transmission through the fiber without (red) and with (blue) the switch field present. Solid lines are fits of equation (5.2). (D) Observed transmission versus average number of switch photons per pulse. The solid grey line is the prediction based on equation (5.2). The transmission is normalized to the EIT transmission in the absence of the switch photons. (E) Truth table of the switch, showing the detected photons in the output port of the switch system as a function of the presence of the probe and switch field pulses. Data are presented for probe pulses containing on average ~ 2 photons and with $\sim 1/e$ attenuation of transmission in the presence of the switch photons.

Here, $\Omega_{s,c} = \frac{\mu_{s,c} E_{s,c}}{\hbar}$ are the Rabi frequencies of the switch and control fields, with $\mu_{s,c}$ being the respective dipole matrix elements. The complex detunings δ_{ij} are defined as $\delta_{ij} = \delta_p + \imath\gamma_{ij}$, with γ_{ij} being the dephasing rates between levels i, j, while $\delta_p = \omega_p + \omega - \omega_{13}$, where ω_{13} is the frequency of the $|1\rangle \to |3\rangle$ transition. The number of input and output photons is given by $N_{in,out} = \int \mathrm{d}t\, |\mathcal{E}_{\mathrm{in,out}}(t)|^2$. In what follows, we consider input pulses with Gaussian envelope $\mathcal{E}_{\mathrm{in}}(t) \sim e^{-\frac{t^2}{2t_p^2}}$, in which case the transmission through our atomic medium is

$$T(\omega_p, \mathrm{OD}) = \frac{N_{out}}{N_{in}} = \frac{t_p}{\sqrt{\pi}} \int \mathrm{d}\omega\, e^{-t_p^2\omega^2}\, e^{-\mathrm{OD}\,\mathrm{Im} f(\omega)}. \tag{5.2}$$

We fit expression (5.2) to the observed absorption profiles such as the ones shown in figures 5.1C and 5.2C to extract the control and switch Rabi frequencies, optical depth and ground state decoherence rate. We next use these parameters to compare our observed EIT and coherent switch data to the theoretical prediction. The solid line in Fig. 5.1E shows the calculated EIT transmission as a function of control pulse photons. Similarly, the solid line in Fig. 5.2D shows the on-resonance attenuation of the probe pulse as a function of the number of switch photons. In both cases, we find excellent agreement between our experimental data and the theoretical model.

In the relevant case of a resonant probe field, equation (5.1) can be approximated by

$$T = \frac{\exp\left(-N_s \left(\frac{\mu_s}{\mu_p}\right)^2 \frac{3}{\pi} \frac{\lambda^2}{A} \frac{t_d}{t_p + t_d}\right)}{\sqrt{1 + \frac{16 t_d^2}{\mathrm{OD}\, t_p^2}}}. \tag{5.3}$$

Here, N_s is the number of switch photons. Furthermore, we have assumed $\Omega_s \ll \Omega_c$, $\gamma_{12} = 0$, $\gamma_{13} \approx \gamma_{24}$ and used $t_d = L/v_g = \frac{\mathrm{OD}\gamma_{13}}{|\Omega_c|^2}$, with L being the length of the medium. For the investigated case of a relatively weak probe transition and resulting OD ≈ 3, the delay time is small ($t_d \sim t_p$) and the probe pulse is never fully stored inside the medium. If the OD is increased (either by improving the atom loading efficiency or using a stronger probe transition), $t_d \gg t_p$ and the whole probe pulse is contained inside the medium as a dark state polariton in a mostly atomic form. In this case, it follows from equation (5.3) that $N_s \sim \frac{A}{\lambda^2}$ switch photons attenuate the probe pulse by a factor of $1/e$. This ideal limit can be easily understood. In the case of a single slow probe photon, the polariton contains only a single atomic spin at any time. Consequently, absorption of a single switch photon, which occurs with probability $p \sim \lambda^2/A$, is required to destroy this coherent atomic excitation.

5.3 Outlook

Further improvements in nonlinear optical efficiency are possible by either simultaneously slowing down a pair of pulses to enable long interaction time [62] or using stationary-pulse techniques from Chapter 3. The former will decrease the number of photons required in the switch pulse by a factor $\sim \sqrt{OD}$ as described in section B.2.3 of Appendix B. In the latter case, a standing wave control field formed by two counter-propagating beams is used to form an EIT Bragg grating in which the probe pulse can be completely stopped with non-vanishing photonic component. In particular, application of this scheme inside the PCF has been proposed for single-photon-controlled switching through an interaction of single-photon stationary light pulses, with probability of interaction between two single photons scaling as $\sim OD\lambda^2/A$ [3]. With a relatively modest improvement in atom loading resulting in optical depth $OD > 100$, achieving deterministic nonlinear switching with two guided photons appears within reach.

These experimental demonstrations introduce a novel physical system that opens up unique prospects in quantum and nonlinear optics. In addition to all-optical switching, our system can be used to implement efficient photon counting [49, 50] by combining photon storage with interrogation of spin-flipped atoms via the cycling transition. Finally, the present demonstration opens up the possibility to create strongly interacting many-body photon states [19], which may give new insights into the physics of non-equilibrium strongly correlated systems.

Chapter 6

Conclusions

6.1 Summary

This work has demonstrated novel techniques and methods focused on increasing the interaction probability between a single photon and a single atom with the goal of making use of such interaction for nonlinear optics at low light levels. The main results of this work can be summarized as follows:

1) Electromagnetically induced transparency can by used to quickly change the optical properties of atomic ensembles from completely transparent to behaving like a Bragg-grating mirror and back. This was used to create a stationary pulse of light for the first time.

2) Laser-cooled atoms were successfully loaded into a single-mode hollow core photonic waveguide and trapped there tens of milliseconds. This system allows one to confine both atoms and photons into an area comparable the the photons' wavelength. The result is a significantly increased probability of interaction between a single photon and a single atom on a single pass, which allows ensembles containing as few as ~ 100 atoms to become optically dense.

3) Using cold atoms confined to this hollow waveguide, we were able to demonstrate a fiber-based all-optical switch activated at energies corresponding to a few hundred optical photons per pulse. This was achieved by using quantum optical techniques to generate slow light propagation and a large nonlinear interaction between light beams.

6.2 Future directions

At the moment, our experimental effort is focused on combining the large optical depth of atomic ensembles trapped inside the hollow core PCF with stationary light pulse techniques with the goal of achieving nonlinear interactions between single-photon pulses. The first results look promising, but many challenges still remain to be conquered.

Looking beyond the current experimental setup, one can think of additional directions in which this work could be developed.

Modulating the dipole trap has so far allowed us to probe the atoms mostly without having to worry about the trap's negative effects. However, the AC Stark shifts of the atomic levels induced by the trapping light, as well as the not completely negligible heating resulting from the trap modulation, present technical limits on the potential applications of this promising system. Use of a different atomic species, for which the trap's negative effect can be avoided through the use of a "magic-wavelength" dipole trap, will open a host of experimental possibilities that are currently difficult to access with rubidium atoms.

Additionally, use of a different single-mode waveguide could further increase the single-photon single-atom interaction probalility, if the diameter of the guided mode is smaller than that of the photonic crystal fiber used in the setup now. In the last couple of years, several candidates for this have become available, most notably slot waveguides and PCFs with ~ 1 μm-diameter hollow core [92, 77].

Going beyond direct applications of this work in low-level nonlinear optics, recent theoretical works have already proposed the use of stationary light pulses and laser-cooled atoms trapped inside a single mode photonic waveguide as platforms for exploring novel physical phenomena in areas ranging from relativistic effects [74] to many-body physics, such as Bose-Einstein condensation of dark state polaritons [34] and fermionization of photons [19]. Given these and other positive responses so far, we are confident that this work will lead to applications and experimental studies in a number of fields, including nonlinear optics, atomic physics, physics of one-dimensinal systems, precision measurements, quantum simulation, and quantum information.

Appendix A

Properties of Rubidium^{87}

Here we briefly list the properties of rubidium^{87} relevant for our experiments as taken from [86]. Reference [86] also lists additional properties as well as the original references for them.

A.1 Physical and optical properties

Table A.1: Physical properties of rubidium^{87}

Atomic Number	37
Neutrons and Protons	87
Relative natural Abundance	27.83(2)%
Atomic Mass	$1.44316060(11) \times 10^{-25}$kg
Density at 25°C	1.53 g.cm^{-3}
Melting Point	39.31°C
Boiling Point	688°C
Vapor Pressure at 25°C	3.0×10^{-7} Torr
Nuclear Spin	3/2

A.2 Number density of rubidium in the vapor cell

We estimate the the number density of rubidium atoms in the spectroscopy vapor cell using the ideal gas law and a pressure-temperature equation from [70]:

$$\begin{aligned}\log_{10} P_v &= -94.048\,26 - \frac{1961.258}{T} - 0.037\,716\,87\,T + 42.575\,26\log_{10} T \\ \log_{10} P_v &= 15.882\,53 - \frac{4529.635}{T} + 0.000\,586\,63\,T - 2.991\,38\log_{10} T \qquad \text{(A.1)}\end{aligned}$$

Table A.2: Optical properties of the D_1 line of rubidium^{87}

D_1 line ($5^2S_{1/2} \rightarrow 5^2P_{1/2}$) Transition Dipole Matrix Element $\langle J = 1/2 \| er \| J' = 1/2 \rangle$	2.992(3) ea_0 $2.537(3) \times 10^{-29}$C.m
Frequency	2π·377.10746345(4) THz
Wavelength (Vacuum)	794.978 850 9(8) nm
Wavelength (Air)	794.765 69 nm
Lifetime	27.70(4) ns
Natural Line Width Γ	2π·5.746(8) MHz

Table A.3: Optical properties of the D_2 line of rubidium^{87}

D_2 line ($5^2S_{1/2} \rightarrow 5^2P_{3/2}$) Transition Dipole Matrix Element $\langle J = 1/2 \| er \| J' = 3/2 \rangle$	4.227(5) ea_0 $3.584(4) \times 10^{-29}$C.m
Frequency	2π·384.230 484 468 5(62) THz
Wavelength (Vacuum)	780.241 209 686(13) nm
Wavelength (Air)	780.032 00 nm
Lifetime	26.24(4) ns
Natural Line Width Γ	2π·6.065(9) MHz

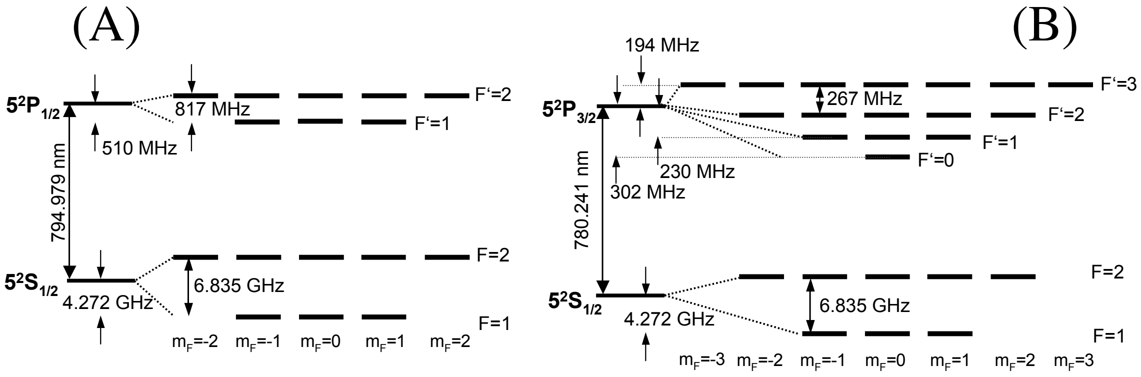

Figure A.1: Atomic-level structure and frequency spacings for (A) the D_1 line and (B) the D_2 line of ^{87}Rb including the Zeeman sublevels.

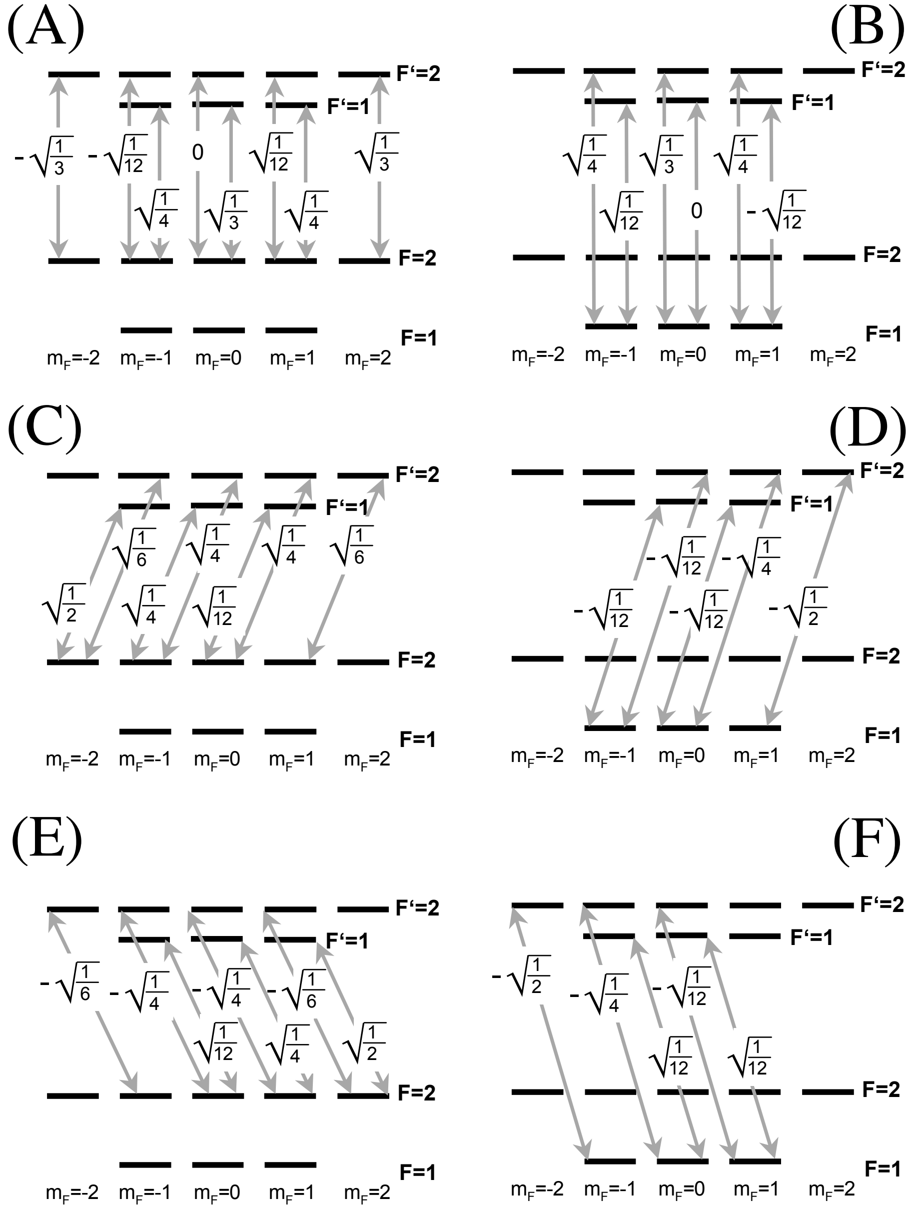

Figure A.2: ^{87}Rb D_1 line ($5^2S_{1/2} \rightarrow 5^2P_{1/2}$) Dipole Matrix Elements expressed as multiples of $\langle J = 1/2||er||J' = 1/2\rangle$: (A) and (B) light polarized linearly along the direction of the quantization axis (π-transitions); (C) and (D) right circularly polarized light coupling the σ_+-transitions; (E) and (F) left circularly polarized light coupling the σ_--transitions.

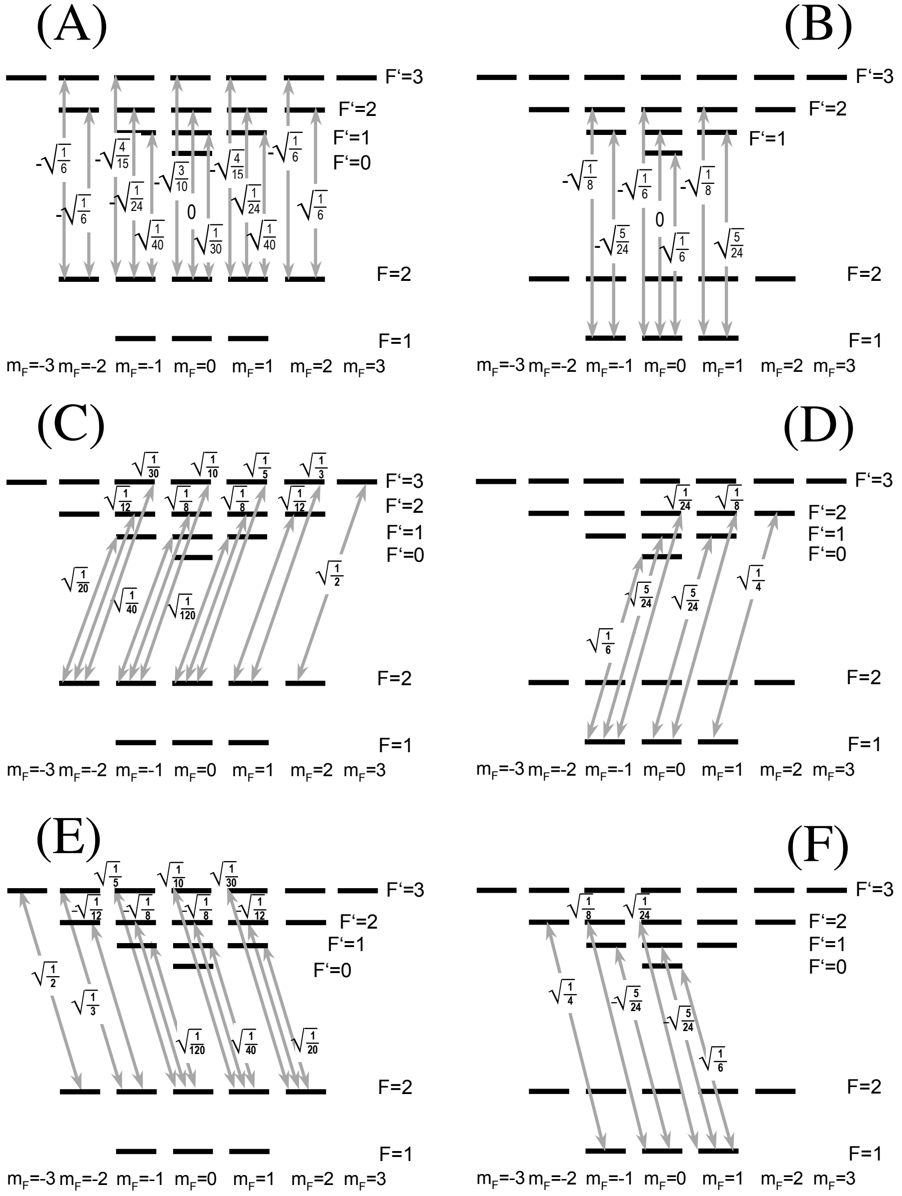

Figure A.3: ^{87}Rb D_2 line ($5^2S_{1/2} \rightarrow 5^2P_{3/2}$) Dipole Matrix Elements expressed as multiples of $\langle J = 1/2||er||J' = 3/2\rangle$: (A) and (B) light polarized linearly along the direction of the quantization axis (π-transitions); (C) and (D) right circularly polarized light coupling the σ_+-transitions; (E) and (F) left circularly polarized light coupling the σ_--transitions.

Here, the first equation describes the vapor-pressure for rubidium in the solid phase ($T < 39.31°C$), while the second one is for the liquid phase ($T > 39.31°C$).

A.3 Scattering cross-section of unpolarized rubidium atoms

For an atom in ground state $|b\rangle = |J,\, F,\, m_F\rangle$ interacting with light of a particular frequency and polarization that couples it to excited state $|a\rangle = |J',\, F',\, m'_{F'}\rangle$, the scattering cross-section of the interaction is given by (2.5), where

$$\mu_{ab} = \tilde{\mu}_{ab}\langle J||er||J'\rangle \tag{A.2}$$

with the values of $\tilde{\mu}_{ab}$ given in figures A.2 and A.3 for the transitions relevant to this work. For example, for an atom in state $|J = 1/2,\, F = 2,\, m_F = 2\rangle$ coupled resonantly with right circularly polarized (σ^+) light to state $|J' = 3/2,\, F' = 3,\, m'_{F'} = 3\rangle$, $\mu_{ab} = 2.534 \times 10^{-29} C \cdot m$ and the scattering cross-section is $\sigma_{ab} = 2.907 \times 10^{-9} cm^2$.

When we probe an ensemble of N atoms that are in ground state $|J,\, F\rangle$ with light of a particular polarization, unless the atoms were somehow prepared to be in a particular m_F Zeeman state beforehand, we can assume that the atoms are distributed over all possible m_F states. Such an ensemble is then treated as a mixture of several ensembles, each with atoms in a particular Zeeman state. For practical purposes, the effective scattering cross-section of such an interaction is given by a sum of the m_F to $m_{F'}$ cross-sections weighted by the fraction of atoms in each m_F state. For example, for a linearly polarized probe probing on the D_2 line an ensemble of atoms equally distributed over all m_F levels of the $F = 2$ ground state,

$$\sigma_{eff}(F = 2 \rightarrow F') = \frac{1}{5}\left(\sum_{m_F=-2}^{2} |\tilde{\mu}_{(F=2, m_F; F', m'_F = m_F)}|^2\right) |\langle J||er||J'\rangle|^2 \frac{\omega_{D_2}}{\hbar\epsilon_o c\frac{\Gamma}{2}} \tag{A.3}$$

Using this approach, we can predict the ratio between the optical depths of the transitions scanned in Fig. 4.14 to be

$$OD_{2\rightarrow 1} \div OD_{2\rightarrow 2} \div OD_{2\rightarrow 3} \approx 1 \div 5 \div 14. \tag{A.4}$$

Appendix B

EIT: Beyond a three level atom

In this appendix we provide a brief discussion of a few additional concepts related to EIT and its applications to nonlinear optics. These concepts are generally known, so the goal of this appendix is mostly to provide a quick reference from an experimentalist's point of view.

B.1 Probing multiple excited states

Before proceeding to the main topics, we will briefly discuss the interaction between a weak probe and an atom with multiple excited states, such as the one in Fig. B.1A), as it will come in handy later on. The propagation of the probe inside a medium consisting of such atoms can be described through a more general form of equation (2.14),

$$\frac{\partial}{\partial z}\mathcal{E}_p + \frac{1}{c}\frac{\partial}{\partial t}\mathcal{E}_p = in\frac{\nu}{\epsilon_o c}\sum_j \mu_{bj}\tilde{\rho}_{jb}, \tag{B.1}$$

where $\tilde{\rho}_{jb}$ is the slowly varying part of the density matrix element, n is the number of atoms per unit volume, and we are summing over all the excited states. Since in the case of a weak probe $\tilde{\rho}_{jb}$ can be approximated by the wavefunction coefficient $\tilde{j}$, for the atom from Fig. B.1 we can write

$$\begin{aligned} \frac{\partial}{\partial z}\mathcal{E}_p + \frac{1}{c}\frac{\partial}{\partial t}\mathcal{E}_p &= in\frac{\nu}{\epsilon_o c}(\mu_{ba}\tilde{a} + \mu_{bd}\tilde{d}) \\ &= i\frac{n\hbar}{2}\left(\frac{\Gamma_a\sigma_{ab}}{\mu_{ab}}\tilde{a} + \frac{\Gamma_d\sigma_{db}}{\mu_{db}}\tilde{d}\right), \end{aligned} \tag{B.2}$$

where σ_{jb} is the resonant scattering cross-section of the transition between levels $|b\rangle$ and $|j\rangle$, and in steady state

$$\tilde{a} = i\frac{\mu_{ab}}{2\hbar}\mathcal{E}_p\frac{1}{\frac{\Gamma_a}{2} - i\delta_1} \tag{B.3}$$

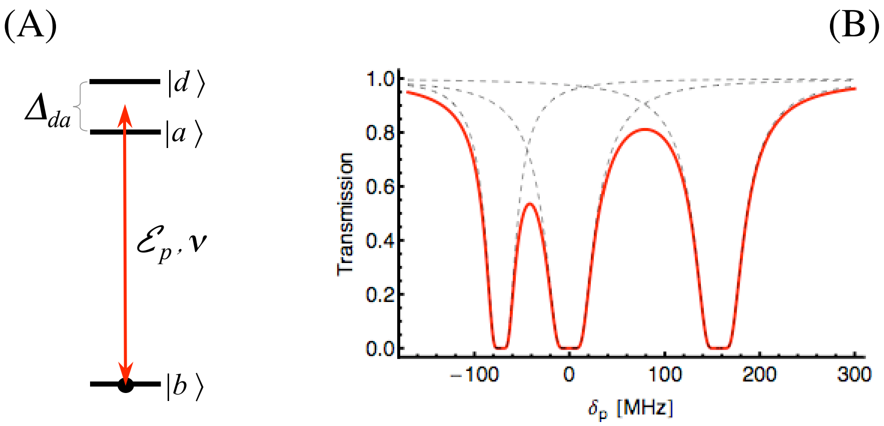

Figure B.1: (A) A weak probe interacting with an atom that has two excited states spaced closely in frequency. (B) Calculated transmission of a weak linearly polarized continuous wave probe through an ensemble of cold rubidium^{87} atoms. The probe is tuned to the D_2 line and is scanned over the allowed $F = 1 \rightarrow F'$ transitions, where $\delta_p = 0$ corresponds to resonance with $F = 1 \rightarrow F' = 1$ (solid red line). The on-resonance optical depth for the $F = 1 \rightarrow F' = 1$ transition is 50, where we assume equal populations for all Zeeman sublevels of the ground state. The dashed line curves correspond to the absorptions from each excited state alone.

$$\tilde{d} = i\frac{\mu_{db}}{2\hbar}\mathcal{E}_p\frac{1}{\frac{\Gamma_d}{2} - i\delta_2} = i\frac{\mu_{db}}{2\hbar}\mathcal{E}_p\frac{1}{\frac{\Gamma_d}{2} + i\Delta_{da} - i\delta_1}$$

with $\delta_1 = \nu - \omega_{ab}$ and $\delta_2 = \nu - \omega_{db} = \delta_1 - \Delta_d a$. A calculated scan of a weak probe over a part of the D_2 line of rubidium^{87} obtained through this approach, can be seen in Fig. B.1B.

B.2 Effects of a third field coupled to a fourth level

Consider a three-level lambda system with an additional atomic level $|d\rangle$ coupled to level $|c\rangle$ through a field with Rabi frequency $\Omega_s = \frac{\mu_{dc}}{\hbar}\mathcal{E}_s$ detuned by $\Delta_s = \omega_s - \omega_{dc}$ from resonance (Fig. B.2A). Following the treatment from section 2.2, the slowly varying parts of the wavefunction coefficients will be described by the following equations of motion:

$$\begin{aligned}
\dot{\tilde{a}} &= -(\frac{\Gamma}{2} - i\delta_p)\tilde{a} + \frac{i}{2}\Omega_c\tilde{c} + i\frac{\mu_{ab}}{2\hbar}\mathcal{E}_p b \\
\dot{b} &= i\frac{\mu_{ab}}{2\hbar}\mathcal{E}_p^*\tilde{a} \qquad\qquad (B.4) \\
\dot{\tilde{c}} &= -(\gamma - i[\delta_p - \delta_c])\tilde{c} + \frac{i}{2}\Omega_c^*\tilde{a} + \frac{i}{2}\Omega_s^*\tilde{d}
\end{aligned}$$

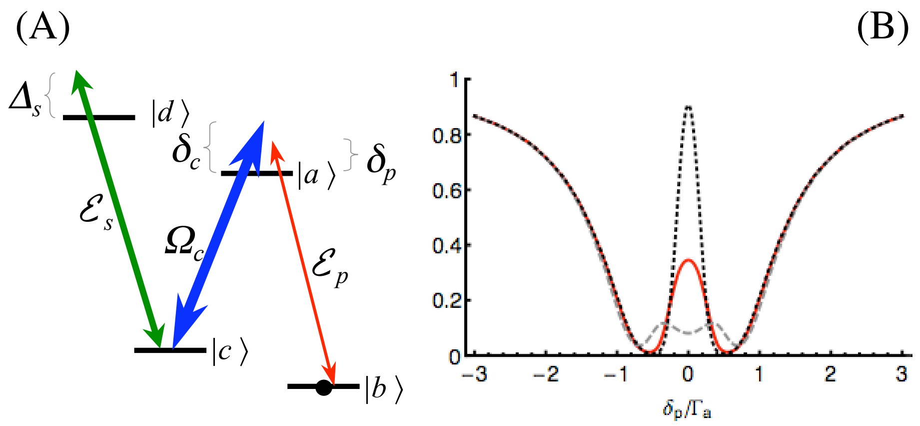

Figure B.2: (A) Four level system interacting with three light fields. (B) Calculated transmission of a weak probe through such system based on equation (B.5) with $OD = 5$, $\Gamma_d = \Gamma_a$, $\delta_c = \Delta_s = 0$, and $\Omega_c = \Gamma_a$. The black dotted line corresponds to $\Omega_s = 0$, red solid line to $\Omega_s = 0.5\Omega_c$, and gray dashed line to $\Omega_s = \Omega_c$.

$$\dot{\tilde{d}} = -(\frac{\Gamma_d}{2} - i[\delta_p - \delta_c + \Delta_s])\tilde{d} + \frac{i}{2}\Omega_s\tilde{c}$$

In steady state, assuming $b \approx 1$ (valid in the weak probe limit), (B.4) will yield:

$$\begin{aligned} \tilde{d} &= i\frac{\Omega_s}{2\tilde{\Gamma}_s}\tilde{c} \\ \tilde{c} &= i\frac{\Omega_c^*}{2}\tilde{a}\frac{1}{\tilde{\gamma} + \frac{|\Omega_s|^2}{4}\frac{1}{\tilde{\Gamma}_s}} \\ \tilde{a} &= i\frac{\mu_{ab}}{2\hbar}\mathcal{E}_p\frac{1}{\tilde{\Gamma}_a + \frac{|\Omega_c|^2}{4}\frac{1}{\tilde{\gamma} + \frac{|\Omega_s|^2}{4}\frac{1}{\tilde{\Gamma}_s}}} \end{aligned} \tag{B.5}$$

Here, $\tilde{\gamma} = \gamma - i(\delta_p - \delta_c)$, $\tilde{\Gamma}_a = \frac{\Gamma}{2} - i\delta_p$, and $\tilde{\Gamma}_d = \frac{\Gamma_d}{2} - i(\delta_p - \delta_c + \Delta_s)$. This corresponds to an EIT system with $\tilde{\gamma}' = \tilde{\gamma} + \frac{|\Omega_s|^2}{4\tilde{\Gamma}_d}$. Additionally, the last equation of (B.5) can be rewritten into the following form:

$$\tilde{a} = i\frac{\mu_{ab}}{2\hbar}\mathcal{E}_p\frac{\gamma - i(\delta_p - \delta_c) + \frac{1}{4}\left(\frac{\Gamma_d}{2} + (\delta_p - \delta_c + \Delta_s)\right)\frac{|\Omega_s|^2}{\frac{\Gamma_d^2}{4} + (\delta_p - \delta_c + \Delta_s)^2}}{\tilde{\Gamma}_a(\tilde{\gamma} + \frac{|\Omega_s|^2}{4\tilde{\Gamma}_d}) + \frac{|\Omega_c|^2}{4}} \tag{B.6}$$

This form allows us to more easily compare the behavior of the system with equation (2.15) describing $\tilde{a}$ for the case when when only the probe and control field are present. We will discuss the behavior of the system in two limits of practical importance.

B.2.1 Resonant case

For $\Delta_s \to 0$ and $\frac{\Gamma_d}{2} \gg \delta_p - \delta_c$, equation (B.6) will essentially simplify to the form of an EIT with

$$\begin{aligned} \gamma' &= \gamma + \frac{|\Omega_s|^2}{2\Gamma_d} \\ \delta_p - \delta_c &\to (\delta_p - \delta_c)\left(1 - \frac{|\Omega_s|^2}{\Gamma_d^2}\right) \end{aligned} \tag{B.7}$$

This case describes the all-optical switch demonstrated in Chapter 5, in which the transmission of the probe light through the system is controlled by the intensity of the switching field $\mathcal{E}_s$. A plot of the transmission of the probe as a function of frequency can be seen in (Fig. B.2B).

Switch contrast

The power in $\mathcal{E}_s$ necessary to operate this scheme as an all-optical switch is given by the the required maximum transparency of the system under EIT conditions and the level to which this transparency needs to be suppressed during the switch operation. This power is (up to a constant) given by $|\Omega_s|^2$, and it determines the number of photons in the switch pulse.

Let us assume that the required power transmission through our EIT system on resonance is T_{max}. From equation (2.17), we get

$$T_{max} = exp\left(-\mathrm{OD}\frac{\frac{\Gamma_a}{2}}{\frac{\Gamma_a}{2} + \frac{|\Omega_c|^2}{4\gamma}}\right) \approx exp\left(-\mathrm{OD}\frac{2\gamma\Gamma_a}{|\Omega_c|^2}\right) \tag{B.8}$$

This sets the lower boundary on the control field Ω_c:

$$|\Omega_c|^2 = 2\gamma\Gamma_a\left(\frac{\mathrm{OD}}{-\mathrm{ln}T_{max}} - 1\right) \approx \mathrm{OD}\frac{2\gamma\Gamma_a}{-\mathrm{ln}T_{max}} \tag{B.9}$$

In the presence of Ω_s, we now require the transmission of the system to change from T_{max} to qT_{max}, where $q < 1$ is the desired contrast between the two states of the switch. Combining (B.8) and (B.7), we obtain

$$qT_{max} \approx exp\left(-\mathrm{OD}\frac{2\left(\gamma + \frac{|\Omega_s|^2}{2\Gamma_d}\right)\Gamma_a}{|\Omega_c|^2}\right) \tag{B.10}$$

which gives us a lower limit on the switch field Ω_s:

$$|\Omega_s|^2 \approx \frac{\mathrm{ln}q}{\mathrm{ln}T_{max}} 2\gamma\Gamma_d \tag{B.11}$$

This result also implies that the ratio between the powers of the switching and control fields is

$$\frac{|\Omega_s|^2}{|\Omega_c|^2} \approx -\frac{1}{2}\frac{\Gamma_a}{\Gamma_d}\frac{\mathrm{ln}q}{OD} \tag{B.12}$$

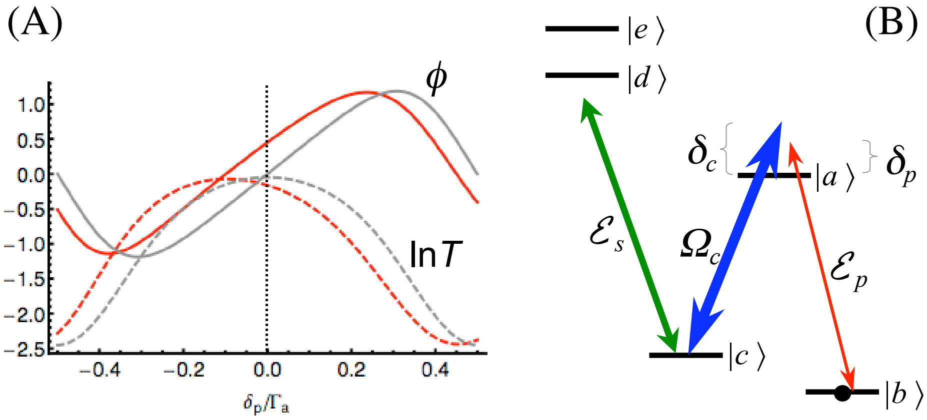

Figure B.3: (A) The calculated phase ϕ a weak probe acquires by propagating through the system of Fig. B.2B based on equation (B.5). The parameters are $OD = 5$, $\Gamma_d = \Gamma_a$, $\delta_c = 0$, $\Delta_s = -10\Gamma_a$, $\Omega_c = \Gamma_a$, and $\Omega_s = 2\Omega_c$ (solid red line) with the solid gray line corresponding to $\Omega_s = 0$ for comparison. The dashed lines plot the natural logarithm of the probe's power transmission through the system for $\Omega_s = 2\Omega_c$ (red) and $\Omega_s = 0$ (gray). (B) An EIT system in which Ω_s couples to two off-resonant levels.

B.2.2 Far off-resonant case

For $\Delta_s \gg \frac{\Gamma_d}{2}$ and $\Delta_s \gg \delta_p - \delta_c$, equation (B.6) will again simplify back to the original EIT but this time with

$$\begin{aligned} \delta_p - \delta_c &\rightarrow \delta_p - \delta_c - \frac{|\Omega_s|^2}{4\Delta_s} \\ \gamma' &= \gamma + \frac{\Gamma_d}{8}\frac{|\Omega_s|^2}{\Delta_s^2} \end{aligned} \tag{B.13}$$

Thus for large enough Δ_s the power transmission of the probe will not be affected, however the presence of the Ω_s field will allow us to control the phase of the probe light (Fig. B.3A) by introducing an effective two-photon detuning into the system as first proposed by [81].

Treatment of multiple off-resonant levels

It is often the case that the field $\mathcal{E}_s$ can couple to more than one state. If the coupling to one of the levels is resonant, the effect of this level will dominantly determine the behavior of the system and the other levels can usually be neglected. However, if $\mathcal{E}_s$ is resonant with none of the transitions, such as in Fig. B.3B, one might need to take into account the effects of multiple levels to determine the system's behavior. In particular, for the system in Fig. B.3B, the stochastic wavefunction method will lead to the following set of differential equations:

$$\begin{aligned}
\dot{\tilde{a}} &= -(\frac{\Gamma}{2} - i\delta_p)\tilde{a} + \frac{i}{2}\Omega_c\tilde{c} + i\frac{\mu_{ab}}{2\hbar}\mathcal{E}_p b \\
\dot{b} &= i\frac{\mu_{ab}}{2\hbar}\mathcal{E}_p^*\tilde{a} \\
\dot{\tilde{c}} &= -(\gamma - i[\delta_p - \delta_c])\tilde{c} + \frac{i}{2}\Omega_c^*\tilde{a} + \frac{i}{2}\Omega_d^*\tilde{d} + \frac{i}{2}\Omega_e^*\tilde{e} \\
\dot{\tilde{d}} &= -(\frac{\Gamma_d}{2} - i[\delta_p - \delta_c + \Delta_d])\tilde{d} + \frac{i}{2}\Omega_d\tilde{c} \\
\dot{\tilde{e}} &= -(\frac{\Gamma_e}{2} - i[\delta_p - \delta_c + \Delta_e])\tilde{e} + \frac{i}{2}\Omega_e\tilde{c}
\end{aligned} \tag{B.14}$$

with $\Delta_d = \omega_s - \omega_{dc}$,$\Delta_e = \omega_s - \omega_{ec}$, $\Omega_d = \frac{\mu_{dc}}{\hbar}\mathcal{E}_s$,$\Omega_e = \frac{\mu_{ec}}{\hbar}\mathcal{E}_s$. Setting $\tilde{\Gamma}_d = \frac{\Gamma_d}{2} - i(\delta_p - \delta_c + \Delta_d)$, $\tilde{\Gamma}_e = \frac{\Gamma_e}{2} - i(\delta_p - \delta_c + \Delta_e)$, and solving equations (B.14), we find that the system behaves with respect to a weak probe as a a three level EIT scheme with

$$\tilde{\gamma}' = \tilde{\gamma} + \frac{|\Omega_d|^2}{4\tilde{\Gamma}_d} + \frac{|\Omega_e|^2}{4\tilde{\Gamma}_e} \tag{B.15}$$

B.2.3 Interaction of two slow light pulses

A theoretically well known – though experimentally not yet implemented – approach improving the efficiency of the all-optical switch based on the interaction of the $\mathcal{E}_p$ and $\mathcal{E}_s$ fields from Fig. B.2 A has been proposed in [62]. In this approach, the fields $\mathcal{E}_p$ and $\mathcal{E}_s$ have the form of two pulses propagating together, both with group velocity $v_g \ll c$, and the efficiency improvement is conceptually based on the increased atom-photon interaction time.

When a single-photon pulse $\mathcal{E}_p$ propagates in an EIT medium in the form of a polariton, the atomic part of this polariton can interact with a single-photon light pulse $\mathcal{E}_s$ and the overall process basically amounts to a photon-photon interaction. The interaction between the atomic part of the $\mathcal{E}_p$ polariton and the field $\mathcal{E}_s$ is equivalent to an interaction between a single atom and a single photon, and if the pulse $\mathcal{E}_s$ propagates with group velocity $v_{g(s)} = c$, the scattering cross-section for this interaction is σ_{dc}. This cross-section can, however, be increased by increasing the interaction time between the $\mathcal{E}_s$ pulse and the atomic part of the probe pulse polariton as discussed in Section 2.1:

$$\sigma_{eff} = \frac{t_{int}}{\tau_p}\sigma_{dc} \tag{B.16}$$

In the ideal limit of the method described in [62], the group velocities of the two pulses are matched such that $v_{g(s)} = v_{g(p)} \ll c$. This way, the interaction time t_{int} is decoupled from τ_p,

$$t_{int} = \frac{L_{medium}}{v_{g(p)}} \approx OD\frac{\Gamma_a}{|\Omega_c|^2}, \tag{B.17}$$

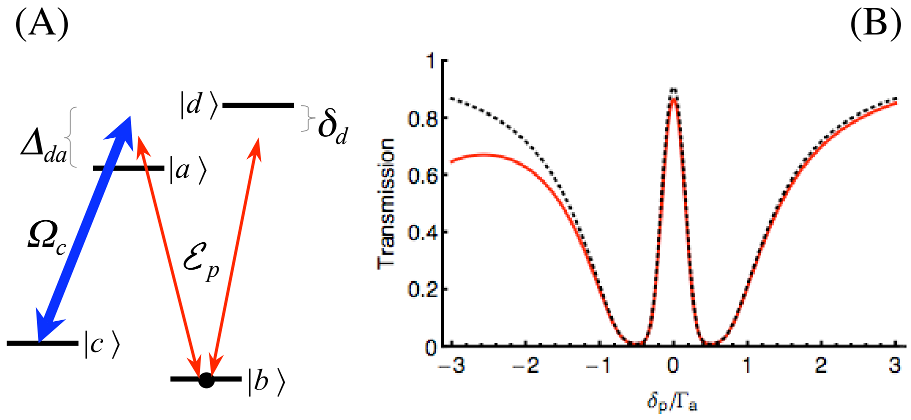

Figure B.4: (A) EIT system in which the probe field only couples to an additional excited state $|d\rangle$. (B) The calculated transmission of such a system for OD $=5$, $\Gamma_a = \Gamma_d$, $\Delta_{da} = -5\Gamma_a$, $\mu_{ab} = \mu_{db}$, and $\Omega_c = \Gamma_a$ (solid red curve). The dotted black curve corresponds to the original EIT system without the effects of the extra atomic level.

and is limited only by width of the EIT transparency window described by equation (2.21), which requires

$$\tau_{pulse} \geq \frac{\Gamma_a}{|\Omega_c|^2}\sqrt{\frac{OD}{\ln 2}}. \tag{B.18}$$

Combining (B.17) and (B.17), we find that in the ideal case the use of two slow light pulses will result in an effective scattering cross-section

$$\sigma_{eff} = \sqrt{OD}\sqrt{\ln 2}\,\sigma_{dc} \tag{B.19}$$

This method can be implemented, for example, by converting $\mathcal{E}_s$ into a slow light polariton in an another EIT system spatially overlapping with the original ensemble of atoms. This will work due to the fact that while most of the energy from the free space light pulse is transferred into the atomic part of the polariton, the peak electric field amplitude of the photonic part of the polariton is equal to the peak electric field amplitude of the single photon pulse in free space.

B.3 Coupling of probe and control fields to additional transitions

Even in the absence of an additional field, the behavior of a real EIT system can significantly vary from that of an idealized three level system due to the coupling of probe and control fields to additional transitions. In the following paragraphs we will

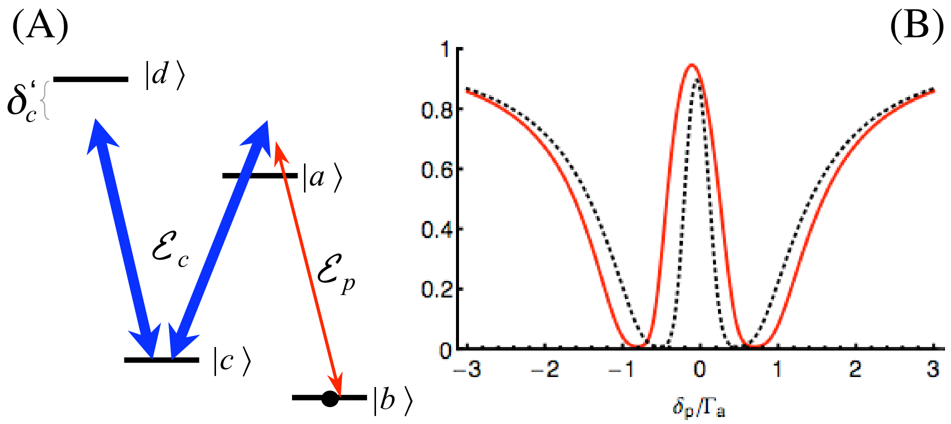

Figure B.5: (A) EIT system in which the control field only couples to an additional excited state $|d\rangle$. (B) The calculated transmission of such a system for OD $= 5$, $\Gamma_a = \Gamma_d$, $\Delta_{da} = 20\Gamma_a$, $\mu_{dc} = 2\mu_{ac}$, and $\Omega_c = \Gamma_a$ (dotted black curve) and $\Omega_c = 1.5\Gamma_a$ (solid red curve).

discuss the basic experimentally relevant scenarios of these additional couplings and their effects. These scenarios include the case of the probe coupling to additional excited states (Fig. B.4 A), the control field coupling off-resonantly to additional excited states (Fig. B.5 A), probe and control field coupling together to more than one excited state (Fig. B.6 A), the control field coupling to the probe transition (Fig. B.6 B), and the probe field coupling $|c\rangle$ to another excited state (Fig. B.6 C).

Coupling of the probe field only to additional excited states will result in additional absorption that cannot be overcome by increasing the intensity of the control field. In the worst case, when $\Delta_{da} \to 0$, this undesired coupling will make the system unsuitable for EIT applications. In less severe cases, when $\Delta_{da} \gg \Gamma_d$, the coupling will lead to a residual absorption scaling as $\sim \text{OD}\left(\frac{\Gamma_d}{\Delta_{da}}\right)^2$, which will place an upper limit on the system's achievable transparency through EIT. In the limit of a weak probe, the system can be quantitatively described with the use of equations (B.1) and (B.2), where for the case shown in Fig. B.4 A in steady state we get

$$\begin{aligned}
\tilde{d} &= i\frac{\mu_{db}}{2\hbar}\frac{1}{\frac{\Gamma_d}{2} - i\delta_d}\mathcal{E}_p = i\frac{\mu_{db}}{2\hbar}\frac{1}{\frac{\Gamma_d}{2} - i(\delta_p - \Delta_{da})}\mathcal{E}_p \\
\tilde{a} &= i\frac{\mu_{ab}}{2\hbar}\frac{\gamma - i[\delta_p - \delta_c]}{(\frac{\Gamma_a}{2} - i\delta_p)(\gamma - i[\delta_p - \delta_c]) + \frac{|\Omega_c|^2}{4}}\mathcal{E}_p \qquad \text{(B.20)}
\end{aligned}$$

An example of a resulting calculated transmission profile, showing a residual absorption of a few percent compared to the original three-level system, can be seen in Fig. B.4 B.

Off-resonant coupling of the control field only to additional excited states (Fig. B.5A)

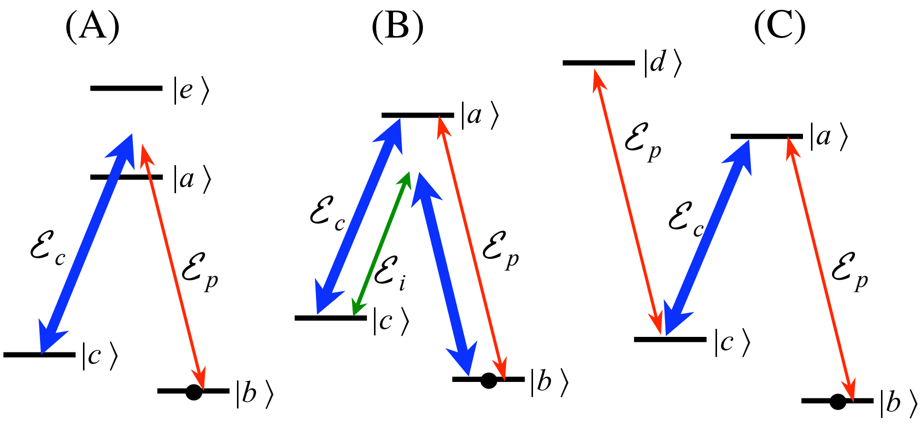

Figure B.6: (A) An EIT system in which the probe and control fields couple to two excited states. (B) An EIT system in which the control field off-resonantly couples to the probe transition, which results in generation of a new field $\mathcal{E}_i$. (C) An EIT system in which the probe field couples to a transition between $|c\rangle$ and another excited state.

will result in a frequency shift of the center of the transparency window with increasing control field intensity (Fig. B.5B). It is essentially the same situation as described in the previous section, except that the control field now plays the role of $\mathcal{E}_s$. Thus the quantitative description of this case is provided by equation (B.5) – or (B.14) if the control field couples to multiple off-resonant levels – with $\Omega_s = \frac{\mu_{dc}}{\hbar}\mathcal{E}_c$. Incidentally, a resonant coupling of the control field to an additional excited state will lead to absorption of the probe just as described in (B.7), which will again make the system not very useful for EIT applications.

The system from Fig. B.6A, in which both probe and control field couple together to more than one excited state, can be described by the following equations of motion

$$\begin{aligned}
\dot{\tilde{a}} &= -\left(\frac{\Gamma_a}{2} - i\delta_p\right)\tilde{a} + \frac{i}{2}\Omega_c\tilde{c} + i\frac{\mu_{ab}}{2\hbar}\mathcal{E}_p b \\
\dot{\tilde{e}} &= -\left(\frac{\Gamma_e}{2} - i[\delta_p - \Delta_{ea}]\right)\tilde{e} + \frac{i}{2}\left(\frac{\mu_{ec}}{\mu_{ac}}\right)\Omega_c\tilde{c} + i\frac{\mu_{eb}}{2\hbar}\mathcal{E}_p b \\
\dot{b} &= i\frac{\mu_{ab}^*}{2\hbar}\mathcal{E}_p^*\tilde{a} + i\frac{\mu_{eb}^*}{2\hbar}\mathcal{E}_p^*\tilde{e} \\
\dot{\tilde{c}} &= -(\gamma - i[\delta_p - \delta_c])\tilde{c} + \frac{i}{2}\Omega_c^*\tilde{a} + \frac{i}{2}\left(\frac{\mu_{ec}^*}{\mu_{ac}^*}\right)\Omega_c^*\tilde{e}
\end{aligned} \tag{B.21}$$

In steady state these lead to a solution

$$\tilde{c} = \frac{-1}{\tilde{\gamma} + \frac{|\Omega_c|^2}{4\tilde{\Gamma}_a} + \left|\frac{\mu_{ec}}{\mu_{ac}}\right|^2 \frac{|\Omega_c|^2}{4\tilde{\Gamma}_e}}\mathcal{E}_p\left(\frac{\mu_{ab}}{2\hbar}\frac{\Omega_c^*}{2\tilde{\Gamma}_a} + \frac{\mu_{eb}}{2\hbar}\frac{\mu_{ec}^*}{\mu_{ac}^*}\frac{\Omega_c^*}{2\tilde{\Gamma}_e}\right)$$

$$\begin{aligned} \tilde{a} &= i\frac{\mu_{ab}}{2\hbar}\frac{\tilde{\gamma}+\frac{|\Omega_c|^2}{4\tilde{\Gamma}_e}\left(\left|\frac{\mu_{ec}}{\mu_{ac}}\right|^2-\frac{\mu_{eb}}{\mu_{ab}}\frac{\mu_{ec}^*}{\mu_{ac}^*}\right)}{\tilde{\gamma}+\frac{|\Omega_c|^2}{4\tilde{\Gamma}_a}+\left|\frac{\mu_{ec}}{\mu_{ac}}\right|^2\frac{|\Omega_c|^2}{4\tilde{\Gamma}_e}}\mathcal{E}_p\frac{1}{\tilde{\Gamma}_a} \qquad \text{(B.22)} \\ \tilde{e} &= i\frac{\mu_{eb}}{2\hbar}\frac{\tilde{\gamma}+\frac{|\Omega_c|^2}{4\tilde{\Gamma}_a}\left(1-\frac{\mu_{ab}}{\mu_{eb}}\frac{\mu_{ec}}{\mu_{ac}}\right)}{\tilde{\gamma}+\frac{|\Omega_c|^2}{4\tilde{\Gamma}_a}+\left|\frac{\mu_{ec}}{\mu_{ac}}\right|^2\frac{|\Omega_c|^2}{4\tilde{\Gamma}_e}}\mathcal{E}_p\frac{1}{\tilde{\Gamma}_e} \end{aligned}$$

with the weak probe propagation governed by:

$$\frac{\partial}{\partial z}\mathcal{E}_p = i\frac{n\hbar}{2}\left(\frac{\Gamma_a\sigma_{ab}}{\mu_{ab}}\tilde{a}+\frac{\Gamma_e\sigma_{eb}}{\mu_{eb}}\tilde{e}\right) \qquad \text{(B.23)}$$

The qualitative effects of this additional coupling depend strongly on the values of the involved transitions' dipole moments and the relative detunings with respect to the two excited states. When the control field is close to resonance with one of the levels, the effect of the additional level will be similar to the case of the control field only coupling to an additional excited state. A more pronounced difference from an idealized three level system's behavior can be expected when the the detunings of the control field from each of the excited states are of the same order of magnitude.

In figure B.6B we can see an EIT system in which the control field couples to the transition between states $|b\rangle$ and $|a\rangle$. This leads to generation of a new field $\mathcal{E}_i$ through a wave-mixing process in which two photons of the control field are absorbed as one photon is emitted into the probe field and one into the field $\mathcal{E}_i$. An experimental observation of this phenomenon, together with a quantitative analysis of it, has been reported in [61]. While this wave-mixing process seemingly improves the transmission of the probe, it is often undesirable as the newly generated probe photons change the statistics of the original probe field. Because of rather large frequency spacing between the two ground states of rubidium, this wave-mixing process, which scales as $\sim \mathrm{OD}\frac{\Gamma_a}{\Delta_{cb}}$, is generally negligible in cold atoms unless OD $\sim$ 1000. On the other hand, for room temperature rubidium vapor, the onset of the wave-mixing can be observed already for OD < 10 due to Doppler broadening of the excited state. Suppression of this process can be achieved, at least theoretically, by preparing the atoms in a single Zeeman sublevel of the ground state and by choosing an appropriate combination of control and probe field polarizations.

Finally, EIT systems in which the probe field couples also to a transition between $|c\rangle$ and an additional excited state $|d\rangle$ have been the subject of several recent theoretical works exploring strongly correlated quantum systems and interactions between single photons [19, 40, 53]. A quick semi-classical calculation reveals that the propagation of the probe field in such system has roughly the form of

$$\frac{\partial}{\partial z}\mathcal{E}_p \sim -OD\frac{\gamma\Gamma_a}{|\Omega_c|^2}\mathcal{E}_p - \frac{OD}{|\Omega_c|^2}\mathcal{E}_p^3. \qquad \text{(B.24)}$$

The second term on the right side suggests that the transmission of the system can be affected by the intensity of the incoming probe field. As a result, the system has

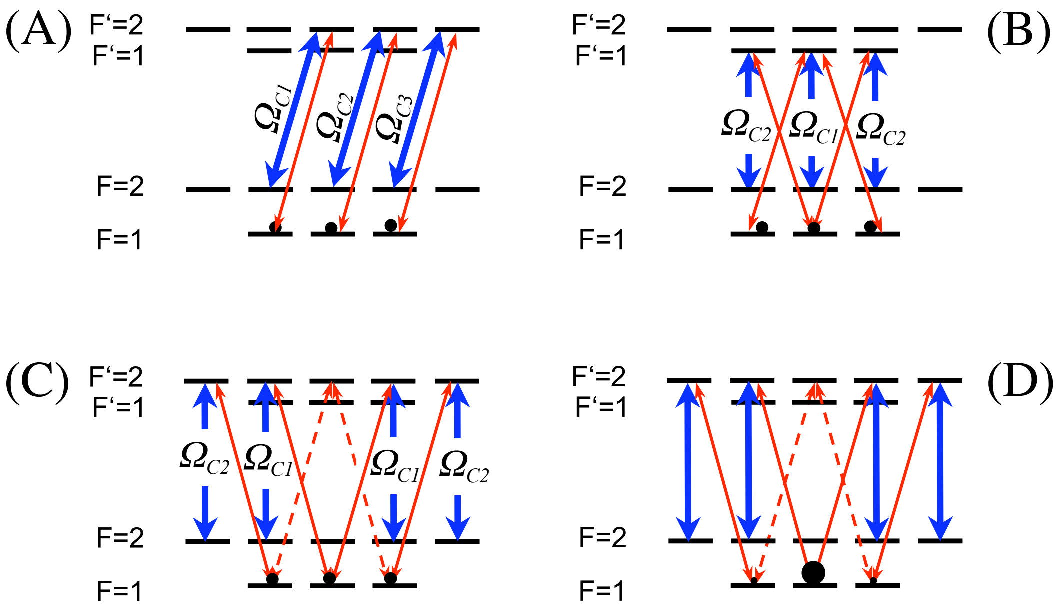

Figure B.7: EIT schemes on D_1 line of rubidium^{87} used in this work. (A) Both probe and control field have the same circular polarization. (B) Probe and control field are both polarized linearly, but perpendicular to each other – so called lin⊥lin scheme. In the atom's frame of reference, the control field is π-polarized, while the probe gets decomposed into σ^+ and σ^- light. (C) A lin⊥lin scheme where $F' = 2$ is used as the excited state. The dashed lines show the probe coupling to excited states that are not part of an EIT system, which leads to probe absorption. (D) The undesired absorption can be prevented by emptying the $m_F = \pm 1$ levels, for example by optically pumping the atoms into the $m_F = 0$ Zeeman sublevel.

the potential to controllably change the photon statistics of the probe field when the atoms and the photons are tightly confined inside a hollow photonic waveguide. This property can be additionally enhanced through the use of the stationary light pulse techniques discussed in Chapter 3. Unfortunately, the experimental realization of such system, in which the coupling between levels $|c\rangle$ and $|d\rangle$ provided by the probe field is either resonant or at least not too far off-resonant, has so far been a bit of a challenge.

B.4 EIT and rubidium^{87}

When implementing EIT in an ensemble of rubidium^{87}atoms, one needs to translate the idealized three-level system of Fig. 2.2 into the harsh experimental reality of the atomic-level structure shown in Fig. A.1. In particular, the frequency and polarization choice for both probe field and control field will determine which m_F sublevels of the two ground states will couple to which $m_{F'}$ sublevels of the excited states. This will determine the optical depth of the atomic ensemble as well as its maximum transparency achievable under EIT conditions.

The trade-offs start already when choosing between implementing EIT on the D_1 versus the D_2 line. The excited states of the D_1 line are spaced further apart in frequency and there are fewer of them compared to the D_2 line. As a result, there is less of the unwanted off-resonant coupling of probe and control fields to the additional excited states for the D_1 line, which is makes it a cleaner system to work with. On the other hand, stronger optical transitions can be found on the D_2 line compared to the D_1 line, which means that the optical depth available on D_2 will be larger given the same number of atoms.

Figures B.7 and B.8 A show the resonant coupling paths between the ground and excited states for the frequency-polarization schemes used to implement EIT in this work. Unless declared otherwise, these schemes assume an equal fraction of atoms to be in all the sublevels of the ground state of the probe transition. Consequently, the atomic ensemble behaves as a mixture of several EIT systems, with each system's behavior determined by the scattering cross-section on the probe transition $\sigma_{a_i b_i}$, Rabi frequency of the control field Ω_{ci}, and coupling of probe and control fields to additional levels.

Figure B.7A corresponds to the polarization scheme used in the experiments described in Chapter 3. For the experiments described in Chapter 5, we had to come up with an EIT scheme that would work with linearly polarized probe and control fields, due to the birefringence of the fiber. These experiments are performed in the scheme shown in Fig. B.7B. The disadvantage of this arrangement is that for the D_1 line the optical depth on the $F = 1 \rightarrow F' = 1$ transition is about five times smaller than it would be on the $F = 1 \rightarrow F' = 2$ transition for the same number of atoms. Unfortunately, the lin$\perp$lin EIT scheme with probe coupled to the $F = 1 \rightarrow F' = 2$ transition will suffer from absorption of the probe due to its coupling to the $|F' = 2, m_{F'} = 0\rangle$ state (Fig. B.7C) and similar problem would be encountered for a lin$||$lin scheme. We attempted to suppress this absorption by optically pumping the atoms into the $|F = 1, m_F = 0\rangle$ state (Fig. B.7D). Unfortunately, due to the $\sim 85\%$ efficiency of the pumping we could achieve, the atoms left in the $|F = 1, m_F = \pm 1\rangle$ states still caused a significant probe loss, in particular at higher (> 10) overall OD.

Lastly, figure B.8A shows the coupling of atomic levels for EIT we implemented on the D_2 line. At 780nm, we were only able to couple light of one linear polarization into the PCF piece in our setup, most likely due to the fact that this wavelength is at the edge of the guiding range of this fiber (Fig. 4.1). The lin$||$lin scheme shown here allowed us to observe EIT in the hollow core PCF also on the D_2 line and made the larger optical depth of this line accessible for NLO experiments in our setup (Fig. B.8B). A minor disadvantage of this arrangement is that it makes separation of probe and control photons more difficult, since polarization filtering cannot be used.

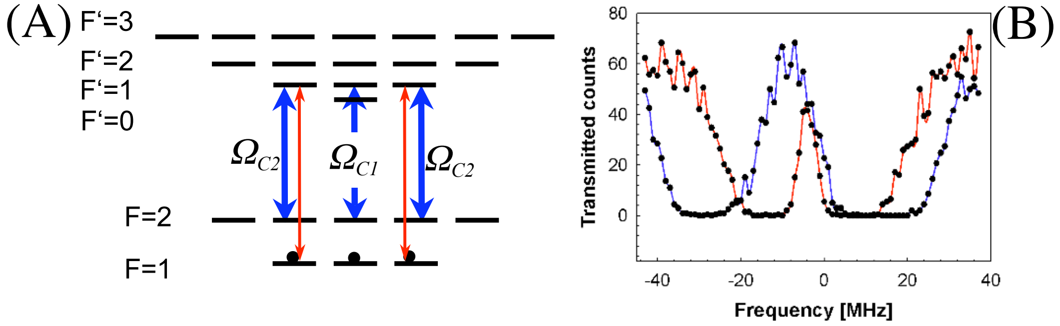

Figure B.8: EIT on D_2 line of rubidium^{87}. (A) Both probe and control field have the same linear polarization – so called lin||lin scheme. (B) Experimental observation of EIT with this scheme inside the hollow core PCF with $OD \approx 40$ for two different control field powers. Note the shift of the EIT peak center resulting from the control field coupling off-resonantly to the $F' = 2$ and $F' = 3$ levels and the onset of absorption from the $F' = 0$ level.

B.5 Doppler broadening

Consider a two-level atom moving with velocity $\vec{v} = (v_x, v_y, v_z)$ interacting with weak light of frequency ν and electric field amplitude $\mathcal{E}_p$ propagating in the z-direction, as described at the end of section 2.1 by equations of motion (2.7). For the general case of $\nu - \omega_{ab} = \delta$, the atom will observe the field detuning from its transition to be $\delta' \approx \delta - kv_z$, where $k = \frac{\nu}{c}$ is the magnitude of the wave vector of the light. In steady state, we can write for the excited state coefficient $\tilde{a}$ from (2.7)

$$\tilde{a}(\delta, v_z) = i\frac{\mu_{ab}\mathcal{E}_p}{2\hbar}\frac{1}{\frac{\Gamma}{2} - i(\delta - kv_z)} \tag{B.25}$$

For an atomic ensemble with temperature T, the probability density function of v_z is given by the Maxwell-Boltzmann distribution, $f_{v_z} = \sqrt{\frac{m}{2\pi k_B T}} exp\left(-\frac{mv_z^2}{2k_B T}\right)$. Therefore, in such an ensemble

$$\tilde{a}(\delta) = i\frac{\mu_{ab}\mathcal{E}_p}{2\hbar}\sqrt{\frac{m}{2\pi k_B T}}\int_{-\infty}^{+\infty}\frac{e^{-\frac{mv_z^2}{2k_B T}}}{\frac{\Gamma}{2} - i(\delta - kv_z)}dv_z \tag{B.26}$$

Carrying out the integration in (B.26), we obtain

$$\tilde{a}(\delta) = i\frac{\mu_{ab}\mathcal{E}_p}{2\hbar}\frac{\sqrt{\pi}}{k}\sqrt{\frac{m}{2k_B T}} exp\left[\frac{m}{2k_B k^2 T}\left(\frac{\Gamma}{2} - i\delta\right)^2\right]\left(1 + i\text{Erfi}\left[i\sqrt{\frac{m}{2k_B k^2 T}}\left(\frac{\Gamma}{2} - i\delta\right)\right]\right) \tag{B.27}$$

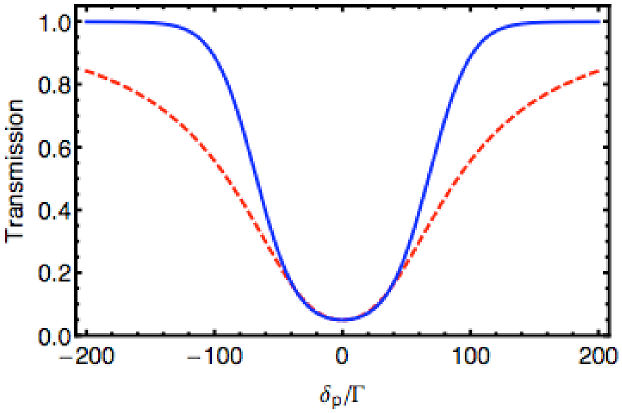

Figure B.9: Calculated transmission of a weak probe through an ensemble of two level Doppler broadened atoms. The solid blue curve is based on equation (B.27), while the dashed red curve corresponds to the approximation (B.28).

where "Erfi" denotes the imaginary error function. For $\sqrt{\frac{m}{2k_B k^2 T}}\left(\frac{\Gamma}{2} - i\delta\right) \ll 1$, (B.27) can be approximated as

$$\tilde{a}(\delta) \approx i\frac{\mu_{ab}\mathcal{E}_p}{2\hbar}\frac{\pi}{2}\frac{1}{\frac{\sqrt{\pi}}{2}\sqrt{\frac{m}{2k_B k^2 T}} + \frac{\Gamma}{2} - i\delta}, \tag{B.28}$$

which leads to equations (2.8) and (2.9). The full treatment from (B.27) is compared to the (B.28) approximation in Fig. B.9 for an ensemble of rubidium^{87} atoms with $OD \approx 3$, $\Gamma/2\pi = 6$ MHz, and $T = 360$K.

On the other hand, an EIT system, which consists of an ensemble of Doppler broadened three-level atoms, cannot analytically be described beyond the approximation (2.26). Thus to make more precise quantitative predictions, in particular for large detuning of the control field, one needs to numerically integrate equation (2.25).

Appendix C

EIT-based wave guide

We show that EIT combined with the Gaussian profile of the control beam can be used for focusing and guiding of weak probe light. In particular, we demonstrate waveguiding of propagating light beams in optically dense media. We also observe evidence of transverse localization of stationary pulses of light. We demonstrate transverse confinement of a stationary light pulse based on radial variation of refractive index of warm rubidium vapor in a Λ-scheme EIT setup.

To achieve these non-linear interactions between pulses with limited numbers of photons, one needs to achieve a combination of large optical non-linearity, high electric field intensity per photon, and long interaction times, while maintaining low photon loss. An atomic ensemble under EIT conditions [82] has low absorption and large nonlinearities that can be easily controlled. At the same time pulses propagate through the ensemble at ultra-low group velocities allowing for long interaction times. In Ref. [8], the authors showed a novel method of increasing the interaction time between light and atoms by creating a stationary light pulse inside atomic media with EIT. Using this technique, one can dynamically control the group velocity of the pulse without affecting the field intensity of the manipulated light pulse. Since this technique is based on a passive medium, the quantum state of the manipulated pulse should be preserved. Consequently, if the stationary pulse were sufficiently transversely confined, the resulting simultaneous increase of the interaction time and of the field intensity per photon could enable coherent, controlled nonlinear processes at optical energies corresponding to single light quantum as proposed e.g. in Ref. [3]. One possible technique for this would be placing the atoms iside a hollow core photonic crystal fiber as demonstrated in [38]. In this work we used the transverse variation in refractive index caused by the Gaussian profile of the control field in [8] to create a transverse confinement for the stationary light pulse.

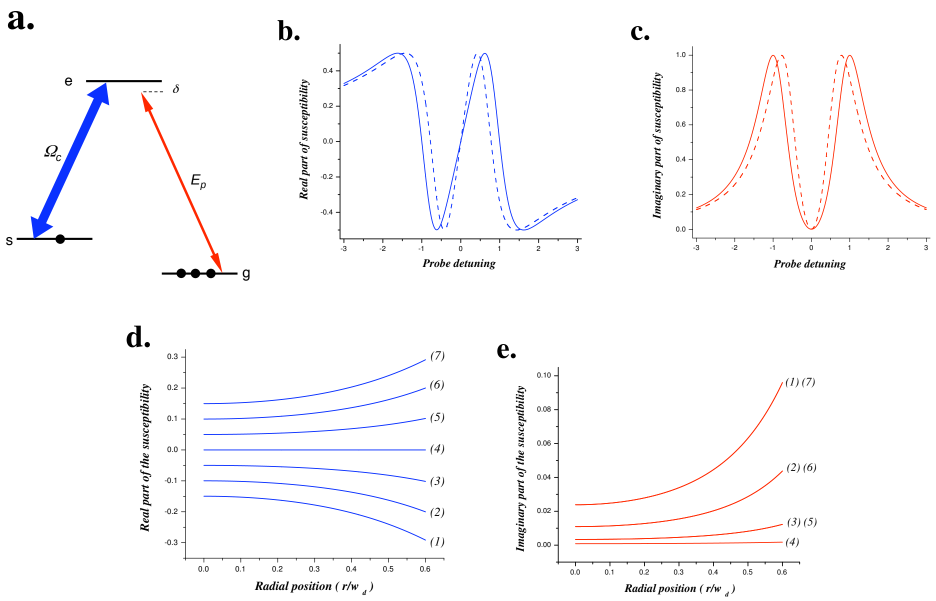

Figure C.1: (a) Idealized Λ atom illuminated by control field with Rabi frequency Ω_c and probe field E_p. The real (b) and imaginary (c) part of the susceptibility as a function of probe detuning δ at the center of the beam, $r = 0$(solid line), and at $r = \frac{w_d}{2}$(dotted line). The real (d) and imaginary (e) part of the medium susceptibility are plotted against radial position with respect to the center of the control beam for several probe detunings. Curves (1) to (7) in both plots correspond to probe detunings of -0.15Γ, -0.1Γ, -0.05Γ, 0, $+0.05\Gamma$, $+0.1\Gamma$, and $+0.15\Gamma$, respectively. All plots are in units of $N|\mu_{eg}|^2(2\pi\Omega_0\epsilon_0\hbar)^{-2}$ where $\Omega_0 = \Gamma$ is the Rabi frequency of the control field in the center of the beam.

C.1 Qualitative picture

Fig. C.1a shows an idealized three level atom interacting with two fields — a control field (Rabi frequency Ω_c) coupled to the transition $|s\rangle \Leftrightarrow |e\rangle$ and a probe field E_p coupled to $|g\rangle \Leftrightarrow |e\rangle$. We assume that the population of the excited state decays equally into each of the states $|g\rangle$ and $|s\rangle$ with rate Γ and the coherence between states $|g\rangle$ and $|s\rangle$ decays at a rate γ_{gs}. When the difference between the probe and drive frequency is close to the splitting between g and s, the otherwise opaque medium will become transparent for the probe in a frequency range $\delta \sim \Omega_C^2/\sqrt{N} \times \sqrt{\gamma_{gs}/\Gamma}$ [61] (N being the atomic density). In Ref. [8] a stationary light pulse was created by applying two control fields propagating in opposite directions to an atomic medium in which a light pulse was stored. The spatial modulation of the medium's susceptibility – resulting from the standing wave control field – works like a Brag grating which captures the retrieved probe pulse in the atomic vapor. To release the trapped probe pulse one may turn off one of the control fields hence erasing the periodic spatial modulation of the medium's susceptibility. The transverse variation of the control field intensity can significantly affect the diameter of the probe beam in an EIT experiment [66, 67]. Since the width of the EIT resonance depends on the intensity of the control field, the absorptive and refractive properties of the medium will vary with the distance from the control beam axis for a given two-photon detuning. More specifically, for small negative two-photon detuning the index of refraction experienced by the probe light will be higher in the center of the control beam than at its edge (Fig. C.1b), while for small positive two-photon detuning the index of refraction will be higher at the edge than in the center of the control beam. At the same time for both small positive and negative detuning the absorption of the probe will increase with distance from the center (Fig C.1c). Therefore a thin slice of the medium works as a combination of a thin (focusing or defocusing) lens and a soft-edged aperture. This spatial variation in susceptibility may reshape the probe beam. We are interested in the beam confinement which is achieved through negative two-photon detuning. In this case the transverse localization of the probe field is, in the ideal limit, achieved purely through spatial variation of the refractive index and is almost without optical loss. Before we proceed, it is worth noting that the mechanism transversely confining the probe field due to variation of the refractive index takes place only in the presence of the control field. Consequently, if a pulse was initially stored in a small diameter volume in warm vapor, the diameter of the volume from which the pulse will be retrieved when the control field is applied again is determined by the spread of the atoms from their initial position due to thermal motion (if unrestricted, atoms at $\sim 70\,^\circ$C travel ~ 0.25 mm in 1 μs). Therefore, to maximize the transverse confinement of a stationary pulse, the storage time should be kept as short as possible.

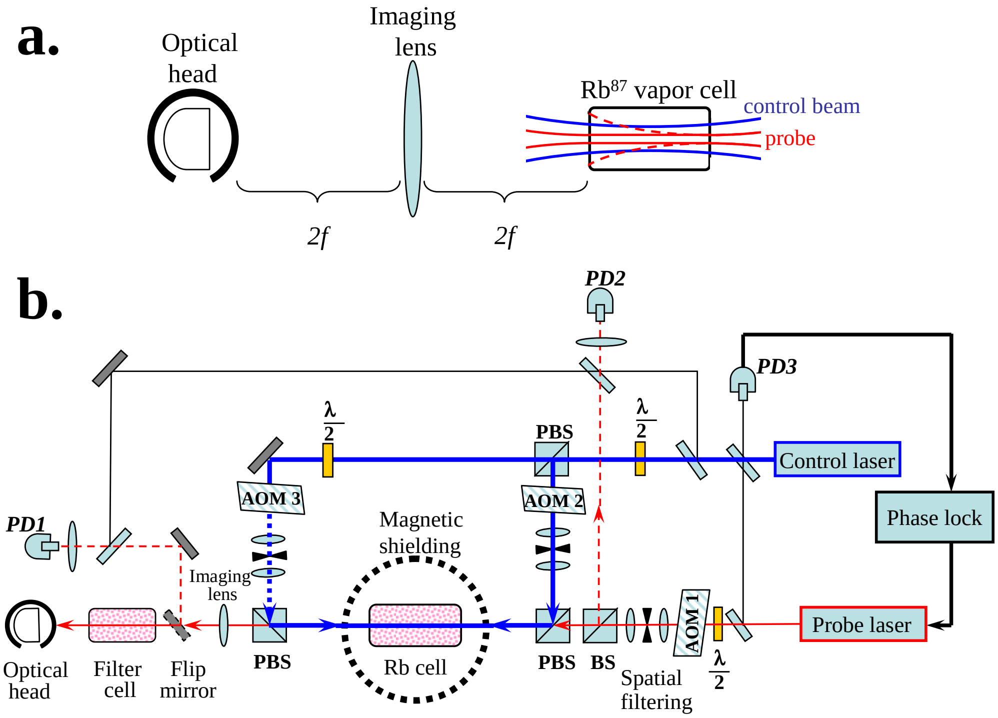

Figure C.2: (a) Schematics of the measurement of the probe beam diameter. (b) Experimental setup. PBS and BS denote polarizing and non-polarizing beam splitters, respectively; AOM labels for acousto-optic modulators ; PD1, PD2, and PD3 are fast photodiodes. The flip mirror can route probe detection between the optical head and the PD1.

C.2 Experimental setup

Our experimental apparatus is shown in Fig. C.2. We approximated the Λ-system from Fig.C.1a by tuning a frequency of the extended cavity diode laser to the $F = 2 \rightarrow F^{'} = 2$ transition of the rubidium $D1$ line (control field) while probe laser frequency is tuned to the $F = 1 \rightarrow F^{'} = 2$ transition (probe field). The frequency of the control field was monitored via saturation spectroscopy on a separate cell. The frequency of the probe laser was phase-locked to the control laser. We used 80 MHz acousto-optic modulators (AOM) as shutters to pulse the laser beams. To achieve clean Gaussian profiles we spatially filtered the beams by focusing them through pinholes. A magnetically shielded 5 cm long ^{87}Rb vapor cell with no buffer gas was maintained at temperature $T \approx 72°C$ (atom number density is $10^{12}\,\mathrm{cm}^{-3}$). The probe and control beams were co-propagating and orthogonally polarized. We first studied the guiding effects associated with EIT in the continuous wave regime by measuring the diameter of the probe beam at the exit of the cell for various two-photon detunings. This was done through imaging the exit plane of the cell onto the optical head of a Thorlabs beam size meter (Fig 2a) after the control beam was filtered out by passing the overlapped beams through a polarizing beam splitter and a filtering cell containing warm ^{85}Rb vapor. We focused a 60 μm probe beam to 200 μm waist at the cell entrance. When the probe was tuned far above the resonance and drive was not present, the probe diameter expanded to 400 μm at the exit face of the cell. A 1.1 mW control beam was collimated to 1.1 mm to keep its diameter approximately constant over the length of the cell (Fig. C.2a). During the measurement the frequency of the control laser was fixed while the frequency of the probe laser was changed in discrete increments. For each frequency point we measured the transmission and beam diameter at the exit face of the cell. The probe power used was the smallest value at which we were still able to measure the beam diameter as a function of two-photon detuning over the whole width of the EIT window. At the same time, we were trying to limit the power in the control field in order to secure low group velocities for the pulsed experiments.

C.3 CW experiment

A typically observed dependence of transmission and exiting probe beam diameter on the two-photon detuning is shown in Fig. C.3. Similar results, scaled by the larger width of the transparency window, were achieved for increased powers in the control beam. Right on two-photon resonance the probe transmission is maximum. As the two-photon detuning increases in the negative direction, we initially observe a steep decrease in the diameter of the exiting probe while the probe transmission does not change significantly. At the same time, when the two-photon detuning increases from zero in the positive direction, the slow change of beam diameter is accompanied by a steep decrease in transmission. We would like to point out the notable asymmetry in the shape of the transmission caused by the transverse variation in the refractive index. For negative two-photon detuning the refractive index profile confines the probe in the region of high control field and low absorption. For positive two-photon detuning the defocusing refractive index profile pushes the probe out of the center into regions with lower intensity of the control field, thus increasing the probe absorption. The appearance of beam confinement observed for positive two-photon detuning is then of purely absorptive origin. Note that the temperature of the cell is about 20 °C lower than the temperature at which the cell was kept in the original stationary pulse experiment [8] and also that the cell contains no buffer gas. This was done to suppress the four-wave mixing effect which occurs when the control field couples into the $F = 1 \rightarrow F' = 2$ transition [61] in an effort to keep the focus of the experiment on the transverse variation of the refractive index and to avoid effects caused by a transversely varying gain for the probe. These changes however come at a price: the lower atomic number density resulting from lower temperature leads to

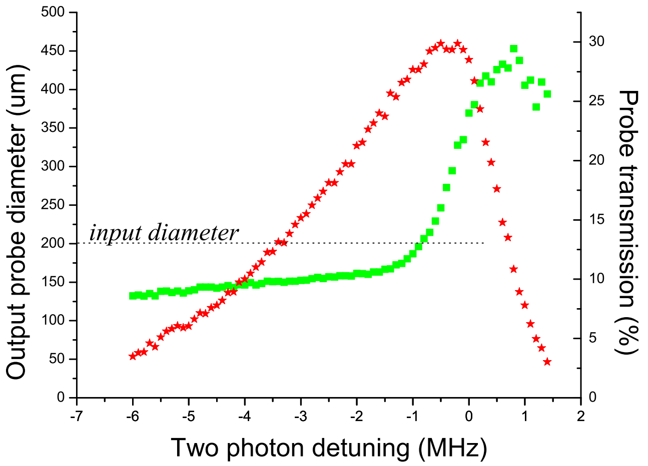

Figure C.3: Beam diameter (squares) at the cell exit and the CW probe transmission (stars) vs the two-photon detuning

higher probe group velocity and lower reflectivity of the Bragg grating created by the standing wave control field, while the absence of buffer gas together with the small probe beam diameter decrease the coherence time τ_{gs}. We therefore expect overall worsening of the conditions for stationary pulse observation. A flip mirror allowed us to send the light coming out of the cell to a second detection setup. Here, the light was mixed with a reference beam taken from the control laser on a fast photodiode and we measured the $\sim$ 6.8 GHz beat with a spectrum analyzer set to zero span. This also allowed us to distinguish the probe light from the new field generated via the four-wave mixing process [61]. We observed the power in the new field to be less than $\sim 1\%$ of the power of the transmitted probe and concluded that its effect on the beam confinement should be negligible.

C.4 Pulsed experiment

Using the same detection setup we proceeded to study the behavior of a stationary pulse under these probe-confining conditions. Since we were not able to measure directly the probe beam diameter in the pulsed regime, we instead compared amplitudes of pulses with two-photon detunings of equal magnitude but opposite sign. The underlying assumption was based on the asymmetry of the transmission curve observed in the c.w. experiments, i. e. when the probe confinement results from refractive index variation (negative detuning), the pulse should experience less absorption and its amplitude should be bigger than when the detuning is positive and any probe confinement is of purely absorptive origin. The red dotted curve in Fig.

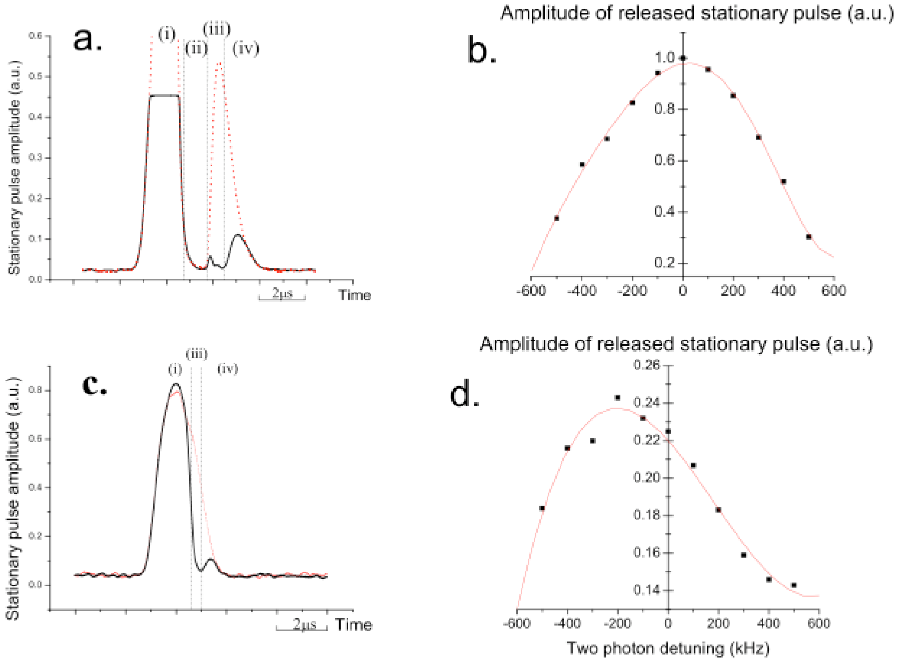

Figure C.4: (a), (c) Stationary light pulse with different storage time (zone (ii): $\tau = 0$ μs and $\tau = 1$ μs). and the amplitude of the released stationary pulse as a function of probe frequency detuning, correspondingly (b) and (d).

C.4a shows the observation of an ordinary storage and retrieval experiment: the left peak represents the fraction of the pulse that escaped the cell before the trapping has begun, while the right peak is the stored and retrieved part of the pulse – it appears only after the forward control is turned on again. The solid black line in Fig. C.4a shows a typical observed signal obtained by following the stationary pulse creation procedure outlined in [8] with the pulse stored in the atomic coherence for 1 μs. The control beam diameter and power are the same as in the CW part. The roman numerals mark time zones with different control field configurations: (i) only forward control beam that co-propagates with the probe is present (writing stage); (ii) all control beams are off (storage stage); (iii) the forward control beam is turned on together with a counter-propagating backward control beam of the same diameter and power (retrieval and trapping); (iv) the backward control field is turned off (release). As in [8], the probe escape from the cell is suppressed for the duration of (iii) (~ 0.5 μs) which is followed by a pulse released after the backward control is turned off (iv). Fig. C.4b plots the magnitude of the released pulse against the detuning of the probe. The plot is fairly symmetric with respect to the zero detuning, which suggests the absence of refractive index based confinement of the stationary pulse. This was to be expected since (as mentioned earlier) the initial confinement is lost during the storage stage due to thermal motion of the atoms in the absence of the control beam. To counteract this we modified the original stationary pulse creation procedure by skipping the storage stage (zone ii) and instead just turning on the backward control beam while the pulse is still propagating through the medium (the forward control beam is kept CW). The experimental observation resulting from this altered procedure can be seen as a solid red line in Fig. C.4c (the black dotted line corresponds to pulse propagation in the presence of the forward control beam only). The roman numerals mark (i) the presence of the forward control beam only; (iii) the backward beam is turned on after the rear edge of the pulse has entered the cell (trapping); (iv) the backward control beam is turned off again (release). The first peak again represents the fraction of the pulse that escapes the cell before the backward beam is turned on and the standing wave starts trapping the pulse. During the time of (ii) (~ 0.5 μs) the escape of the probe light from the cell is suppressed. This is then followed by a released pulse when the backward beam is turned off again (iv). The magnitude of this released pulse is plotted against the probe detuning in Fig. C.4d. Here the amplitude of the released pulse decreases faster with increasing positive detuning than for increasing negative two photon detuning. This behavior qualitatively follows the transmission asymmetry observed in the CW experiment (Fig. C.3) which suggests that for negative probe detuning the stationary pulse is indeed transversely confined through radial variation of the refractive index.

C.5 Summary

In conclusion, we observed refractive index based probe beam confinement in an atomic medium under Λ-scheme EIT conditions with negative probe detuning. This originated from transverse variation in the intensity of the control field as predicted and was complemented by a notable asymmetry of the transmission resonance resulting from the overall radial dependence of the susceptibility. Furthermore, we created stationary light pulses under probe confining experimental conditions and observed an indirect signature of a transversely confined stationary light pulse. Despite obvious limitation of this technique in warm atomic vapor this experiment provides a demonstration of tight three-dimensional confinement of light pulses with non-vanishing photonic component. The mechanisms behind both the transverse and the longitudinal confinement of the light pulse are based on a passive medium and in the ideal limit are not accompanied by optical loss or gain. We therefore anticipate that this technique can be used to tightly confine single photons in all three dimensions while preserving their quantum state. Finally it is worth noting that the demonstrated effects were achieved with a control beam with diameter significantly larger than that of the probe. This implies that the confocal parameter of the control beam is not a limiting factor for the distance over which the probe can be confined. Consequently, the techniques described here might also prove useful for probing cold atomic ensembles with extremely large aspect ratios, such those demonstrated in Ref. [90].

Appendix D

Technical appendices to Chapter 4

D.1 Vacuum system

The vacuum system is centered around a custom designed welded vacuum chamber manufactured by Nor-Cal. The chamber has ten viewports (windows) and an electropolished inner surface. The rest of the vacuum tubing parts as well as the viewports are off-the-shelf, mostly manufactured by Nor-Cal and MDC. Additionally, the viewports have antireflection coatings (by Spectrum Thin Films) for the rubidium wavelengths. The chamber, together with the rest of the vacuum system, is bolted to a $30'' \times 60''$, $\sim 2''$ thick Newport honeycomb structure breadboard. The bolting structure was custom designed with the goal of minimizing the possibility of uneven stresses on the copper gaskets sealing the joints between parts. The breadboard with the vacuum system sits on an optics table and is cushioned by four $4''$-diameter, $1''$-thick sorbothane pads for vibration isolation.

All vacuum parts were cleaned in an ultrasonic bath before we assembled them. The large parts were cleaned by the manufacturer[1], while the cleaning of the smaller parts (e.g. PCF holding assembly) was done in-house. We used a four step ultrasonic cleaning procedure consisting of baths in soap water, distilled water, acetone and ethanol, taking 15 minutes each.

The vacuum is maintained by a 20 litres/sec ion pump (VacIon 20 Plus by Varian) controlled by a MidiVac controller and titanium sublimation pump based on a section of the vacuum system coated with titanium using a Varian TSP filament operated by Varian 929022 filament controller (fresh titanium coating is applied about once a year). A naked ion gauge (Varian 24p) operated by Terranova 934 controller from Duniway can be used to check the vacuum inside the chamber. The system is pumped down with a turbo pump backed by a roughing oil pump, which achieves pressure of $\sim 10^{-5}$ Torr, and then baked out for seven days with the running turbo pump

---

[1] Though some of the non-electropolished tubing required additional acetone and ethanol scrubbing with clean room wipes.

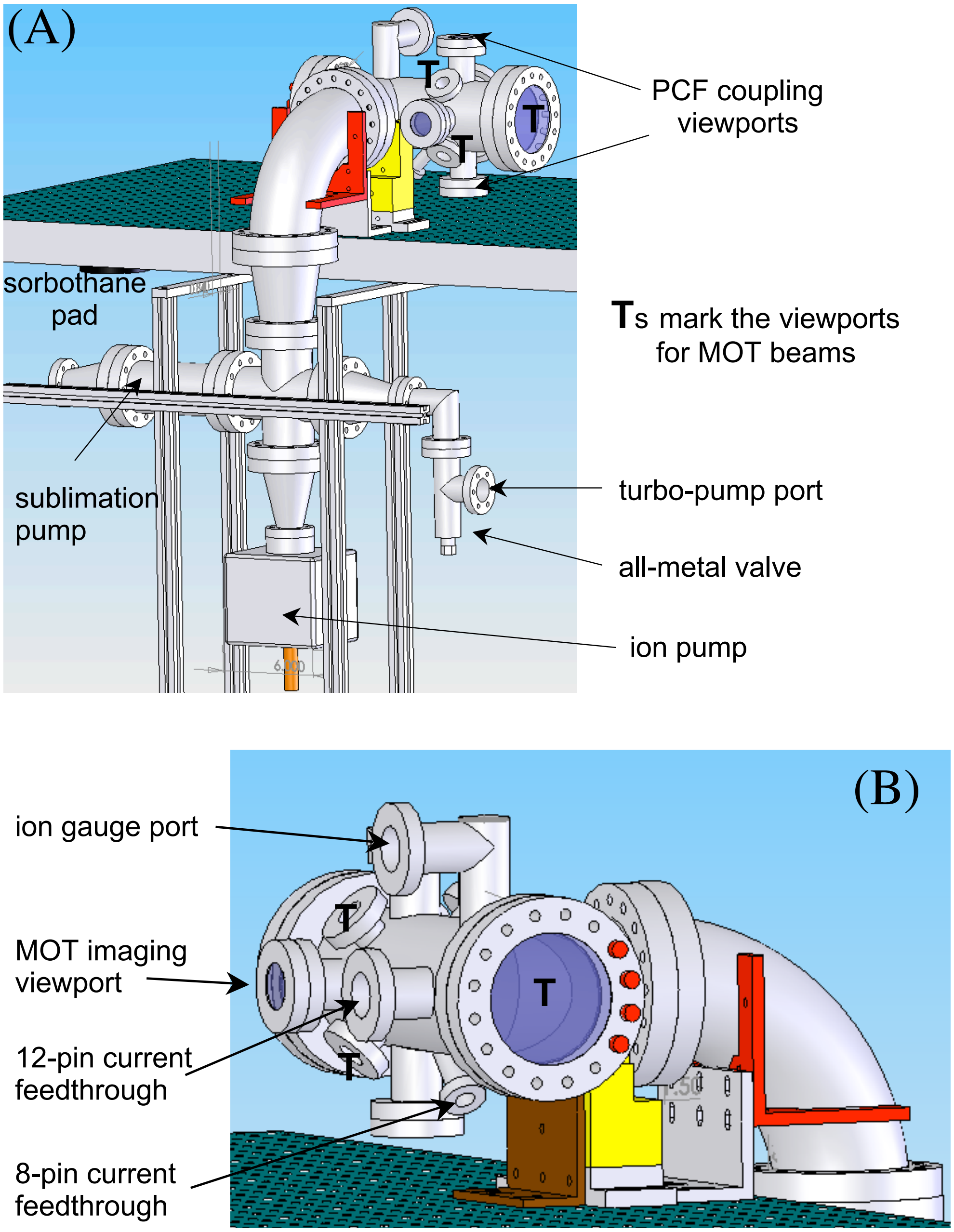

Figure D.1: (A) The overall vacuum system. (B) The vacuum chamber.

attached to the system. After the system is cooled down the ion pump is engaged. The bakeout was performed by heating tapes (by Omega) covered with aluminum foil.[2] We used several sections of the heating tape, with each section controlled by a separate variac to maintain an even temperature over the vacuum system. The first bakeout was done with the vacuum system assembled completely but without the fiber holding assembly. The maximum temperature during this bakeout was $\sim 200\,^\circ\mathrm{C}$ limited by the glass-metal seals on the viewports. The second bakeout was performed with the fiber assembly inside the chamber and the maximum temperature was limited to $\sim 150\,^\circ\mathrm{C}$. This lower limit was given by the temperature tolerance of the Kapton isolation of the wiring and of the epoxy (EPO-TEK 353ND purchased from Thorlabs) used in the fiber assembly. After the chamber cooled off, the pressure stabilized at $\sim 10^{-9}$ Torr. Note that after the bakeout procedure, the all metal valve is closed and the turbo pump is disconnected from the system.

D.2 Current carrying structures

Our experimental system contains multiple current carrying structures, both inside and outside of the vacuum. These include the main MOT coils (in vacuum), three pairs of bias coils (outside vacuum), a small shift coil (in vacuum), and a magnetic funnel. Additional details of the design and construction for these structures as well as for the current controllers can be found in [22]. Note that all wire used inside the vacuum chamber was purchased from Allectra and has UHV compatible Kapton isolation. The current into the vacuum chamber is supplied by two feedthroughs – a small one with 8 Kovar pins (up to 7A/pin, from MDC) and a bigger one with 12 copper pins (up to 30A/pin, from Kurt Lesker). In-vacuum connections between wires are provided either by UHV in-line Be/Cu barrel connectors (by Kurt Lesker) or by ultrasonically cleaned stainless steel eurostrips from which the plastic has been stripped. The feedthroughs are connected to a fan-out ring inside the chamber. This ring is then connected to the current carrying structures of the fiber assembly, with the wires marked by colored ceramic beads. The map of the in-vacuum electrical connections can be seen in Fig. D.2.

D.3 Laser systems

The laser systems used in our experiments are all based on laser diodes with stabilized current and temperature. Most of them are purchased from Toptica, Sacher, and VVV, while a few were constructed in-house. Groups of lasers and their infrastructure are located on separate breadboards and light is brought over to the main experimental breadboard via single mode polarization maintaining fiber patches (mostly from

---

[2] We were careful to avoid crossing of the heating tape.

Fanout connector	Bead color	Component	Feedthroogh	Connector
1	green	F4 - funnel wire right back (top)	small	8
2	blue	F3 - funnel wire left back (top)	small	4
3	brown	F2 - funnel wire left front (top)	small	1
4	gray	F1 - funnel wire right front (top)	small	7
5	blue blue	F3 - funnel wire left back (bottom)	small	3
6	gray gray	F1 - funnel wire right front (bottom)	small	2
7	brown brown	F2 - funnel wire left front (bottom)	small	5
8	green green	F4 - funnel wire right back (bottom)	small	6
9	black black	small coil (bottom wire)	big	3
10	black	small coil (top wire)	big	2
11	--		big	1
12	gray green	back MOT (top layer)	big	11
13	lost bead	back MOT (bottom layer)	big	9
14	green	Rb getter left back	big	7
15	blue	Rb getter left front	big	6
16	blue white	front MOT (bottom wire)	big	12
17	lost bead	front mot (top wire)	big	5
18	gray	Rb getter right back	big	8
19	brown	Rb getter right front	big	10
20	black	Rb getters gnd	big	4

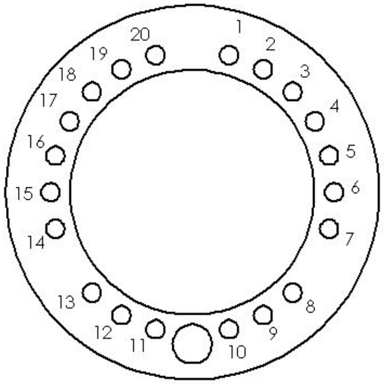

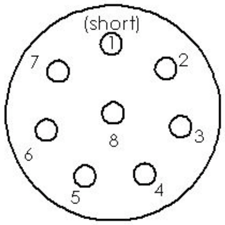

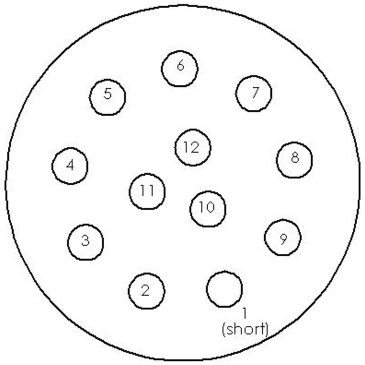

MOT coils: (looking at the front)
front MOT coil: bottom →(ccw) → top
back MOT coil: bottom →(cw) → top

Small Coil: (looking from top down)
bottom→(ccw)→ top

Note: position of getters and funnel wires (left vs right) is determined by looking from back to front

cw = clock-wise, ccw = counter-clock-wise, front = closer to the lab door

Figure D.2: The map of the in-vacuum electrical connections for the 8-pin and 12-pin current feedthroughs, and the fan-out ring.

OZ Optics). This way, a component realignment on the laser boards does not affect the experiment and vice versa. Additionally, this layout makes it possible to move the experiment (should the need arise) without having to disassemble it completely.

D.3.1 D$_2$ line lasers

These lasers are used for trapping and cooling of the rubidium atoms, and can also be used for probing atoms inside the fiber. An extended cavity diode laser (by VVV) serving as a reference laser is stabilized to a particular frequency within the D_2 line [17] using a DAVLL scheme [24]. Additional lasers tuned to the D_2 line are stabilized via a frequency offset lock through a feedback system whose details are described in [17, 22]. These lasers include the MOT repumper tuned to the $F = 1 \rightarrow F' = 2$ transition (Sacher Cheetah system based on a DFB laser diode), the main MOT trapping and cooling laser tuned near the $F = 2 \rightarrow F' = 3$ transition (an extended cavity VVV laser seeding a Toptica BoosTA laser amplification system based on a tapered amplifier laser diode), and an additional VVV extended cavity diode laser that can be used for MOT imaging or probing of atoms inside the fiber. The infrastructure on the board includes optical isolators, accusto-optic modulators, fiber couplers, and optics for generating beatnotes for the frequency offset locks.

D.3.2 D$_1$ line lasers

These lasers are used for probing of atoms inside the hollow core fibers. The reference laser is a VVV extended cavity diode laser stabilized by DAVLL to a particular frequency on the D_1 line. The second laser is a Toptica DL100 extended cavity diode laser that is phase-locked to the reference with a phase stabilized version of a frequency offset lock.

D.3.3 Dipole trap lasers

The laser systems we use for far off-resonant dipole traps are not frequency stabilized with feedback loops as is the case for the D_2 and D_1 line lasers. However, stabilization of temperature and current makes them sufficiently stable for our purposes (to less than $\sim 10^{-2}$ nm).

The fiber guided dipole trap was initially implemented with a free running laser diode (Sharp GH0781JA2C, $P_{max} \approx 100$ mW) mounted in a VVV laser diode mount and stabilized at $\lambda \approx 782$ nm. We eventually moved to a home-built (by Thibault) tapered amplifier setup seeded by a free running laser diode (Sanyo DL-LS2075) stabilized at $\lambda \approx 802$ nm.

The blue detuned hollow beam guide for atoms is based on a tapered amplifier setup obtained by turning a damaged tapered amplifier laser (Tiger by Sacher, origi-

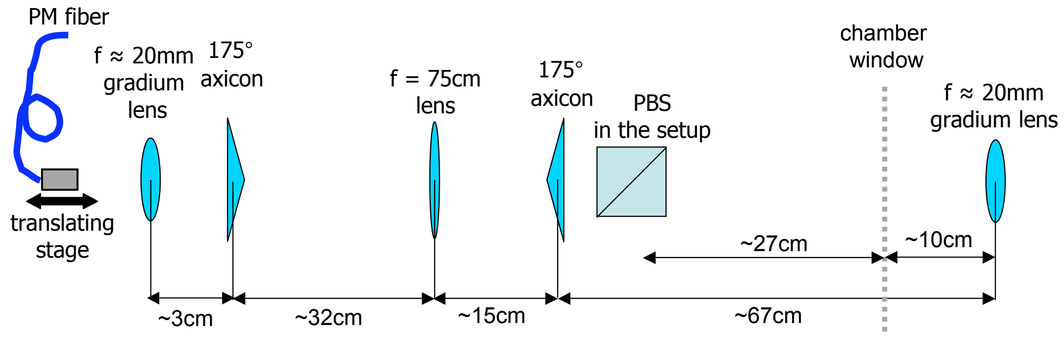

Figure D.3: The optical components and distances between them for the hollow beam setup. Additionally, there are two steering mirrors between the first and the second axicon (to make sure the beam is centered on the second axicon as well), as well as as two steering mirrors between the second axicon and the polarizing beam splitter (PBS), to allow steering of the hollow beam independently of the beams coupled into the fiber. The collimation of the beam coming out of the polarization maintaining (PM) fiber is initially adjusted with the micrometer translation stage such that the beam is focused on the chamber window (viewport) after passing through the two axicons and the 75 cm lens. The collimation of the hollow beam above the fiber tip is finalized by maximizing the loading efficiency of atoms into the PCF.

nally used for the MOT trapping and cooling) into a slave seeded by a free running DFB laser diode stabilized at $\lambda \approx 780.22$ nm.

D.4 Hollow beam generation

A hollow beam is a beam with an intensity minimum (ideally zero) on the propagation axis – basically a ring shaped beam. Higher order Laguerre-Gaussian beams and Bessel beams are examples of hollow beams that are also eigenfunctions of the paraxial form of the Helmholtz equation [80]. Experimentally, hollow beams can be generated by passing a Gaussian beam through a converting set of non-Gaussian optics. The simplest method consists of placing a small opaque disc on the axis of a Gaussian beam. This is of course not very efficient, since a large part of the original beam's power is wasted this way, but for some applications it is sufficient. More sophisticated methods use vortex plates, axicons, and computer generated holograms (either printed on a glass plate or in the form of a spatial light modulator). Issues to consider for a particular application include conversion efficiency, suppression of light on the propagation axis, and area of the dark-spot compared to the area of the bright part of the beam.

The hollow beam generating setup used in our experiment is based on a set of

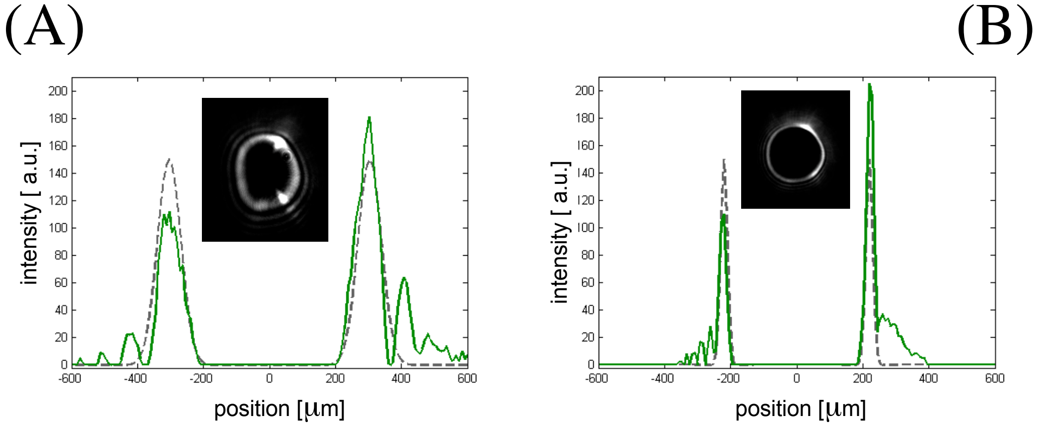

Figure D.4: Intensity profile of the hollow beam at the position of the MOT (A) and ∼1mm above the fiber tip (B), with the insets being the original CCD images. The dashed grey lines correspond to (D.1) where $r_o \approx 300\mu$m and $w_o \approx 70\mu$m for (A) and $r_o \approx 220\mu$m and $w_o \approx 20\mu$m for (B).

axicons [3] and is inspired by the setup used in [84]. This setup is relatively simple, has good conversion efficiency, and its components are relatively inexpensive and available off-the-shelf. The details of the setup can be seen in Fig. D.3. As mentioned in Chapter 4, the distances between the components were finalized by trial and error. The design process was inherently complicated by the the fact that the vertex of a real axicon is rounded and not point-like, and that the hollow beam generated this way is not even remotely an eigenfunction of the Helmholtz equation. A good treatment of the rounded vertex is however provided in [28]. To calculate the trap depth of the hollow beam we approximate the inner ring of the beam profiles from Fig. D.4 by

$$I(r) = I_o \cdot exp\left[-2\left(\frac{r - r_o}{w_o}\right)^2\right]. \tag{D.1}$$

Here $I_o \approx \frac{P_{main\,ring}}{\sqrt{2}\pi^{3/2} r_o\, w_o}$ with $P_{main\,ring}$ being the power in the main (inner) ring. For the beam from Fig.D.4 with $P_{total} = 60$ mW, $P_{main\,ring} \approx \frac{1}{2}P_{total}$, $\lambda = 780.22$ nm ($\Delta \approx 10$ GHz), the trap depth will be $\sim 180\ \mu$K at the MOT site and $\sim 800\ \mu$K ~ 1 mm above the fiber tip where the funnel wires will start obstructing the hollow beam.

---

[3] An axicon is essentially a conical lens, i.e. a lens whose thickness decreases linearly with distance from center, instead of quadratically as is the case for an ordinary lens.

D.5 Probe light detection

The weak probe used in the experiments is detected by a single photon counting module (SPCM-AQR-13-FC by Perkin Elmer). When hit by a photon, the module produces a short TTL pulse with a 65% detection efficiency. This is followed by a so called dead-time (∼50 ns), during which the photon counter cannot detect. Consequently, at higher rates of photon arrival the number of clicks starts to deviate from the linear dependence on photon number and a correction factor described in the photon counter spec sheet has to be included (this becomes a noticeable issue at $\sim 10^6$ clicks/sec). Additionally, the photon counter shuts down if the number of arriving photons exceeds $\sim 10^7$ /sec. The output of the photon counter is collected either by a LabView board or by a fast counting board manufactured by SensL that allows us to time resolve the photons' arrivals.

One of the major challenges in probing the atoms inside the hollow core fiber consists of separating the weak probe (∼1 pW) from the fiber guided dipole trap (∼10 mW) and EIT control field (∼1 nW).

To filter out the dipole trap we use optical bandpass filters. We have had good experiences with filters by Semrock (3 nm wide, off-the-shelf) and by Omega Optical (1 nm wide, custom), as filters from both of those manufacturers have better than 90% transmission for the probe light. These filters can be frequency tuned by slight tilting (but only downwards in wavelength). The filtering can be improved by using two filters in series, however using three will not lead to a significant additional improvement. Furthermore, to make sure that only the light from the hollow fiber core is detected by the photon counter, the probe is additionally spatially filtered by a single mode fiber after passing through the bandpass filters. Lastly, we apply a modulation on the photon counter's control port so that the photon counter only detects when we expect a probe photon arrival. This signal, as well as all the other fast modulations in the experiment, is provided by a PulseBlaster programmable computer board, which ensures synchronization of the modulating signals.

Filtering away the EIT control field is accomplished by a temperature stabilized etalon with a finesse of ~ 50. For a lin$\perp$lin scheme, one etalon in combination with polarization filtering was usually sufficient, while for lin$||$lin two etalons were needed.

Incidentally, diode lasers emit a band of spontaneous light about 20 nm wide. This light is fairly weak (suppressed by ~ 40 dB compared to the stimulated emission), it is however enough to be seen by the photon counters since part of it has the correct frequency to get through the bandpass filters in our case. To avoid this, we place two bandpass filters centered at the dipole trap wavelength in the path of the dipole trap light on the laser breadboard, which clips away the unwanted light.

D.6 Fiber assembly

Figures D.5 and D.6 show the building process of the fiber assembly from figure 4.4A. Note that the structure supporting parts (white) of the assembly were machined out of macor. The fiber assembly is anchored by eight set screws that push against the inner surface of the vacuum chamber. The diameter of the assembly structure is a few millimeters less than the inner diameter (4 inches) of the vacuum chamber.

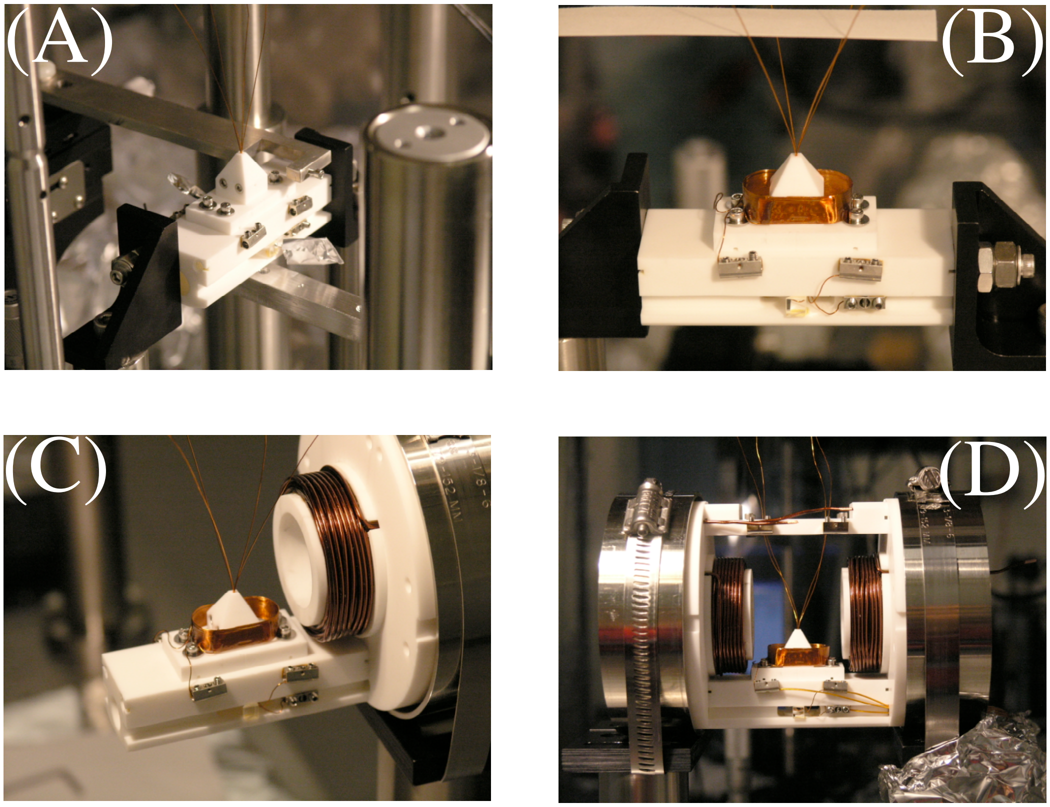

Figure D.5: (A) After the fiber piece is sandwiched between the magnetic funnel wires inside the fiber chuck, the chuck is aligned with the bottom coupling lens (Geltech, aspheric, $f = 4.5$ mm, purchased from Thorlabs), bolted to the bottom bar of the structure, and the bottom ends of the funnel wires are clamped in the eurostripes. (B) The small shift coil is added, together with the main rings carrying the MOT coils (C) and (D).

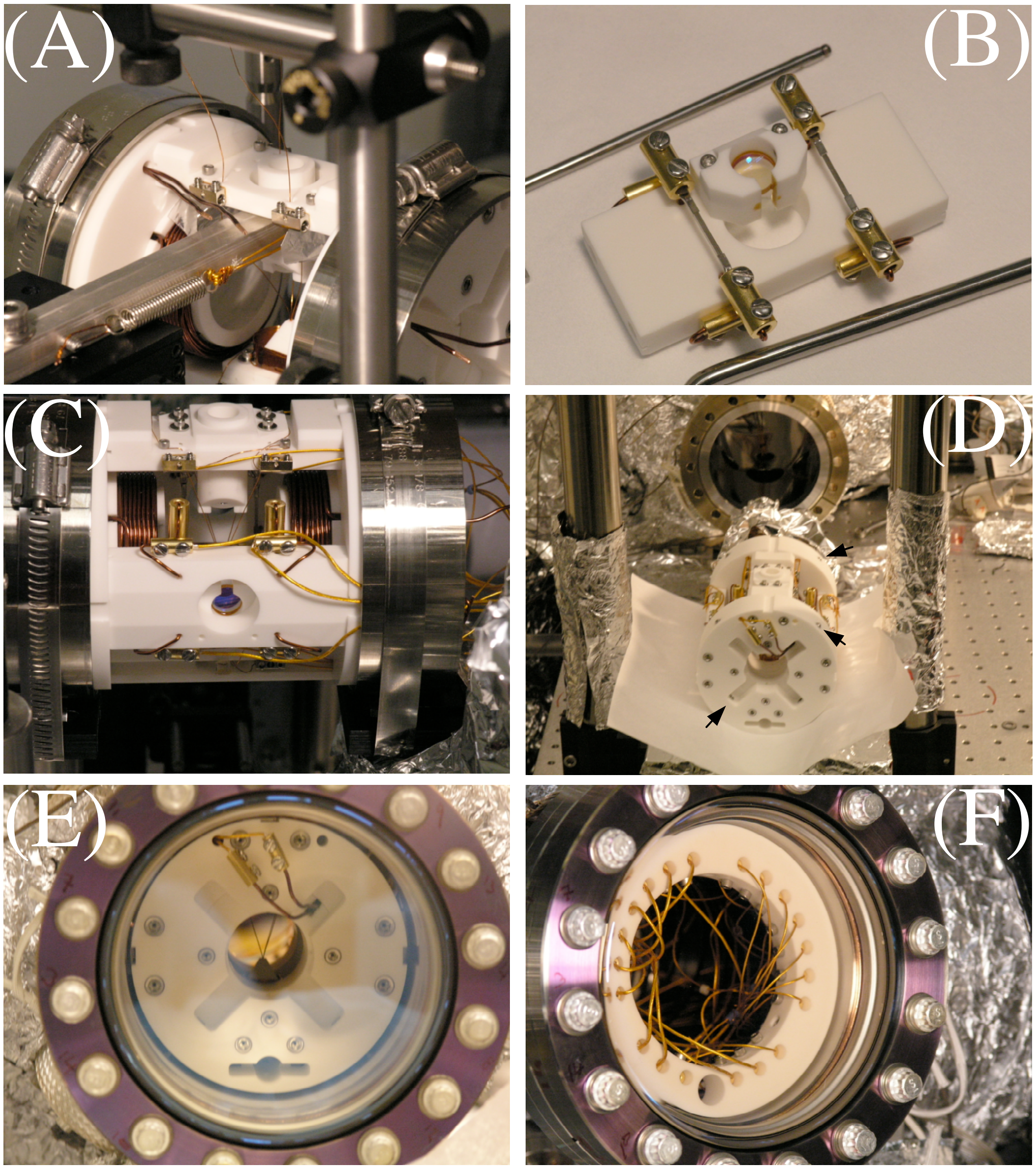

Figure D.6: (A) Alignment of the top coupling lens (gradium lens by LightPath, f = 22 mm at $\sim$ 600 nm, which corrects to f≈20 mm at 800 nm, purchased as NT47-449 from Edmund Optics) (B) One of the structural side bars (for the left side of the assembly) with imaging lens (gradium, Edmund Optics NT47-450) and two of the rubidium dispensers (from SAES Getters USA Inc., 17 mm active length, FT terminals) clamped in barrel connectors. (C) Completed assembly with wiring. (D) Assembly ready to be inserted into the vacuum chamber. The black arrows mark the positions of some of the anchoring set screws. (E) The front side of the vacuum chamber with the assembly loaded in. (F) Back side of the vacuum chamber with the fan-out ring visible. Like the fiber assembly, the fan-out ring is made out of macor and is anchored inside the chamber by set screws.

Appendix E

Atomic cloud expansion in free space

In this section we will describe how the spatial and velocity distribution of a freely expanding cloud of atoms (or molecules) evolves with time. We employ this result in Chapter 4 to estimate the temperature of the initial atomic cloud, the capture radius of the fiber guided dipole trap above the fiber tip, and the temperature of the atoms once they are loaded into the fiber.

We assume that the position and the velocity of an atom in the cloud are two independent random variables with Gaussian distributions at t_o – the start of the expansion. Due to the stochastic nature of cooling in three dimensional optical molasses, this should be a reasonable assumption. We take the end of the cooling process, just when the cooling beams are turned off, as t_o. Thus we assume that at time $t_o = 0$ the number of atoms within a volume element d^3rd^3v of the position-velocity space, with $\vec{v} = (v_x, v_y, v_z)$ and at position $\vec{r} = (r_x, r_y, r_z)$ is

$$N(\vec{r},\vec{v})d^3rd^3v = N_0\frac{1}{\pi^{3/2}}\frac{1}{r_{ox}r_{oy}r_{oz}}e^{-\frac{r_x^2}{r_{ox}^2}}e^{-\frac{r_y^2}{r_{oy}^2}}e^{-\frac{r_z^2}{r_{oz}^2}}\frac{1}{\pi^{3/2}}\frac{1}{v_{ox}v_{oy}v_{oz}}e^{-\frac{v_x^2}{v_{ox}^2}}e^{-\frac{v_y^2}{v_{oy}^2}}e^{-\frac{v_z^2}{v_{oz}^2}}d^3rd^3v \tag{E.1}$$

Here N_0 is the total number of atoms in the cloud, $d^3r = dr_xdr_ydr_z$, $d^3v = dv_xdv_ydv_z$, and with $v_{oi} = \sqrt{\frac{2k_BT_i}{M}}$, $i \in \{x,y,z\}$ and M is the mass of a single atom, we allow for the general case of atoms having a different temperature T_i in each spatial direction. Additionally, at $t_o = 0$ the cloud is centered at the origin and the standard deviations r_{oi}, $i \in \{x,y,z\}$, are referred to as the radius of the cloud in direction i.

We will first derive the time dependent distribution of atoms in space, using a roughly similar treatment as [96]. Following this, we will look at how the probability density function of an atom's velocity, and thus the atom's temperature, becomes dependent on the atom's position in space as the cloud expands.

E.1 Evolution of spatial distribution

Loosely, equation E.1 describes the number of atoms, at time $t_o = 0$, within a volume element $dV = d^3r$ with spatial coordinates (r_x, r_y, r_z) and with velocity (v_x, v_y, v_z) . Consequently, this also describes the number of atoms that at time $t_o = 0$ are within volume element $dV_o = dr_x dr_y dr_z$ with spatial coordinates (r_x, r_y, r_z) and at time t will have moved into volume element $dV_t = dxdydz$ with spatial coordinates (x, y, z) , such that:

$$\begin{aligned} z &= r_z + v_z t \\ y &= r_y + v_y t - \frac{1}{2} g t^2 \\ x &= r_x + v_x t \end{aligned} \tag{E.2}$$

Here we included the effect of gravity and took $\hat{y}$ as the vertical direction. Equation E.1 can be thus rewritten as

$$N(\vec{r}, \vec{v}) d^3r d^3v \rightarrow N(\vec{r}, x, y, z) d^3r dxdydz = \tag{E.3}$$

$$= N_0 \frac{1}{\pi^3} \frac{1}{r_{ox} r_{oy} r_{oz}} e^{-\frac{r_x^2}{r_{ox}^2}} e^{-\frac{r_y^2}{r_{oy}^2}} e^{-\frac{r_y^2}{r_{oy}^2}} \frac{t^{-3}}{v_{ox} v_{oy} v_{oz}} e^{-\frac{(x-r_x)^2}{v_{ox}^2 t^2}} e^{-\frac{(y-r_y+\frac{1}{2}gt^2)^2}{v_{oy}^2 t^2}} e^{-\frac{(z-r_z)^2}{v_{oz}^2 t^2}} d^3r dxdydz$$

using the transformation

$$\begin{aligned} v_z &= \frac{z - r_z}{t} \\ v_y &= \frac{y - r_y + \frac{1}{2} g t^2}{t} \\ v_x &= \frac{x - r_x}{t} \end{aligned} \tag{E.4}$$

with t^{-3} being the determinant of the Jacobian matrix $\mathbf{J}(x, y, z)$ of this transformation:

$$|\mathbf{J}(x, y, z)| = \begin{vmatrix} \frac{\partial v_x}{\partial x} & \frac{\partial v_x}{\partial y} & \frac{\partial v_x}{\partial z} \\ \frac{\partial v_y}{\partial x} & \frac{\partial v_y}{\partial y} & \frac{\partial v_y}{\partial z} \\ \frac{\partial v_z}{\partial x} & \frac{\partial v_z}{\partial y} & \frac{\partial v_z}{\partial z} \end{vmatrix} = \begin{vmatrix} t^{-1} & 0 & 0 \\ 0 & t^{-1} & 0 \\ 0 & 0 & t^{-1} \end{vmatrix} \tag{E.5}$$

The total number of atoms within a particular volume element dV_t can be then obtained by adding up atoms moving into this volume element from all possible volume elements dV_o

$$N(x, y, z, t) dxdydz = \int_{r_x} \int_{r_y} \int_{r_z} N(\vec{r}, x, y, z) dr_x dr_y d_z dxdydz \tag{E.6}$$

Carrying out this integration yields that the number of atoms at time t within a volume element $dxdydz$ with spatial coordinates (x, y, z) is

$$N(x, y, z, t) dxdydz = \frac{N_0}{\pi^{3/2}} \frac{e^{-\frac{x^2}{v_{ox}^2 t^2 + r_{ox}^2}}}{\sqrt{v_{ox}^2 t^2 + r_{ox}^2}} \frac{e^{-\frac{(y+\frac{1}{2}gt^2)^2}{v_{ox}^2 t^2 + r_{ox}^2}}}{\sqrt{v_{oy}^2 t^2 + r_{oy}^2}} \frac{e^{-\frac{z^2}{v_{oz}^2 t^2 + r_{oz}^2}}}{\sqrt{v_{oz}^2 t^2 + r_{oz}^2}} dxdydz \tag{E.7}$$

Consequently, the time dependent radius in direction $i \in \{x, y, z\}$, of a freely expanding atomic cloud is given by

$$r_{[i]}(t) = \sqrt{r_{oi}^2 + v_{oi}^2 t^2} \tag{E.8}$$

where $v_{oi} = \sqrt{\frac{2k_B T_i}{M}}$. This can be used to determine the temperature of an atomic cloud through a time of flight (TOF) measurement in which the cloud's radius is measured as it expands with time.

Additionally, we can obtain the number of atoms within an infinite vertical cylinder with radius R, overlapping with the cloud, by integrating (E.7) over the cylinder volume:

$$N_{atoms} = \int_{y=-\infty}^{+\infty} \int\int_{z^2+x^2=R^2} N(x, y, z, t) dxdydz = N_0 \left(1 - exp\left[\frac{-R^2}{v_o^2 t^2 + r_o^2}\right]\right) \tag{E.9}$$

where for simplicity we assumed $r_{ox} = r_{oz} = r_o$ and $v_{ox} = v_{oz} = v_o$.

E.2 Position dependence of velocity

In this section, we derive the answer to the following question: What is the probability of an atom having velocity $\vec{v} = (v_x, v_y, v_z)$ given that it was found at position (x, y, z) at time t ?[1]

This question describes a conditional probability $P(A|B)$ of event A taking place given that event B already occurred:

$$P(A|B) = \frac{P(A \cap B)}{P(B)} \tag{E.10}$$

where $P(A \cap B)$ is the probability of events A and B occurring simultaneously. In our case, event A is the atom having velocity $\vec{v} = (v_x, v_y, v_z)$ and event B is the atom being found at position (x, y, z) at time t. In the previous section, we derived

$$P(B) = \frac{1}{\pi^{3/2}} \frac{e^{-\frac{x^2}{v_{ox}^2 t^2 + r_{ox}^2}}}{\sqrt{v_{ox}^2 t^2 + r_{ox}^2}} \frac{e^{-\frac{(y+\frac{1}{2}gt^2)^2}{v_{ox}^2 t^2 + r_{ox}^2}}}{\sqrt{v_{oy}^2 t^2 + r_{oy}^2}} \frac{e^{-\frac{z^2}{v_{oz}^2 t^2 + r_{oz}^2}}}{\sqrt{v_{oz}^2 t^2 + r_{oz}^2}} dxdydz \tag{E.11}$$

At the same time, $P(A \cap B)$ is the probability that, at time t, an atom has velocity $\vec{v}(t) = (v_x, v_y, v_z)$ and is found at position (x, y, z). This is equivalent to the

---

[1] Formulated more precisely: What is the probability of an atom being localized within a velocity space volume element $dv_x dv_y dv_z$ positioned at $\vec{v} = (v_x, v_y, v_z)$ given that it was found within volume element $dxdydz$ at position (x, y, z) at time t ?

probability that at time $t_o = 0$ the atom had velocity $\vec{v}(0) = (v_x, v_y + gt, v_z)$ **and** position (r_x, r_y, r_z) such that:

$$\begin{aligned} z &= r_z + v_z t \\ y &= r_y + (v_y + gt)t - \frac{1}{2}gt^2 \\ x &= r_x + v_x t \end{aligned} \tag{E.12}$$

Following equation (E.1), we can then write:

$$P(A \cap B) = \frac{1}{\pi^3}\frac{1}{r_{ox}r_{oy}r_{oz}} e^{-\frac{r_x^2}{r_{ox}^2}} e^{-\frac{r_y^2}{r_{oy}^2}} e^{-\frac{r_z^2}{r_{oz}^2}} \frac{1}{v_{ox}v_{oy}v_{oz}} e^{-\frac{v_x^2}{v_{ox}^2}} e^{-\frac{(v_y+gt)^2}{v_{oy}^2}} e^{-\frac{v_z^2}{v_{oz}^2}} dr_x dr_y dr_z dv_x dv_y dv_z, \tag{E.13}$$

which can be rewritten as

$$\begin{aligned} P(A \cap B) = \quad & \frac{1}{\pi^3}\frac{1}{r_{ox}r_{oy}r_{oz}} e^{-\frac{(x-v_x t)^2}{r_{ox}^2}} e^{-\frac{(y-v_y t-\frac{1}{2}gt^2)^2}{r_{oy}^2}} e^{-\frac{(z-v_z t)^2}{r_{oz}^2}} \\ & \frac{1}{v_{ox}v_{oy}v_{oz}} e^{-\frac{v_x^2}{v_{ox}^2}} e^{-\frac{(v_y+gt)^2}{v_{oy}^2}} e^{-\frac{v_z^2}{v_{oz}^2}} dx dy dz dv_x dv_y dv_z \end{aligned} \tag{E.14}$$

using (E.12). Combining (E.14) and (E.11) in (E.10) we obtain

$$P(A|B) = f_{\vec{v}|\vec{r}}(t) dv_x dv_y dv_z. \tag{E.15}$$

Here $f_{\vec{v}|\vec{r}}$ is the conditional time dependent probability density function for the velocity of an atom, given the atom's position:

$$f_{\vec{v}|\vec{r}}(t) = f_{v_x|x}(v_x, x, t) f_{v_y|y}(v_y, y, t) f_{v_z|z}(v_z, z, t) \tag{E.16}$$

with

$$\begin{aligned} f_{v_x|x}(v_x, x, t) &= \frac{1}{\sqrt{\pi}}\frac{\sqrt{v_{ox}^2 t^2 + r_{ox}^2}}{r_{ox}v_{ox}} exp\left[\frac{-\left(v_x - \frac{txv_{ox}^2}{v_{ox}^2 t^2 + r_{ox}^2}\right)^2}{\frac{r_{ox}^2}{v_{ox}^2 t^2 + r_{ox}^2} v_{ox}^2}\right] \\ f_{v_y|y}(v_y, y, t) &= \frac{1}{\sqrt{\pi}}\frac{\sqrt{v_{oy}^2 t^2 + r_{oy}^2}}{r_{oy}v_{oy}} exp\left[\frac{-\left(v_y - \frac{t\left(y - g\left[\frac{r_{oy}^2}{v_{oy}^2} + \frac{t^2}{2}\right]\right)v_{oy}^2}{v_{oy}^2 t^2 + r_{oy}^2}\right)^2}{\frac{r_{oy}^2}{v_{oy}^2 t^2 + r_{oy}^2} v_{oy}^2}\right] \\ f_{v_z|z}(v_z, z, t) &= \frac{1}{\sqrt{\pi}}\frac{\sqrt{v_{oz}^2 t^2 + r_{oz}^2}}{r_{oz}v_{oz}} exp\left[\frac{-\left(v_z - \frac{tzv_{oz}^2}{v_{oz}^2 t^2 + r_{oz}^2}\right)^2}{\frac{r_{oz}^2}{v_{oz}^2 t^2 + r_{oz}^2} v_{oz}^2}\right] \end{aligned} \tag{E.17}$$

Example plots of these conditional probability density functions can be seen in figures 4.12A and 4.12B for an expanding cloud of ^{87}Rb atoms with $r_{ox} = r_{oy} = r_{oz} = 1mm$ and $v_{ox} = v_{oy} = v_{oz} = 9cm/s$ corresponding to $T \approx 42\mu$K.

Note that atoms found at position (x, y, z) at time t will thus have an average velocity $\vec{v}_{avg} = (\frac{txv_{ox}^2}{v_{ox}^2t^2+r_{ox}^2}, \frac{t\left(y-g\left[\frac{r_{oy}^2}{v_{oy}^2}+\frac{t^2}{2}\right]\right)v_{oy}^2}{v_{oy}^2t^2+r_{oy}^2}, \frac{tzv_{oz}^2}{v_{oz}^2t^2+r_{oz}^2})$. Additionally, the atoms' velocity will have a standard deviation $\vec{\sigma} = (\frac{r_{ox}v_{ox}}{\sqrt{v_{ox}^2t^2+r_{ox}^2}}, \frac{r_{oy}v_{oy}}{\sqrt{v_{oy}^2t^2+r_{oy}^2}}, \frac{r_{oz}v_{oz}}{\sqrt{v_{oz}^2t^2+r_{oz}^2}})$. The magnitude of this standard deviation decreases as $\sim t^{-1}$ for $t \gg \frac{r_{oi}}{v_{oi}}$, which effectively translates into a temperature drop in the middle of the cloud as a result of the cloud's expansion, e.g. $T_x(t) = \frac{Mv_{ox}^2}{2k_B}\frac{r_{ox}^2}{v_{ox}^2t^2+r_{ox}^2}$.

This cooling has an interesting consequence for the phase space density in the center of the cloud. The phase space density is defined as $\rho = N\lambda_{dB}^3$, where N is the number of atoms per unit volume and $\lambda_{dB} = \frac{2\pi\hbar}{\sqrt{3Mk_BT}}$ is the deBroglie wavelength. Combining (E.7) with the spatially dependent temperature derived in this section we find that the phase space density will remain constant with time:

$$\rho(t) = \rho(t_o) = \frac{8\hbar^3 N_0 \pi^{3/2}}{M^3 r_{ox} r_{oy} r_{oz} v_{ox} v_{oy} v_{oz}} \tag{E.18}$$

Bibliography

[1] A. V. Akimov, A. Mukherjee, C. L. Yu, D. E. Chang, A. S. Zibrov, P. R. Hemmer, H. Park, and M. D. Lukin. Generation of single optical plasmons in metallic nanowires coupled to quantum dots. *Nature*, 450:402, 2007.

[2] A. André. *Nonclassical States of Light and Atomic Ensembles: Generation and New Applications*. PhD thesis, Harvard University, May 2005.

[3] A. André, M. Bajcsy, A. S. Zibrov, and M. D. Lukin. Nonlinear optics with stationary pulses of light. *Physical Review Letters*, 94(6):063902, 2005.

[4] A. André and M. D. Lukin. Manipulating light pulses via dynamically controlled photonic band gap. *Phys. Rev. Lett.*, 89:143602, 2002.

[5] E. Arimondo. Coherent population trapping in laser spectroscopy. *Progress in Optics*, 35:257, 1996.

[6] A. Ashkin and J. M. Dziedzic. Optical trapping and manipulation of viruses and bacteria. *Science*, 235:1517, 1987.

[7] M. Bajcsy, S. Hofferberth, V. Balic, T. Peyronel, M. Hafezi, A. S. Zibrov, V. Vuletic, and M. D. Lukin. Efficient all-optical switching using slow light within a hollow fiber. *Phys. Rev. Lett.*, 102:203902, 2009.

[8] M. Bajcsy, A. S. Zibrov, and M. D. Lukin. Stationary pulses of light in an atomic medium. *Nature*, 426:638–641, 2003.

[9] F. Benabid, F. Couny, J. C. Knight, T. A. Birks, and P. S. Russell. Compact, stable and efficient all-fibre gas cells using hollow-core photonic crystal fibres. *Nature*, 434:488, 2005.

[10] F. Benabid, JC. Knight, G. Antonopoulos, and P.S.J. Russell. Stimulated raman scattering in hydrogen-filled hollow-core photonic crystal fiber. *Science*, 298(5592):399–402, OCT 11 2002.

[11] J. Beugnon, C. Tuchendler, H. Marion, A. Gaëtan, Y. Miroshnychenko, Y. R. P. Sortais, A. M. Lance, M. P. A. Jones, G. Messin, A. Browaeys, and P. Grangier. Two-dimensional transport and transfer of a single atomic qubit in optical tweezers. *Nature Physics*, 3:696, 2007.

[12] K. M. Birnbaum, A. Boca, R. Miller, A. D. Boozer, T. E. Northup, and H. J. Kimble. Photon blockade in an optical cavity with one trapped atom. *Nature*, 436:87, 2005.

[13] K. J. Boller, A. Imamoglu, and S. E. Harris. Observation of electromagnetically induced transparency. *Phys. Rev. Lett.*, 66(2593-2596), 1991.

[14] D. Bouwmeester, A. K. Ekert, and A. Zeilinger. *The Physics of Quantum Information*. Springer, New York, 2000.

[15] R.W. Boyd. *Nonlinear Optics*. Academic Press, New York, 1992.

[16] D.A. Braje, V. Balic, G.Y. Yin, and S.E. Harris. Low-light-level nonlinear optics with slow light. *Phys. Rev. A*, 68:041801(R), 2003.

[17] D. R. Brown. Trapping cold rubidium in a fiber. Bachelor's thesis, MIT, 2007.

[18] H. Cao, Y. G. Zhao, S. T. Ho, E. W. Seeling, and R. P. H. Chang. Random laser action in semiconductor powder. *Phys. Rev. Lett.*, 82:2278–2281, 1999.

[19] D.E. Chang, V. Gritsev, G. Morigi, V. Vuletic, M.D. Lukin, and E.A. Demler. Crystallization of strongly interacting photons in a nonlinear optical fiber. *Nature Physics*, 4:884, 2008.

[20] Y.F. Chen, Z.H. Tsai, Y.C. Liu, and I.A. Yu. Low-light-level photon switching by quantum interference. *Opt. Lett.*, 30:3207, 2005.

[21] Caleb A. Christensen, Sebastian Will, Michele Saba, Gyu-Boong Jo, Yong-Il Shin, Wolfgang Ketterle, and David Pritchard. Trapping of ultracold atoms in a hollow-core photonic crystal fiber. *Physical Review A (Atomic, Molecular, and Optical Physics)*, 78(3):033429, 2008.

[22] Y. Chu. Loading rubidium atoms into a hollow core fiber. Bachelor's thesis, MIT, 2007.

[23] C. Cohen-Tannoudji, J. Dupont-Roc, and G. Grynberg. *Photons and Atoms: Introduction to Quantum Electrodynamics*. Wiley-VCH, 1997.

[24] K. L. Corwin, Z. T. Lu, C. F. Hand, R. J. Epstein, and C. E. Wieman. Frequency-stabilized diode laser with the Zeeman shift in an atomic vapor. *Applied Optics*, 37:3295, 1998.

[25] R.F. Cregan, B.J. Mangan, J.C. Knight, T.A. Birks, P.S. Russell, P.J. Roberts, and D.C. Allan. Single-mode photonic band gap guidance of light in air. *Science*, 285(5433):1537 – 1539, 1999.

[26] J. Dalibard and C. Cohen-Tannoudji. Laser cooling below the Doppler limit by polarization gradients: simple theoretical models. *JOSA B*, 6:2023, 1989.

[27] B. Dayan, A. S. Parkins, T. Aok, E.P. Ostby, K.J. Vahala, and H.J. Kimble. A photon turnstile dynamically regulated by one atom. *Science*, 319(5866):1062–1065, 2008.

[28] B. Dépret, P. Verkerk, and D. Hannequin. Characterization and modelling of the hollow beam produced by a real conical lens. *Optics Communications*, 211:31, 2002.

[29] R. M. Dickson and L. A. Lyon. Unidirectional plasmon propagation in metallic nanowires. *J. Phys. Chem. B*, 104:6095, 2000.

[30] M. V. Gurudev Dutt, L. Childress, L. Jiang, E. Togan, J. Maze, F. Jelezko, A. S. Zibrov, P. R. Hemmer, and M. D. Lukin. Quantum register based on individual electronic and nuclear spin qubits in diamond. *Science*, 316:1312, 2007.

[31] M. Fleischhauer. private conversation, 2009.

[32] M. Fleischhauer, A. Imamoğlu, and J.P. Marangos. Electromagnetically induced transparency: Optics in coherent media. *Rev. Mod. Phys.*, 77:633, 2005.

[33] M. Fleischhauer and M. D. Lukin. Dark-state polaritons in electromagnetically induced transparency. *Phys. Rev. Lett.*, 84:5094 – 5097, 2000.

[34] M. Fleischhauer, J. Otterbach, and R. G. Unanyan. Bose-Einstein condensation of stationary-light polaritons. *Phys. Rev. Lett.*, 101:163601, 2008.

[35] I. Fushman, D. Englund, A. Faraon, N. Stoltz, P. Petroff, and J. Vuckovic. Controlled phase shifts with a single quantum dot. *Science*, 320(5877):769–772, 2008.

[36] D. Gammon and D. G. Steel. Optical studies of single quantum dots. *Physics Today*, 55:36, 2002.

[37] C. W. Gardiner, A. S. Parkins, and P. Zoller. Wave-function quantum stochastic differential equations and quantum jump simulation methods. *Phys. Rev. A*, 46:4363, 1992.

[38] S. Ghosh, A. R. Bhagwat, C. K. Renshaw, S. Goh, A. L. Gaeta, and B. J. Kirby. Low-light-level optical interactions with rubidium vapor in a photonic band-gap fiber. *Phys. Rev. Lett.*, 97(2):023603, 2006.

[39] R. Grimm, M. Weidemuller, and Y.B. Ovchinnikov. Optical dipole traps for neutral atoms. *Adv. in Atomic, Molec., and Opt. Phys.*, 42:95–170, 2000.

[40] M. Hafezi. *Strongly interacting systems in AMO physics*. PhD thesis, Harvard University, August 2009.

[41] S. E. Harris. Electromagnetically induced transparency with matched pulses. *Phys. Rev. Lett.*, 70:552–555, 1993.

[42] S.E. Harris. Electromagnetically induced transparency. *Phys. Today*, 50:36 – 42, 1997.

[43] S.E. Harris, J.E. Field, and A. Imamoğlu. Nonlinear optical processes using electromagnetically induced transparency. *Phys. Rev. Lett.*, 64:1107, 1990.

[44] S.E. Harris and L. V. Hau. Nonlinear optics at low light levels. *Phys. Rev. Lett.*, 82:4611 – 4614, 1999.

[45] S.E. Harris and Y. Yamamoto. Photon switching by quantum interference. *Phys. Rev. Lett.*, 81:3611, 1998.

[46] L.V. Hau, S.E. Harris, Z. Dutton, and C.H. Behroozi. Light speed reduction to 17 metres per second in an ultracold atomic gas. *Nature*, 397(6720):594–598, 1999.

[47] P. R. Hemmer. private conversation.

[48] P. R. Hemmer, D. P. Katz, J. Donoghue, M. Cronin-Golomb, M. S. Shahriar, and P. Kumar. Efficient low-intensity optical-phase conjugation based on coherent population trapping in sodium. *Opt. Lett.*, 20:982–984, 1995.

[49] A. Imamoğlu. High efficiency photon counting using stored light. *Phys. Rev. Lett.*, 89(16), OCT 14 2002.

[50] D.F.V. James and P.G. Kwiat. Atomic-vapor-based high efficiency optical detectors with photon number resolution. *Phys. Rev. Lett.*, 89:183601, 2002.

[51] J. D. Joannopoulos, R. D. Meade, and J. N. Winn. *Photonic Crystals: Molding the Flow of Light*. Princeton University Press, 1995.

[52] M. M. Kash, V. A. Sautenkov, A. S. Zibrov, L. Hollberg, G. R. Welch, M. D. Lukin, Y. Rostovtsev, E. S. Fry, and M. O. Scully. Ultraslow group velocity and enhanced nonlinear optical effects in a coherently driven hot atomic gas. *Phys. Rev. Lett.*, 82:5229–5232, 1999.

[53] M. Kiffner and M. J. Hartmann. Dissipation induced Tonks-Girardeau gas of photons. *arXiv*, page 0908.2055, 2009.

[54] O. Kocharovskaya, Y. Rostovtsev, and M. O. Scully. Stopping light via hot atoms. *Phys. Rev. Lett.*, 86:628–631, 2001.

[55] H. Kogelnik and C. V. Shank. Coupled wave theory of distributed feedback lasers. *J.Appl.Phys*, 43:2327, 1972.

[56] S. O. Konorov, A. B. Fedotov, and A. M. Zheltikov. Enhanced four-wave mixing in a hollow-core photonic-crystal fiber. *Opt. Lett.*, 28:1448 – 1450, 2003.

[57] S. J. M. Kuppens, K. L. Corwin, K. W. Miller, T. E. Chupp, and C. E. Wieman. Loading an optical dipole trap. *Phys. Rev. A*, 62:013406, 2000.

[58] Y. Lin, I. Teper, C. Chin, and V. Vuletic. Impact of the Casimir-Polder potential and Johnson noise on Bose-Einstein condensate stability near surfaces. *Phys. Rev. Lett.*, 92:050404, 2004.

[59] Y.-W. Lin, W.-T. Liao, T. Peters, H.-C. Chou, J.-S. Wang, H.-W. Cho, P.-C. Kuan, and I. A. Yu. Stationary light pulses in cold atomic media and without Bragg gratings. *Phys. Rev. Lett.*, 102:213601, 2009.

[60] C. Liu, Z. Dutton, C. H. Behroozi, and L.V. Hau. Observation of coherent optical information storage in an atomic medium using halted light pulses. *Nature*, 409:490 – 493, 2001.

[61] M. D. Lukin, M. Fleischhauer, A. S. Zibrov, H. G. Robinson, V. L. Velichansky, L. Hollberg, and M. O. Scully. Spectroscopy in dense coherent media: Line narrowing and interference effects. *Phys. Rev. Lett.*, 79:2959–2962, 1997.

[62] M.D. Lukin and A. Imamoğlu. Nonlinear optics and quantum entanglement of ultraslow single photons. *Phys. Rev. Lett.*, 84:1419, 2000.

[63] M.D. Lukin and A. Imamoğlu. Controlling photons using electromagnetically induced transparency. *Nature*, 413(6853):273–276, 2001.

[64] H. Mabuchi and A. C. Doherty. Cavity quantum electrodynamics: coherence in context. *Science*, 298:1372, 2002.

[65] H. J. Metcalf and P. van der Straten. *Laser Cooling and Trapping.* Springer, 2001.

[66] R. R. Moseley, S. Shepherd, D. J. Fulton, B. D. Sinclair, and M. H. Dunn. Spatial consequences of electromagnetically induced transparency: Observation of electromagnetically induced focusing. *Phys. Rev. Lett.*, 74:670, 1995.

[67] R. R. Moseley, S. Shepherd, D. J. Fulton, B. D. Sinclair, and M. H. Dunn. Electromagnetically-induced focusing. *Phys. Rev. A*, 53:408, 1996.

[68] D. Muller, E. A. Cornell, D. Z. Anderson, and E. R. I. Abraham. Guiding laser-cooled atoms in hollow-core fibers. *Phys. Rev. A*, 61:033411, 2000.

[69] K. P. Nayak, F. Le Kien, M. Morinaga, and K. Hakuta. Antibunching and bunching of photons in resonance fluorescence from a few atoms into guided modes of an optical nanofiber. *Phys. Rev. A*, 79:021801, 2009.

[70] A. N. Nesmeyanov. *Vapor Pressure of the Chemical Elements.* Elsevier, Amsterdam, 1963.

[71] G. Nikoghosyan and M. Fleischhauer. Stationary light in cold atomic gases. *Phys. Rev. A*, 80:013818, 2009.

[72] M.A. Ol'Shanii, Yu.B. Ovchinnikov, and V.S. Letokhov. Laser guiding of atoms in a hollow optical fiber. *Optics Communications*, 98:77–79, 1993.

[73] C. Ottaviani, D. Vitali, M. Artoni, F. Cataliotti, and P. Tombesi. Polarization qubit phase gate in driven atomic media. *Phys. Rev. Lett.*, 90:197902, 2003.

[74] J. Otterbach, R. G. Unanyan, and M. Fleischhauer. Confining stationary light: Dirac dynamics and Klein tunneling. *Phys. Rev. Lett.*, 102:063602, 2009.

[75] D. Petrosyan and G. Kurizki. Symmetric photon-photon coupling by atoms with Zeeman-split sublevels. *Phys. Rev. A*, 65:033833, 2002.

[76] D. F. Phillips, A. Fleischhauer, A. Mair, R. L. Walsworth, and M. D. Lukin. Storage of light in atomic vapor. *Phys. Rev. Lett.*, 86:783–786, 2001.

[77] Q. M. Quan, I. Bulu, and M. Loncar. Broadband waveguide QED system on a chip. *Phys. Rev. A*, 80:011810, 2009.

[78] E. L. Raab, M. Prentiss, A. Cable, S. Chu, and D. E. Pritchard. Trapping of neutral sodium atoms with radiation pressure. *Phys. Rev. Lett.*, 59:2631, 1987.

[79] G. Sague, E. Vetch, W. Alt, D. Meschede, and A. Rauschenbeutel. Cold-atom physics using ultrathin optical fibers: Light-induced dipole forces and surface interactions. *Phys. Rev. Lett.*, 99:163602, 2007.

[80] B. E. A. Saleh and M. C. Teich. *Fundamentals of Photonics.* Wiley-Interscience, 2 edition, 1997.

[81] H. Schmidt and A. Imamoğlu. Giant Kerr nonlinearities obtained by electromagnetically induced transparency. *Opt. Lett.*, 21:1936, 1996.

[82] M. O. Scully and S. M. Zubairy. *Quantum Optics.* Cambridge University Press, Cambridge, UK, 1997.

[83] D. Slusher and B. Eggelton, editors. *Nonlinear photonic crystals*. Springer, New York, 2003.

[84] Y. Song. *Hollow beam atom tunnel*. PhD thesis, University of Maryland, 1999.

[85] S. M. Spillane, G. S. Pati, K. Salit, M. Hall, P. Kumar, R. G. Beausoleil, and M. S. Shahriar. Observation of nonlinear optical interactions of ultralow levels of light in a tapered optical nanofiber embedded in a hot rubidium vapor. *Phys. Rev. Lett.*, 100:233602, 2008.

[86] D. A. Steck. Rubidium 87 D line data, 2001, `http://steck.us/alkalidata`.

[87] T. Takekoshi and R. J. Knize. Optical guiding of atoms through a hollow-core photonic band-gap fiber. *Phys. Rev. Lett.*, 98(21):210404, 2007.

[88] L. M. Tong, R. R. Gattass, J. B. Ashcom, S. L. He, J. Y. Lou, M. Y. Shen, I. Maxwell, and E. Mazur. Subwavelength-diameter silica wires for low-loss optical wave guiding. *Nature*, 426:816, 2003.

[89] A. V. Turukhin, V. S. Sudarshanam, M. S. Shahriar, J. A. Musser, B. S. Ham, and P. R. Hemmer. Observation of ultraslow and stored light pulses in a solid. *Phys. Rev. Lett.*, 88:023602, 2002.

[90] M. Vengalattore, W. Rooijakkers, R. Conroy, and M. Prentiss. Suppression of photon rescattering due to spatial anisotropy in a cold atomic gas. *Phys. Rev. A*, 67:063412, 2003.

[91] T. Wilk, S. C. Webster, A. Kuhn, and G. Rempe. Single-atom single-photon quantum interface. *Science*, 317:488 – 490, 2007.

[92] Q. F. Xu, V. R. Almeida, R. R. Panepucci, and M. Lipson. Experimental demonstration of guiding and confining light in nanometer-size low-refractive-index material. *Opt. Lett.*, 29:1626, 2004.

[93] E. Yablonovitch, T. J. Gmitter, R. D. Meade, A. M. Rappe, K. D. Brommer, and J. D. Joannopoulos. Donor and acceptor modes in photonic bandgap structures. *Phys. Rev. Lett.*, 67:3380, 1991.

[94] M. Yan, E. Rickey, and Y. Zhu. Observation of absorptive photon switching by quantum interference. *Phys. Rev. A*, 64:041801(R), 2001.

[95] Z.-C. Yan, A. Dalgarno, and J. F. Babb. Long-range interactions of lithium atoms. *Phys. Rev. Lett.*, 55:2882, 1997.

[96] I. Yavin, M. Weel, A. Andreyuk, and A. Kumarakrishnan. A calculation of the time-of-flight distribution of trapped atoms. *Am. J. Phys.*, 70:149, 2001.

[97] D. Yin, H. Schmidt, J. P. Barber, and A. R. Hawkins. Integrated arrow waveguides with hollow cores. *Optics Express*, 12:2710, 2004.

[98] A. S. Zibrov, A. B. Matsko, O. Kocharovskaya, Y. V. Rostovtsev, G. R. Welch, and M. O. Scully. Transporting and time reversing light via atomic coherence. *Phys. Rev. Lett.*, 88:103601, 2002.